SUBTASK 2.1 – PATHWAY TO LOW-CARBON LIGNITE UTILIZATION

Topical Report

(for the period of September 15, 2015, through May 31, 2017)

Prepared for:

AAD Document Control

National Energy Technology Laboratory
U.S. Department of Energy
626 Cochrans Mill Road
PO Box 10940, MS 921-107
Pittsburgh, PA 15236-0940

Cooperative Agreement No.: DE-FE0024233
DOE Technical Monitor: David A. Lang

Prepared by:

John P. Kay
Joshua J. Stanislowski
Scott C. Tolbert
Nathan J. Fiala
Nikhil Patel
Jason D. Laumb

Energy & Environmental Research Center
University of North Dakota
15 North 23rd Street, Stop 9018
Grand Forks, ND 58202-9018

2017-EERC-05-17 May 2017

EERC DISCLAIMER

LEGAL NOTICE This research report was prepared by the Energy & Environmental Research Center (EERC), an agency of the University of North Dakota, as an account of work sponsored by the U.S. Department of Energy National Energy Technology Laboratory. Because of the research nature of the work performed, neither the EERC nor any of its employees makes any warranty, express or implied, or assumes any legal liability or responsibility for the accuracy, completeness, or usefulness of any information, apparatus, product, or process disclosed or represents that its use would not infringe privately owned rights. Reference herein to any specific commercial product, process, or service by trade name, trademark, manufacturer, or otherwise does not necessarily constitute or imply its endorsement or recommendation by the EERC.

DOE DISCLAIMER

This report was prepared as an account of work sponsored by an agency of the United States Government. Neither the United States Government, nor any agency thereof, nor any of their employees, makes any warranty, express or implied, or assumes any legal liability or responsibility for the accuracy, completeness, or usefulness of any information, apparatus, product, or process disclosed, or represents that its use would not infringe privately owned rights. Reference herein to any specific commercial product, process, or service by trade name, trademark, manufacturer, or otherwise does not necessarily constitute or imply its endorsement, recommendation, or favoring by the United States Government or any agency thereof. The views and opinions of authors expressed herein do not necessarily state or reflect those of the United States Government or any agency thereof.

SUBTASK 2.1 – PATHWAY TO LOW-CARBON LIGNITE UTILIZATION

ABSTRACT

Utilities continue to investigate ways to decrease their carbon footprint. Carbon capture and storage (CCS) can enable existing power generation facilities to maintain operations and address carbon reduction. Subtask 2.1 – Pathway to Low-Carbon Lignite Utilization focused on several research areas in an effort to find ways to decrease the cost of capture across both precombustion and postcombustion platforms.

Two postcombustion capture solvents were tested, one from CO_2 Solutions Inc. and one from ARCTECH, Inc. The CO_2 Solutions solvent had been evaluated previously, and the company had incorporated the concept of a rotating packed bed (RPB) to replace the traditional packed columns typically used. In the limited testing performed at the Energy & Environmental Research Center (EERC), no CO_2 reduction benefit was seen from the RPB; however, if the technology could be scaled up, it may introduce some savings in capital expense and overall system footprint. Rudimentary tests were conducted with the ARCTECH solvent to evaluate if it could be utilized in a spray tower configuration contactor and capture CO_2, SO_2, and NO_x. This solvent after loading can be processed to make an additional product to filter wastewater, providing a second-tier usable product.

Modeling of the RPB process for scaling to a 550-MW power system was also conducted. The reduced cost of RPB systems combined with a smaller footprint highlight the potential for reducing the cost of capturing CO_2; however, more extensive testing is needed to truly evaluate their potential for use at full scale.

Hydrogen separation membranes from Commonwealth Scientific and Industrial Research Organisation (CSIRO) were evaluated through precombustion testing. These had also been previously tested and were improved by CSIRO for this test campaign. They are composed of vanadium alloy, which is less expensive than the palladium alloys that are typically used. Their performance was good, and they may be good candidates for medium-pressure gasifiers, but much more scale-up work is needed.

Next-generation power cycles are currently being developed and show promise for high efficiency, and the utilization of supercritical CO_2 to drive a turbine could significantly increase cycle efficiency over traditional steam cycles. The EERC evaluated pressurized oxy-combustion technology from the standpoint of CO_2 purification. If impurities can be removed, the costs for CO_2 capture can be lowered significantly over postcombustion capture systems. Impurity removal consisted of a simple water scrubber referred to as the $DeSNO_x$ process. The process worked well, but corrosion management is crucial to its success. A model of this process was constructed.

Finally, an integrated gasification combined-cycle (IGCC) system model, developed by the Massachusetts Institute of Technology (MIT), was modified to allow for the modeling of membrane systems in the IGCC process. This modified model was used to provide an assessment of the costs of membrane use at full scale. An economic estimation indicated a 14% reduction in cost for CO_2 separation over the SELEXOL™ process.

This subtask was funded through the EERC–DOE Joint Program on Research and Development for Fossil Energy-Related Resources Cooperative Agreement No. DE-FE0024233. Nonfederal sponsors for this project were the North Dakota Industrial Commission, Basin Electric Power Cooperative, and Allete, Inc. (including BNI Coal and Minnesota Power).

TABLE OF CONTENTS

Continued . . .

TABLE OF CONTENTS (continued)

LIST OF FIGURES

Continued . . .

LIST OF FIGURES (continued)

Continued . . .

LIST OF FIGURES (continued)

Continued . . .

LIST OF FIGURES (continued)

LIST OF TABLES

Continued . . .

LIST OF TABLES (continued)

Continued . . .

LIST OF TABLES (continued)

NOMENCLATURE

A/D	analog to digital
Ag	silver
AGAS	acid gas absorption system
AGFC	advanced gasification fuel cell
AHT	advanced hydrogen turbine
APEA	Aspen Process Economic Analyzer
ASME	American Society of Mechanical Engineers
ASU	air separation unit
Au	gold
bby	billion barrels per year
bcc	body-centered cubic
BFW	boiler feed water
BPCV	back-pressure control valve
Btu	British thermal unit
°C	degree Celsius
CCEMC	Climate Change and Emissions Management Corporation
CCS	carbon capture and storage
CEM	continuous emission monitor
CEPS	conversion and environmental process simulator
CF	capacity factor
CFB	circulating fluidized bed
CFBR	continuous fluid-bed reactor
CGE	cold-gas efficiency
CH_4	methane
cm	centimeter
CO	carbon monoxide
CO_2	carbon dioxide
COE	cost of electricity
COS	carbonyl sulfide
CPP	Clean Power Plan
CPU	central processing unit
CSES	CO_2 Solutions Enzymatic Solvent
CSIRO	Commonwealth Scientific and Industrial Research Organization
Cu	copper
DGM	dry gas meter
DOE	U.S. Department of Energy
EERC	Energy & Environmental Research Center
EFG	entrained-flow gasifier
EOR	enhanced oil recovery
EPA	U.S. Environmental Protection Agency

Continued . . .

NOMENCLATURE (continued)

EPRI	Electric Power Research Institute
°F	degree Fahrenheit
FBG	fluidized-bed gasifier
fcc	face-centered cubic
FCV	fuel cell vehicle
FEP	fluorinated ethylene propylene
ft	foot
FT	Fischer–Tropsch
ft^3	cubic foot
FTIR	Fourier transform infrared
GC	gas chromatograph
GEE	General Electric Energy
gph	gallon per hour
gpm	gallon per minute
GSAS	gas-sweetening absorption system
GTS	GasTech Systems
H_2	diatomic hydrogen
H_2S	hydrogen sulfide
HCl	hydrochloric acid
HGFV	hot-gas filter vessel
HHV	higher heating value
HMTS	hydrogen membrane test system
hp	horsepower
hr	hour
HRSG	heat recovery steam generator
HT	high temperature
ICEV	internal combustion engine vehicle
i.d.	inside diameter
IGCC	integrated gasification combined cycle
IGFC	integrated gasification fuel cell
IMTP	Intalox® metal tower packing
in.	inch
ITM	ion transport membrane
K	Kelvin
kg	kilogram
kPa	kilopascal
kW	kilowatt
kW-hr	kilowatt hour
L	liter
lb	pound

Continued . . .

NOMENCLATURE (continued)

L/G	liquid to gas
LGA	laser gas analyzer
lpm	liter per minute
LT	low temperature
m	meter
m^3	cubic meter
MEA	monoethanolamine
mf	mass fraction
mg	milligram
MIT	Massachusetts Institute of Technology
mL	milliliter
mm	millimeter
MMBtu	million British thermal unit
µm	micrometer
mol	mole
MOP	maximum operating pressure
MPa	megapascal
MW	megawatt
MWh	megawatt-hour
NETL	National Energy Technology Laboratory
NGCC	natural gas combined cycle
NH_3	ammonia
nm	nanometer
NO_x	nitrogen oxides
ø	diameter (m)
ø	diameter (ft)
O&M	operating and maintenance
o.d.	outside diameter
Pa	pascal
P&ID	piping and instrumentation drawing
pc	pulverized coal
PCO_2C	Partnership for CO_2 Capture
Pd	palladium
PE	polyethylene
PHEV	plug-in hybrid electric vehicle
ppb	parts per billion
ppm	parts per million
ppmv	parts per million volume
PSA	pressure swing adsorption
psia	pound per square inch, actual

Continued . . .

NOMENCLATURE (continued)

psig	pound per square inch, gauge
PTFE	polytetrafluoroethylene
RPB	rotating packed bed
s	second
scfh	standard cubic foot per hour
scfm	standard cubic foot per minute
scmh	standard cubic meter per hour
scmm	standard cubic meter per minute
SO_2	sulfur dioxide
SOFC	solid oxide fuel cell
SO_x	sulfur oxides
SS	stainless steel
TC	thermal conductivity
TOC	total overnight capital
TPC	total plant cost
TRDU	transport reactor development unit
USC	ultrasupercritical
vol%	volume percent
WGC	water–gas cleanup
WGS	water–gas shift
XRF	x-ray fluorescence

SUBTASK 2.1 – PATHWAY TO LOW-CARBON LIGNITE UTILIZATION

EXECUTIVE SUMMARY

Utilities continue to investigate ways to decrease their carbon footprint. Carbon capture and storage (CCS) can enable existing power generation facilities to maintain operations and address carbon reduction. In the northern Great Plains region, there is synergistic incentive to develop and implement next-generation coal-fired technologies. Regional industry partners are actively seeking options that can cost-effectively improve the efficiency of power production while coproducing CO_2 for use in enhanced oil recovery (EOR) applications. Subtask 2.1 focused on several research areas in an effort to find ways to decrease the cost of capture across both precombustion and postcombustion platforms.

Two postcombustion technologies were investigated: an enzyme-based CO_2 capture solvent used in conjunction with a rotating packed bed (RPB) and a humic acid-based solvent. The CO_2 Solutions enzyme-based solvent had been previously tested at the Energy & Environmental Research Center (EERC) under the Partnership for CO_2 Capture Program, where it displayed moderate success at capturing CO_2. Starting tests on natural gas were conducted using the RPB for the absorption portion of the capture system. However, very limited success was shown, and capture results were not improved over the use of the solvent in a conventional column arrangement. Tests were halted by CO_2 Solutions, and coal-fired tests were not conducted. A short test utilizing the RPB in the regeneration step indicated that the RPB was not suited for this purpose. Assuming the performance was similar to that of previous work on coal, the EERC utilized information on the costs related to RPBs to achieve full-scale performance. The cost of CO_2 recovery (U.S. Department of Energy [DOE] Account Code 5B) was projected to be 50% of the cost as calculated in the DOE bituminous baseline study. This savings resulted in a projected CO_2 capture cost of $30.2/tonne of CO_2 captured (US$ 2007). Although this shows great potential, much more study is needed to determine more accurately how the RPB concept would scale up, and vetting of the associated costs needs to continue.

ARCTECH has developed a CO_2 capture solvent derived from humic acid extracted from North Dakota lignite. ARCTECH had conducted work on a laboratory scale by bubbling cylinder gas mixes through a small tube containing the solvent. It was unclear if the solvent would function in a test apparatus that represents a full-scale system. Tests were conducted in batch mode observing CO_2, SO_2, and NO_x absorption only, no regeneration, firing lignite in an EERC bench combustor. Maximum CO_2 capture was 82%, SO_2 capture was between 80% and 90%, and NO_x capture was between 10% and 20%. The solvent is a good candidate for additional testing, but its regeneration behavior still needs to be examined. Because of the early stages of this technology, economic evaluation was not conducted.

Carbon management will be needed in integrated gasification combined-cycle (IGCC) applications to facilitate the use of hydrogen. Among the most promising technologies are hydrogen separation membranes. Membranes provide the potential to produce hydrogen while simultaneously separating CO_2 at system pressure. Gas impurities must be considered in membrane development as they can very quickly poison the membrane, rendering it unusable. CO_2 can be captured at a lower cost and energy penalty than combustion systems; therefore, methods to remove gas impurities would greatly improve IGCC economics.

The Commonwealth Scientific and Industrial Research Organisation (CSIRO) provided hydrogen separation membranes to test for separation performance. EERC gasification equipment was used to produce the syngas from lignite coal. These were the first tests of the CSIRO membranes on coal-derived syngas. The membranes worked very well, but several improvements are recommended as CSIRO's technology is improved. These include better control of the endothermic reaction of the membrane to reduce fracture potential, additional information on the transmembrane pressure boundaries and upper limits, metallurgy of the membrane connections, and full life cycle testing to determine robustness.

Preliminary economic projections were undertaken on the hydrogen separation process. Scaling costs to an equivalent 550-MW system projected a 14% reduction in cost as compared to the DOE baseline estimate for a SELEXOL™ system. Small future improvements in permeance and performance of the membrane would result in a very significant cost savings for the system.

The EERC also evaluated pressurized oxy-combustion technology from the standpoint of CO_2 purification. Purity of the gas stream is crucial. If the purity can be increased, then it holds great promise in realizing highly efficient systems with simplified CO_2 purification techniques.

Existing EERC gasification equipment was used to generate a syngas to test a technology to remove nitrogen and sulfur species. The system, referred to as the $DeSNO_x$ process, has the potential to be used in not only pressurized oxy-combustion but also supercritical CO_2 cycles. Testing indicated that over 77% nitrogen capture was achieved and greater than 90% of the SO_2 was removed by the process. However, challenges remain with selective condensation of acids at the entry of the $DeSNO_x$ system that must be addressed as the technology is moved forward. Models of both a single-stage and a two-stage oxy-combustion system were created and intended to provide the foundation for future full-scale technoeconomic analysis.

Finally, the EERC modified a model constructed by the Massachusetts Institute of Technology (MIT) which represents an IGCC gasification system with CO_2 capture and compression. The modification substituted H_2 separation membranes for the more traditional SELEXOL process. The modified model performance was compared to the MIT model and the DOE Baseline Case B5B for an IGCC system and indicated an improvement in net power generation of 577 MW_e over 540 MW_e for MIT and 543 MW_e for the DOE case. Efficiency was also improved to 34.7% over 32.4% and 32.6% for the MIT model and the DOE base case, respectively.

This subtask has demonstrated additional promising pathways to improve CO_2 purity in combustion and gasification systems, reduce complexity of plant systems, and project potential economic benefits for the technologies tested. Modeling of many of these technologies was carried out and will provide the foundation for future modeling and pilot-scale testing efforts.

This subtask was funded through the EERC–DOE Joint Program on Research and Development for Fossil Energy-Related Resources Cooperative Agreement No. DE-FE0024233. Nonfederal sponsors for this project were the North Dakota Industrial Commission, Basin Electric Power Cooperative, and Allete, Inc. (including BNI Coal and Minnesota Power).

SUBTASK 2.1 – PATHWAY TO LOW-CARBON LIGNITE UTILIZATION

1.0 INTRODUCTION

Coal will continue to play a major role in meeting energy demands well into the 21st century. Research at the Energy & Environmental Research Center (EERC) is ensuring that coal can be utilized as cleanly and efficiently as possible in existing facilities as well as with emerging technologies. Because CO_2 capture is currently an expensive process that adversely impacts efficiency, considerable effort is being focused on the development of more efficient, cost-effective capture technologies.

In the northern Great Plains region, there is synergistic incentive to develop and implement next-generation coal-fired technologies. Regional industry partners are actively seeking options that can cost-effectively improve the efficiency of power production while coproducing CO_2 for use in enhanced oil recovery (EOR) applications. Commodity markets for CO_2 create the opportunity to offset the capture and first-of-a-kind costs while developing cost-effective technologies that achieve broader applications and meet the future needs for coal-fired power in other regions.

The ultimate goal of the project is to develop knowledge that supports deployment of commercially viable low-carbon power generation technologies for the next generation of coal-fired power plants. Toward that end, the EERC built upon past work performed through its Partnership for CO_2 Capture (PCO_2C) Program, gasification technology development projects, and evaluation of advanced energy cycles and polygeneration systems to advance next-generation coal-fired power systems with integrated CO_2 capture technologies toward commercial application. In this subtask, a series of laboratory, pilot, and modeling screening activities were focused on promising options for advanced power systems and CO_2 capture technologies. Five activities were developed to conduct the work.

Activity 1 – Project Management was focused on project coordination to ensure that results from each of the technical activities (Activities 2–5) were incorporated into and guided project activities. This included quarterly progress reports, the planning and execution of project status meetings, and the generation of this report. Activity 2 – Postcombustion Capture Technologies focused on testing at bench and pilot scale two novel technology concepts. The first concept involved utilizing rotating packed beds (RPBs) for CO_2 capture, and the other was a mineralization solution. A precombustion membrane developed by the Commonwealth Scientific and Industrial Research Organization (CSIRO) was tested in Activity 3 – Precombustion Capture Technologies. Activity 4 – Evaluation of Next-Generation Power Cycles with Carbon Capture looked at generating additional data and information for pressurized oxy-combustion systems and supercritical CO_2 cycles. Finally, Activity 5 – Development of Improved Carbon Capture Systems Engineering Models looked at developing an Aspen Plus® model for integrated gasification combined cycle (IGCC)-based coal-to-electricity conversion utilizing membranes for CO_2 capture. This report describes the work performed in the technical activities, 2–5.

2.0 ACTIVITY 2 – POSTCOMBUSTION CAPTURE TECHNOLOGIES

Under this activity, two technology concepts were tested to collect data on CO_2 capture performance. The first utilized RPBs as a CO_2 absorber and as a solvent regenerator. The second was a solution that could capture CO_2 and sulfur, mineralize the CO_2, and create an additional product for filtering wastewater.

2.1 CO_2 Solutions RPB Concept

Work with CO_2 Solutions, Inc., Quebec, Canada, and its enzyme-based solvent had been conducted previously at the EERC (1) and showed promise as an alternative to monoethanolamine (MEA). This patented process was able to capture almost 50% of the CO_2 from a coal-derived flue gas using only hot water for solvent regeneration. Steam was not needed for the process. Information gained in that work was used by CO_2 Solutions to improve its solvent, and work has continued in Canada with the technology (2).

Since that work, CO_2 Solutions partnered with GasTran Systems (GTS®), Cleveland, Ohio, and developed a RPB technology that offered promising results as an absorption system that could be more economical than traditional packed columns. CO_2 Solutions approached the EERC to perform parametric testing on natural gas and coal to evaluate system performance.

The EERC's solvent-based capture system, shown in Figure 2-1, consists of two absorber columns and one stripper (or regeneration) column, each constructed from 25.4-cm (10-in.)-i.d. stainless steel (SS) column sections of varying lengths bolted together to achieve a desired total height. The absorbers treat the flue gas in series, with the gas flowing from the bottom to the top of each column, countercurrent to the solvent.

The columns contain packing designed to promote liquid–gas contact, facilitating the absorption and regeneration processes. Total combined packing height for the absorber columns is approximately 8 m (25 ft), including 3 m (10 ft) of Koch–Glitsch Intalox® metal tower packing (IMTP) 25 316L SS random packing and 5 m (15 ft) of Sulzer Mellapak™CC advanced structured packing. Liquid distribution plates are inserted at the top of each packing section to evenly distribute the solvent, mitigating wall effects. The top (south) absorber has a 0.3-m (1-ft)-high column section near the middle of the column that is used as a water-cooled heat exchanger to control column temperature. A demister is installed near the top of the absorber column to prevent the flue gas from carrying solvent overhead with the exhaust stream.

The upper (south) absorber column has an integrated intracolumn water-cooled heat exchanger section. The solvent line between the upper and lower absorber columns also has an integrated tube-and-shell heat exchanger that cools the solvent. These heat exchangers help control the exothermic reaction within the absorber column during testing. The columns will handle up to 3.7 scmm (130 scfm) of flue gas generated by one of two nearby combustion systems.

Figure 2-1. EERC solvent-based capture system and control station.

The postcombustion capture system is controlled and monitored through a custom National Instruments™ LabVIEW computer interface developed by the EERC. The LabVIEW control program also records all data generated by the postcombustion capture system, including temperature, pressure, and flow rate.

CO_2 Solutions delivered a RPB system (shown in Figure 2-2) that was integrated into the EERC's system and configured to easily function as an absorber of CO_2 or a solvent regenerator, using the EERC's capture system to perform the remaining functions.

Figure 2-2. Photo of the RPB system provided by CO_2 Solutions.

During initial testing on natural gas using the RPB as the absorber, the rate of CO_2 capture approached 50%, which was similar to that observed with CO_2 Solutions solvent in the EERC's traditional solvent system. When functioning as a solvent regenerator, the unit could not regenerate solvent quickly enough to maintain consistent CO_2 capture and the idea was abandoned. Upon these initial results, the work was halted by CO_2 Solutions and data were not generated on coal-fired flue gas.

Even though data were not collected on coal-fired flue gas, the parallel performance of the RPB system utilizing CO_2 Solutions enzyme-based solvent and that of the EERC's system operating with the solvent in past work allows for an estimation of the economic change that could be realized if a RPB system were utilized at full scale. This work was performed under Activity 5 – Development of Improved Carbon Capture Systems Engineering Models.

2.2 ARCTECH HUMASORB®-L Solution

ARCTECH, Inc., headquartered in Chantilly, Virginia, has a patented coal-derived, organic humic liquid solution that it has successfully shown in small laboratory tests to be effective at removing CO_2 from synthetic flue gas mixtures. This work was the result of a Phase I award under the Climate Change and Emissions Management Corporation (CCEMC) Grand Challenge in 2014 (3). In that work, the solution was held in a small laboratory tube and the synthetic flue gas was allowed to percolate through the solution. ARCTECH lacked the beginning data to show the solution's ability to capture CO_2 in an environment more closely representative of an actual absorber column. After absorption of CO_2, the spent material is used to manufacture a multipurpose filter, HUMASORB-CS, which can be used for the removal of contaminants from wastewater.

The EERC tested HUMASORB-L liquid absorbent for the removal of CO_2, NO_x, and SO_x from coal combustion flue gas. North Dakota lignite was used in the conversion and environmental process simulator (CEPS) test unit at the EERC for this testing.

The CEPS is a downfired design for nominally topfiring 4.0 lb/hr (1.8 kg/hr) of pulverized coal with a heat output of 30,000 Btu/hr. It is a modular system capable of simulating conditions of both the radiant and convective sections of a full-scale utility boiler. The electrically heated 12-ft vertical radiant furnace portion has an inside diameter of 6 in. for the first 9 ft, with the final heated section diameter reduced to 3 in. The radiant zone exit is through a horizontal 1.5-in.-i.d. ceramic tube. From the convective section, flue gas flows through a series of heat exchangers and then on to the particulate control device, which is a baghouse, wet scrubber, or cyclone. Flue gas temperatures are well controlled going into the control device section for typical operation between 250° and 350°F, and flexibility has been built into the system to allow experimentation at even higher flue gas temperatures. Beyond the control device, the flue gas proceeds through an air eductor and up to a stack through the top of the roof of a pilot plant facility at the EERC.

The EERC-fabricated scrubber is designed to remove SO_2 using a conventional chemical engineering approach for the design of a packed gas absorption tower because, for the scale at which this scrubber was designed, random packing best approximates full-scale tray towers. Fabricated from acrylic, it is 4 in. (10.16 cm) in diameter and has a packed height of 6 ft (1.8 m). Koch–Glitsch 25-mm IMTP random packing was used in the column.

HUMASORB-L was contained at the bottom of the absorber column and pumped up to a nozzle at the top of the column. The liquid spray contacted the flue gas in a counterflow arrangement. The absorber column also has a recycle loop for the liquid to keep the HUMASORB-L mixed. The absorber column reservoir is electrically heated to maintain a constant solvent temperature. A variable-speed pump was used to move the solvent from the sump to the nozzle and allowed for adjustment to change the liquid-to-gas (L/G) ratio of the absorber column. The gas flow remained fixed.

The preliminary test plan is given in Table 2-1. Various liquid flow rates were used to move solvent through the column. Gas analyzers recorded the inlet and outlet gas compositions for O_2, CO_2, SO_2, and NO_x. The solvent was sampled, and a few select samples were submitted for analysis to determine the CO_2 content, sulfur content, and a few trace metals. Curves were generated showing the solvent's reaction over time during the given flow rate.

Table 2-1. HUMASORB-L Test Plan

Test	Flue Gas, scfm	HUMASORB-L, gpm	L/G Ratio, gal/1000 ft^3
1	8	0.40	50
2	8	0.60	75
3	8	1.0	125
4	8	1.0	115–125

Inlet flue gas: 10%–15% CO_2, 1200 ppm NO_x, 200 ppm SO_x

Three test runs were performed to evaluate HUMASORB-L liquid absorbent. A solvent sample was collected prior to and at the conclusion of each test. The burning of 4 lb/hr of coal generates approximately 8 scfm (227 lpm) flue gas flow. The flue gas is run through a baghouse to remove particulate before entering the scrubber column.

Gas composition is collected via continuous emissions monitors (CEMs) at the outlet of the combustor and at either the gas outlet or inlet of the scrubber column. Typically, a CEM was positioned to sample at the outlet of the scrubber, but was switchable to sample the inlet as a check on the validity of using the combustor outlet CEM data as the scrubber inlet data. These checks showed very little difference between combustor outlet and scrubber inlet gas analysis, so the data at the combustor outlet were used to determine capture rates.

For the first test, 5 gal (19 liters) of HUMASORB-L solvent was loaded into the system as delivered. With solvent circulating through the column at approximately 0.3 gpm (1.1 lpm), flue gas was introduced to the column. Immediately upon contact with the gas, the solvent began foaming and flooding the column. The system was not able to flow gas through the column, as the foaming solvent created a backpressure on the combustor which was too great for the system to maintain. Follow-up attempts resulted in the same issues. Approximately 40 mL of antifoam was added in two 20 mL stages in an effort to curb the foaming, but it did not have a significant effect. The first test was unsuccessful in operating for any length of time, and no data was generated.

A second test was performed with a new batch of solvent and approximately 40 mL of antifoam was added to the solvent prior to contact with flue gas. Antifoam was mixed into the solvent by pumping the solvent around within the tank, bypassing the column.

At the start of the test, constant flue gas flow of approximately 8 scfm (227 lpm) was introduced to the column and solvent flow started at approximately 0.3 gpm (1.1 lpm), which corresponds to a L/G ratio of approximately 51 gal/1000 ft^3 (193 liters/28.3 m^3). No foaming or effervescing of the solvent was observed upon solvent contacting the flue gas. Solvent ran through the column packing smoothly, with only a few bubbles visible on the surface of the solvent within the tank. Some wall effects were observed during testing, with streams of solvent tracking along the column surface. In areas where the column inner walls were not wetted, flow along and within the packing could be viewed. The percentage of total solvent flow running along the wall was not quantifiable with the apparatus used.

The solvent quickly reached peak performance, with CO_2 capture rate increasing over the first 5 minutes until reaching approximately 73% capture of the incoming CO_2. Figure 2-3 displays CO_2 capture, SO_2 capture, and NO_x capture over the course of the test.

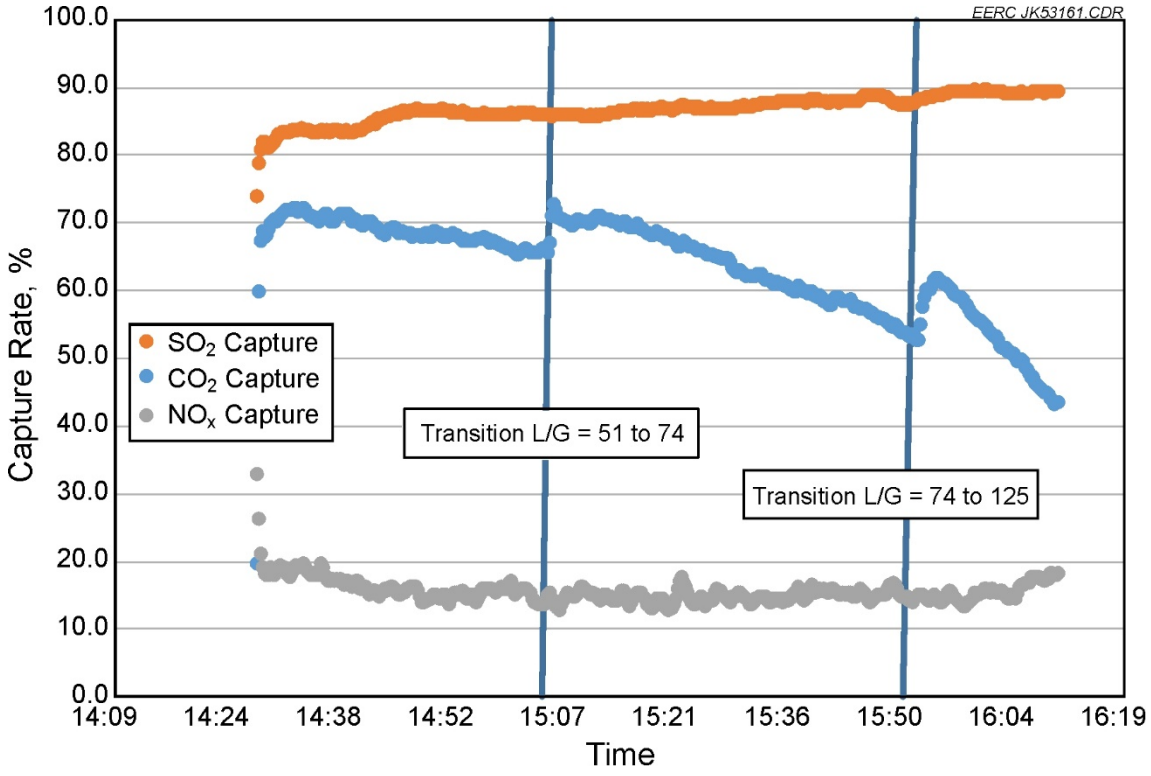

Figure 2-3. Capture profiles for HUMASORB-L at various L/G ratios during the second test.

At each L/G test rate, CO_2 capture decreased as the test progressed. Each transition increased L/G, and CO_2 capture increased for a short time following each transition. SO_2 capture remained between 80% and 90% throughout the test, and between 10% and 20% of NO_x was captured. SO_2 capture appeared to increase throughout the test, with no apparent effect from increasing L/G ratio. Similarly, NO_x capture remained relatively constant throughout the test and did not see a significant change across the L/G ratios tested. A solvent sample was collected at the end of each L/G test period from the column.

A third test was performed, and as with the second test, approximately 40 mL of antifoam was added to the solvent inventory prior to the test. Fuel used was the same coal as the previous tests. For the third test, a single L/G ratio of 115 was maintained. A CO_2 capture decay curve, shown in Figure 2-4, was developed for the solvent.

During the third test, no foaming or effervescing of the solvent was observed within the column packing section, and only a few large dispersed bubbles were observed within the solvent tank. Similar to the second test, wall effects and solvent flow within the packing were observed. SO_2 capture trended steadily upward throughout the test, increasing from about 75% to nearly 85% over 2.5 hr. This mirrored the results from the second test, where SO_2 capture steadily increased to nearly 90%. CO_2 capture increased rapidly upon start-up and continued increasing for approximately 42 minutes to a maximum capture level of 82%. After peaking at 82% capture, CO_2 capture decreased over the next 2 hr to a minimum level of about 10%, at which point the test was ended.

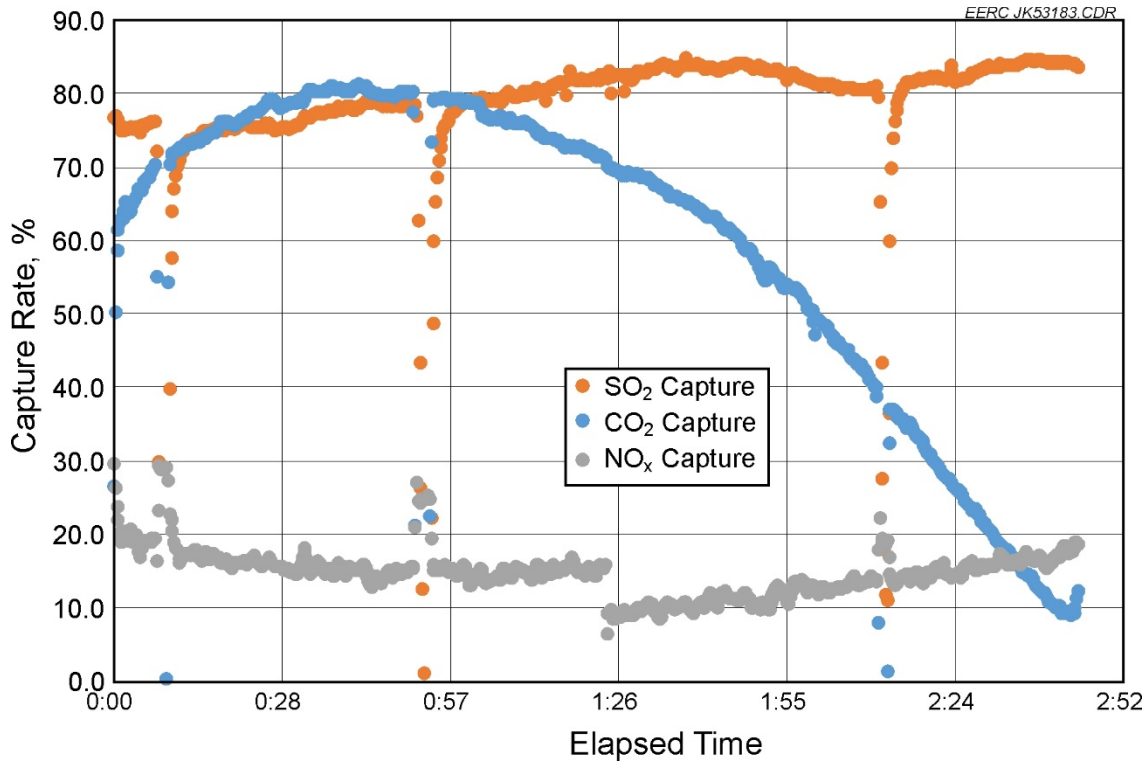

Figure 2-4. Capture profile for HUMASORB-L at constant L/G ratio during the third test.

Table 2-2 gives the results of analyses performed on samples of the coal, untested Humisorb-L solution, solution at the conclusion of Test 2, solution at the point of maximum CO_2 capture during Test 3, and the solution at the conclusion of Test 3. The sample at the point of maximum CO_2 capture was taken at the 36-minute mark of the test, the peak period of CO_2 capture as shown in Figure 2-4. The untested Humisorb-L solution analyzed did include the antifoaming agent.

Table 2-2. Analytical Results of Samples

	S	Cl	Hg	Se	Na	TIC[1]	TOC[2]
Sample	%	µg/g					
Coal	0.33	30.3	0.069		8460	–	70.66
Humisorb, before testing[3]	0.045	25.2	0.0092	<0.5	4600	2680	17900
Test 2 Post	0.034	23.9	0.0088	<0.5	4300	14200	16500
Test 3 – Max CO_2	0.040	19.1	0.01	<0.5	4200	26300	15400
Test 3 Post	0.053	30.3	0.0689	<0.5	4100	38100	13900

[1]TIC – total inorganic carbon.
[2]TOC – total organic carbon.
[3]Sample included antifoam agent.

In summary, HUMASORB-L solvent tests were successful in demonstrating the CO_2, SO_2, and NO_x capture capabilities of the solvent within the test system. With a L/G ratio of 115, a CO_2 saturation curve was produced for a single solvent batch, showing a maximum capture rate of approximately 82% before declining. SO_2 was captured by the solvent at rates between 75% and 90%, and NO_x capture was between 10% and 20%.

The ARCTECH HUMASORB-L showed good potential to be used in a batch situation as a multipollutant capture solvent. The solvent could be utilized in a process that mimics full-scale absorption. More testing at a larger pilot scale would be a benefit in helping develop performance characteristics. Regeneration of the solution was not performed and should also be studied.

3.0 ACTIVITY 3 – PRECOMBUSTION CO_2 CAPTURE TESTING

In order to facilitate the use of hydrogen in IGCC applications or as a transportation fuel, hydrogen-from-coal technologies that are capable of managing carbon will be needed. Many technologies are under development for the separation of hydrogen from coal-derived syngas, and among the most promising are hydrogen separation membranes. Studies indicate a significant IGCC plant efficiency increase can be realized if warm-gas cleanup and hydrogen separation membranes are used in the place of conventional technologies. These membranes provide the potential to produce hydrogen while simultaneously separating carbon dioxide at system pressure. Membrane development activities need to take into account the impact of coal-derived impurities. Gasification syngas typically has many impurities that, if not removed, will poison most hydrogen separation materials. In order to commercialize this promising technology, scale-up to bench- and pilot-scale gasifiers is required so that the impact of impurities can be evaluated.

EERC work focused on testing the CSIRO hydrogen separation membranes for purifying hydrogen from coal-derived syngas. CSIRO provided nine palladium–vanadium metal membranes that were tested on syngas produced in the EERC's fluidized-bed gasifier (FBG). These were the first tests of CSIRO's membranes on actual coal-derived syngas. The EERC's hydrogen membrane test system (HMTS) was used as the platform for testing the membranes. The goal of the project was to conduct tests with coal-to-hydrogen production technology using warm-gas cleanup techniques and CSIRO's hydrogen separation membranes. The FBG and warm-gas cleanup system were configured to facilitate testing in conjunction with the HMTS. The data derived will be used to support CSIRO's efforts in developing hydrogen separation membranes.

3.1 Background

Five main types of membranes are currently under development: dense polymer, microporous ceramic, porous carbon, dense metallic, and dense ceramic (4). Of these types, dense metallic and dense ceramic have the highest hydrogen selectivity. Dense metallic membranes also have very high hydrogen flux rates, making them potential candidates for large-scale commercial application if poisoning issues can be overcome. Palladium is the typical base metal for metallic membranes, and alloy combinations such as Pd–Cu, Pd–Au, and Pd–Ag have been tested. Many other formulations exist, but most are closely guarded trade secrets.

Two main applications for hydrogen separation membranes employed at large scale are envisioned. Large-scale hydrogen production facilities could provide fuel for fuel cell vehicles (FCVs). Power generation facilities with CO_2 capture could employ hydrogen separation membranes to reduce the cost of separation. Both scenarios are likely to employ coal gasification to produce the hydrogen.

3.1.1 Membranes for Hydrogen Production for Transportation Applications

The U.S. Department of Energy (DOE) views hydrogen as an energy carrier of the future because it can be derived from domestic resources that are clean and abundant and because hydrogen is an inherently clean fuel. According to DOE, the deployment of hydrogen technologies could lead to the creation of 675,000 green jobs in the United States (5). Coal gasification plants can separate hydrogen from the synthesis gas, purify the carbon for storage, and burn the hydrogen to produce power in an IGCC configuration. In this type of configuration, the only major emission from the plant is water. Hydrogen can also play a key role as a transportation fuel. If all vehicles in Los Angeles were converted to hydrogen, the urban smog problems would be virtually eliminated. Hydrogen fuel cell technologies have undergone rapid development over the past decade, and the technology exists today to produce commercial hydrogen FCVs that have a transportation range of up to 280 miles (6). The main challenges that remain today are the economical production of hydrogen; the economical production of FCVs; and the development of hydrogen transportation, storage, and dispensing infrastructure.

The National Hydrogen Association views hydrogen as the best pathway to both reduce oil consumption in the United States and reduce transportation-based CO_2 emissions. Figure 3-1 compares three different vehicle market penetration scenarios for light-duty vehicles (7). The bar on the left represents 100% gasoline internal combustion engines, the middle bar represents market penetration for PHEVs, and the bar on the right represents hydrogen FCVs. Each scenario is compared to the annual oil consumption for that time period. It can be seen that if nothing changes and the United States continues to rely solely on gasoline-powered vehicles, the annual oil consumption is predicted to increase from 4 billion barrels per year (bby) to over 7 bby by the year 2100. With a significant market penetration of PHEVs, oil consumption can be reduced to about 2.5 bby by 2100. However, with 98% market penetration of FCVs, dependence on oil is virtually eliminated. While the future of transportation will certainly be a mix of several technologies, this graph illustrates that hydrogen is one of the only pathways toward eliminating the use of oil.

Figure 3-2 shows a similar set of scenarios, but compares the market penetration with annual CO_2 emissions from vehicles (7). It should be noted that the study assumes hydrogen production is occurring with carbon capture and storage (CCS) or hydrogen is supplied from a renewable source. The graph shows that CO_2 emissions from vehicles will almost double by the year 2100 if gasoline vehicles continue to be used exclusively. A reduction in CO_2 emissions is achieved if the course of PHEVs is followed. However, with the FCV scenario, CO_2 emissions are reduced by over 80% in the year 2100. This illustrates that hydrogen is a potential fuel pathway in a carbon-constrained world. Increased production of natural gas and coal will be needed to meet these targets, and the data assume that the hydrogen production facility is equipped with carbon capture technology.

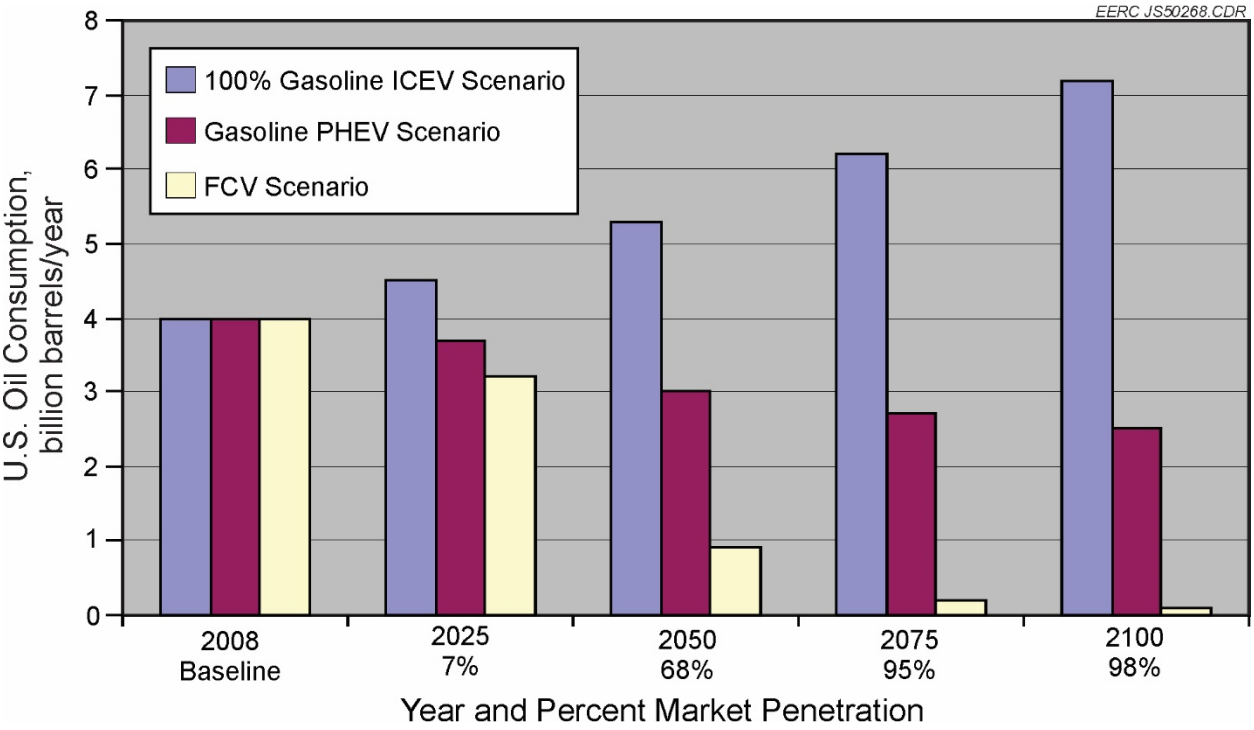

Figure 3-1. U.S. oil consumption for various vehicle scenarios (7) (ICEV is internal combustion engine vehicle, and PHEV is plug-in hybrid electric vehicle).

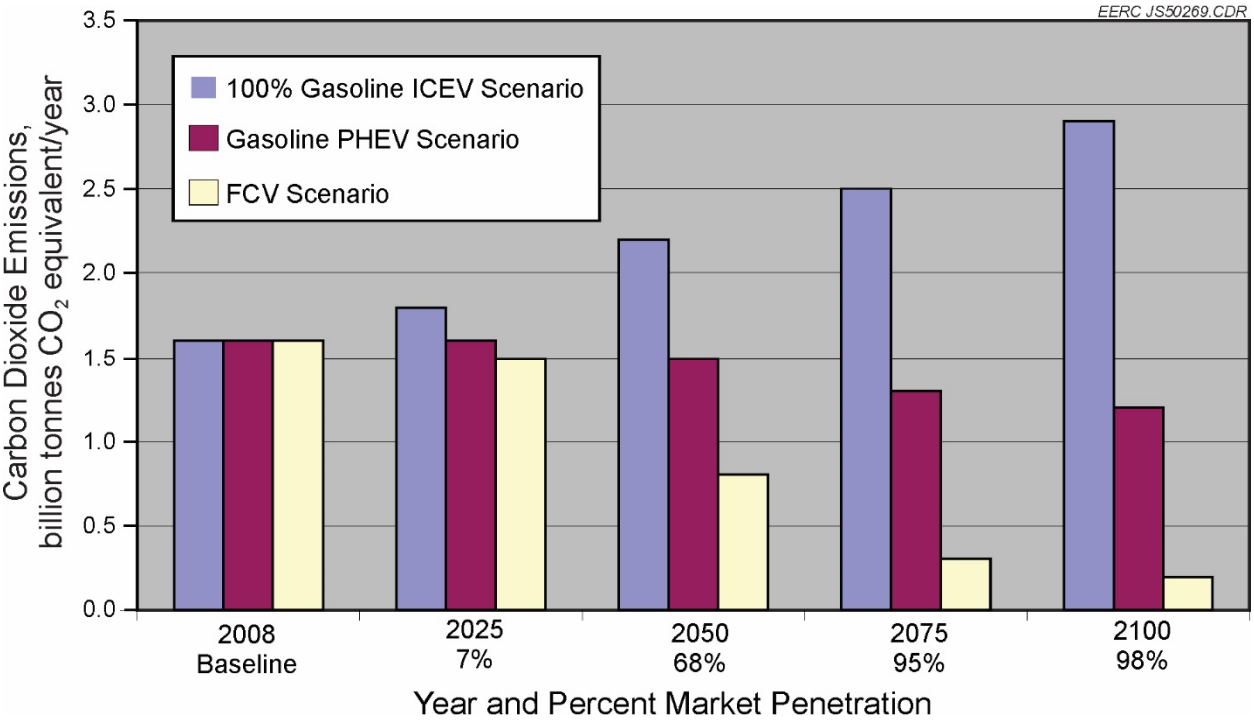

Figure 3-2. CO_2 emissions for various vehicle scenarios (7).

3.1.2 Membranes Integrated with Power Systems

Coal gasification is of significant interest to the future of power generation in the United States because it can be performed more efficiently and with fewer emissions than conventional combustion. IGCC systems fire the syngas produced directly in a gas turbine and recover the heat produced, resulting in more efficient conversion of energy to electricity than a conventional steam cycle. Currently, gasification systems produce electricity at a higher cost than conventional combustion systems. One significant advantage of gasification over combustion is the ability to capture CO_2 at a much lower cost and energy penalty. The CO_2 in gasifier syngas streams is at much higher concentration and typically at elevated pressure; therefore, less energy is required to perform the separation. When the cost of CO_2 capture is considered in the overall capital and operating cost of a power system, gasification units can have advantages in the cost of electricity (COE) over conventional combustion. Figure 3-3 compares the COE for gasification versus conventional power systems with and without CO_2 capture (8). The figure shows that for conventional power systems, the COE is significantly less if CO_2 capture is not required. In the cases where CO_2 capture is needed, the IGCC plant produces electricity at a lower cost than the pc systems. The cost of NGCC is heavily dependent on the price of natural gas. With recent natural gas prices as low as $2/MMBtu, the current cost of NGCC is significantly lower than the competing technologies.

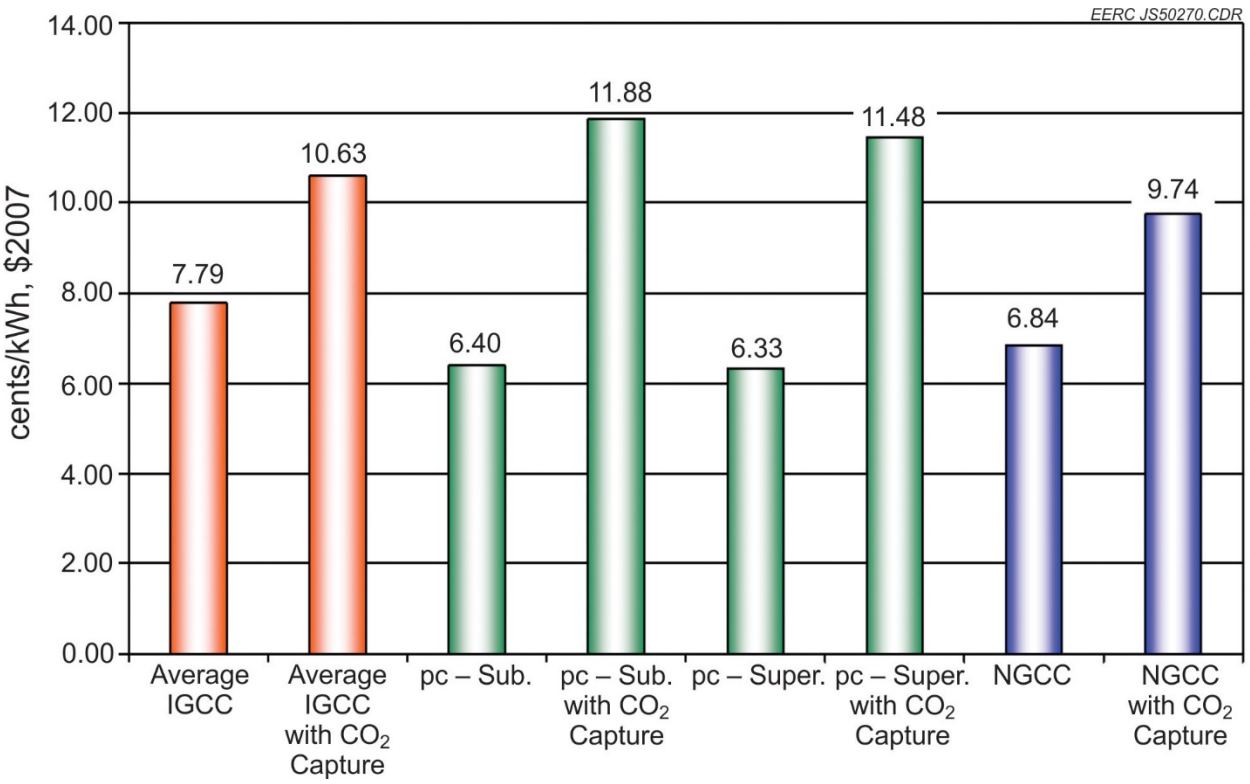

Figure 3-3. Comparison of COE for gasification vs. conventional systems with and without CO_2 capture (8) (pc is pulverized coal, and NGCC is natural gas combined cycle).

The cost of gasification with CO_2 capture utilizing technologies that are commercially available today is still relatively high compared to the COE production with no capture. Advanced technologies are needed to further reduce the costs of capture and improve the overall efficiency of the plants. Several critical research pathways and technologies have been identified by the DOE National Energy Technology Laboratory (NETL) that will greatly improve the efficiency of gasification-based power systems. Figure 3-4 depicts the technology advancements and the incremental increase in net plant efficiency if each technology is implemented (9). The figure indicates that the technology with the highest potential for reducing the cost of gasification systems is hydrogen and CO_2 separation using hydrogen-selective membranes. According to NETL, the implementation of membrane technology can result in a nearly 3% efficiency point increase for a gasification system over using a conventional SELEXOL™ process. If all of the advanced pathway technologies are realized, the efficiency of an IGCC system with hydrogen separation membrane technology and CO_2 capture and compression could reach 40%. Advanced gasification fuel cell (AGFC) technologies could push the efficiency over 50%.

EERC JS50271.CDR

Case Title	Efficiency (% HHV)	Delta* Efficiency (% points)	TPC** (S/kW)	Delta* TPC** ($/kW)	20-yr Leveraged COE (¢/kW-hr)	Delta* COE (¢/kW-hr)
Reference IGCC	30.4	0	2718	0	11.48	0
Adv. "F" Turbine	31.7	1.3	2472	-246	10.64	-0.84
Coal Feed Pump	32.5	0.8	2465	-7	10.54	-0.10
85% CF	32.5	0.0	2465	0	10.14	-0.40
WGCU/Selexol	33.3	0.8	2425	-40	10.00	-0.14
WGCU/H_2 Membrane	36.2	2.9	2047	-378	8.80	-1.20
AHT-1 Turbine	38.0	1.8	1855	-192	8.14	-0.66
ITM	38.3	0.3	1724	-131	7.74	-0.40
AHT-2 Turbine	40.0	1.7	1683	-41	7.61	-0.13
90% CF	40.0	0.0	1683	0	7.36	-0.25
IGCC Pathway		+9.6% pts (+32%)		-1035 (-38%)		-4.12 (-36%)
Advanced IGFC	56.3	+26% pts +85%	1759	-959 (-35%)	7.45	-4.03 (-35%)

* Delta shown is the incremental change as each new technology is added to previous case configuration.
** TPC is reported in January 2007 dollars and excludes owner's costs.

Figure 3-4. Advanced gasification pathways toward improving efficiency and reducing COE for IGCC systems (9) (HHV is higher heating value, TPC is total plant cost, CF is capacity factor, WGCU is water–gas cleanup, AHT is advanced hydrogen turbine, and ITM is ion transport membrane).

3.1.3 Coal Gasification Fundamentals

Coal gasification is a process in which coal is reacted with steam and oxygen at temperature and pressure to form H_2 and carbon monoxide. Pressures can range from atmospheric pressure to 1200 psi, and temperatures range from about 1200° to over 2900°F. Besides the typically desired products H_2 and CO, many other by-products are formed during gasification such as CO_2, CH_4, H_2S, COS, HCl, NH_3, higher hydrocarbons, tars and oils, and particulate matter. The biggest challenge with any gasification system is dealing with the inorganic components in the coal and matching gasifier design to fuel-specific properties and desired end products. Gasifiers are typically configured as fixed beds, fluidized beds, moving beds, or entrained flow. Each gasifier type has strengths and weaknesses depending on the fuel used and the desired end products.

Entrained-flow gasifiers (EFGs) operate at very high temperatures and pressures, usually exceeding 2700°F and 600 psig. Systems are either up-fired or down-fired, and the gasifier operates like a plug flow reactor, with the pulverized solids entrained in the gas stream. Residence times are on the order of seconds. The main advantage of EFGs is that the high temperature results in the destruction of heavy organic materials, light aromatics, and hydrocarbons including methane. Carbon conversions of low-reactivity high-rank coals and petroleum coke can exceed 99%, and most EFGs are designed for high-rank fuels. The inorganic components are melted in the high-temperature environment and flow out of the gasifier as liquid slag. The elevated temperature results in lower cold-gas efficiencies (CGEs) with EFGs, and most gasifiers average near 80% CGE. EFGs are commercially available today and are backed by large companies such as Shell, GE, Siemens, and CB&I.

FBGs operate with a fluidized bed of unconverted carbon and inorganic particles, typically sized to approximately 0.075 in. Solids residence times are typically 0.5 to 2 minutes. The temperature of the system is kept below the ash-melting point, usually below 1600°F, and the systems typically operate at elevated pressure. These systems are well-suited for high-reactivity, low-rank fuels. Fluid beds can produce high levels of tars and organic materials and can achieve CGEs of 90% and carbon conversions over 95%. Commercial systems include the High-Temperature Winkler offered by ThyssenKrupp and the U-Gas technology developed by the Gas Technology Institute and licensed to Synthesis Energy Systems.

Fixed-bed gasifiers operate with a bed of larger coal particles, ranging from 0.5 to 2 in. in size. Both slagging and nonslagging fixed beds have been developed. Depending on the operating conditions, fixed beds can produce high levels of tars, organics, and methane. The low temperature and relatively simple operation of nonslagging systems can lead to high CGEs and low-cost operation. The Lurgi gasifier offered by Air Liquide is currently deployed commercially at Sasol in South Africa and the Great Plains Synfuels Plant in North Dakota.

For the purposes of this test program, syngas was produced from a small pilot-scale EFG and FBG. These systems were chosen because they are commercially available and tend to produce less methane than fixed-bed gasifiers. While methane is not expected to harm membrane materials, elevated levels in syngas reduce the overall capture efficiency of an IGCC facility.

Coal gasification has taken on a renewed interest in recent years because of the rising price of oil and pending carbon legislation. Falling natural gas and oil prices over the last 2 years have made recent deployment and financing of gasification technologies more difficult. Historically, studies have shown that if CCS are required, IGCC plants will have a significant cost advantage over conventional pc boilers with retrofit carbon capture (10, 11). However, the most recent studies have stated that the costs may be similar between the two technologies, especially when considering ultrasupercritical boilers (12–14). At this point, it is difficult to accurately estimate the cost of carbon capture from a pc power plant because no commercially available technology exists. Therefore, these studies must be reevaluated once technologies are commercially available.

3.1.4 Gas Cleanup Fundamentals

Conventionally, cold-gas cleanup methods have been employed to remove contaminants from coal gasification syngas streams. Methods such as Rectisol® or SELEXOL are commercially available and do a very good job removing contaminants but are also very costly from a capital and operational perspective. Significant economic benefits can be realized by utilizing warm- or hot-gas-cleaning techniques. DOE has stated thermal efficiency increases of 8% over conventional techniques can be realized by integrating warm-gas cleanup technologies into IGCC plants (10). Hydrogen separation membranes typically operate at warm-gas cleanup temperatures, so they are a good match for IGCC projects looking to employ warm-gas cleanup and carbon capture.

Work has been performed at the EERC in conjunction with DOE to develop methods to remove contaminants from syngas to levels suitable for a hydrogen separation membrane. The warm-gas cleanup train is capable of removing sulfur, particulate, chlorine, and trace metals including mercury at temperatures above 400°F. All of the technologies utilized are considered either commercial or near-commercial in development. One such test involved gasification of Texas lignite in the EERC's transport reactor development unit (TRDU), with a slipstream of gas being sent to the warm-gas cleanup train (15). Figure 3-5 shows the test setup and a sampling of the results from the test.

Sulfur in the form of hydrogen sulfide and carbonyl sulfide was removed in a transport-style gas–solid contactor at temperatures between 600° and 1000°F. The system was capable of reducing sulfur to single-digit ppm levels in the syngas. Particulate was removed in a HGFV that provided near-absolute filtration using candle filters. Mercury and trace elements were removed with a proprietary sorbent. A high-temperature WGS catalyst significantly increased the hydrogen concentration in the gas stream while reducing CO. A sulfur-polishing bed removed hydrogen sulfide to concentrations below 0.2 ppm. A chlorine guard bed was used in front of the low-temperature WGS catalyst to prevent poisoning. CO was reduced to 0.1% in a low-temperature shift bed, and hydrogen was maximized. If the system were run under oxygen-fired conditions, the resulting syngas would have had combined H_2 and CO_2 levels greater than 90%. After passing through the cleanup train, the syngas was ready for hydrogen and CO_2 separation in a hydrogen separation membrane.

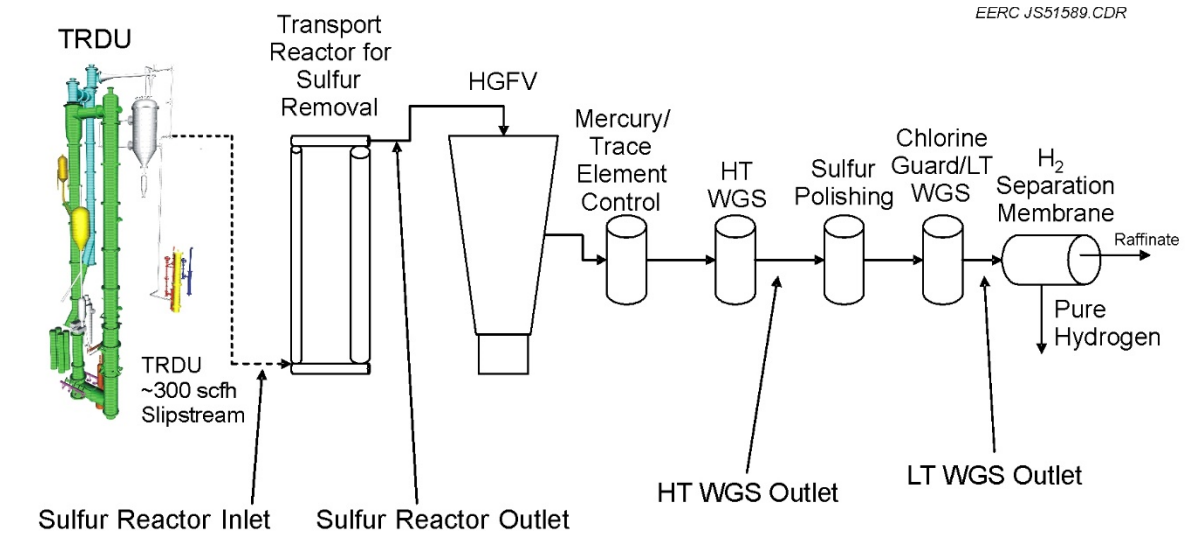

Component	Concentration	Unit
H_2	8.3	%
CO	4.8	%
CO_2	15.0	%
N_2	69.1	%
CH_4	1.7	%
H_2S	3455	ppm
H_2/CO	1.7	ratio

Component	Concentration	Unit
H_2	7.7	%
CO	4.4	%
CO_2	133.8	%
N_2	72.3	%
CH_4	1.5	%
H_2S	4.4	ppm
H_2/CO	1.8	ratio

Component	Concentration	Unit
H_2	10.9	%
CO	1.0	%
CO_2	16.7	%
N_2	68.6	%
CH_4	1.5	%
H_2S	3.0	ppm
H_2/CO	11.0	ratio

Component	Concentration	Unit
H_2	13.3	%
CO	0.1	%
CO_2	18.4	%
N_2	65.5	%
CH_4	1.6	%
H_2S	0	ppm
H_2/CO	98.3	ratio

Figure 3-5. Gasification and gas cleanup process diagram with test results (12) (HGFV is hot-gas filter vessel, HT is high temperature, LT is low temperature, and WGS is water–gas shift).

3.1.5 Conventional Hydrogen Separation Processes

The most commonly employed method used today for hydrogen separation is a process called pressure swing adsorption (PSA). PSA technology is based on an adsorbent bed that captures the impurities in the syngas stream at higher pressure and then releases the impurities at low pressure. Multiple beds are utilized simultaneously so that a continuous stream of hydrogen may be produced. This technology can produce hydrogen with purity greater than 99.9% (16). Temperature swing adsorption is a variation on PSA but is not widely used because of the relatively long time it takes to heat and cool sorbents. Electrical swing adsorption has been proposed as well, but is currently in the development stage. Cryogenic processes also exist to purify hydrogen but require extremely low temperatures and are, therefore, very expensive (17).

3.1.6 Principles of Hydrogen Separation Membranes

Most hydrogen separation membranes operate on the principle that hydrogen selectively penetrates through the membrane because of the inherent properties of the material. The mechanism for hydrogen penetration through the membrane depends on the type of membrane in question. Most membranes rely on the partial pressure of hydrogen in the feed stream as the driving force for permeation, which is balanced with the partial pressure of hydrogen in the permeate stream. Kluiters has categorized membranes into five main types that are commercial or appear to have commercial promise: dense polymer, microporous ceramic, porous carbon, dense metallic,

and dense ceramic (4). Each membrane type has advantages and disadvantages, and research organizations and companies continue to work to develop better versions of each (18). Figure 3-6 illustrates the basic operating principles of hydrogen separation membranes for use in coal-derived syngas (15). This figure shows a dense metallic tubular membrane, but plate-and-frame-style membranes have also been developed. The "syngas in" stream refers to the feed gas into the membrane module. The permeate stream has permeated through the membrane wall and, in this case, is made up of mostly hydrogen. The raffinate stream is what is left of the feed stream once the permeate is separated. A sweep gas such as nitrogen may be used on the permeate side to lower the partial pressure of hydrogen and enable more hydrogen to permeate the membrane.

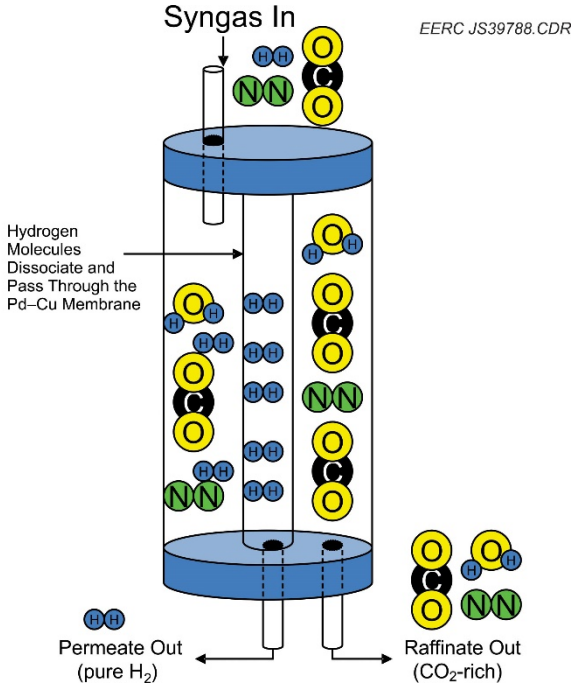

Figure 3-6. Illustration of the operating principle of hydrogen separation membranes (12).

The mechanisms for hydrogen transport through each membrane type are different. However, the performance of each membrane is gauged by two main principles: hydrogen selectivity and hydrogen flux. Hydrogen selectivity is defined by Equation 1 (4):

$$\alpha_{A/B} = \frac{y_A / y_B}{x_A / x_B} \qquad \text{[Eq. 1]}$$

where α is the selectivity factor of component A over component B in the mixture, y_A and y_B are the fractions of those components in the permeate, and x_A and x_B are the fractions of those components in the feed. Components A and B are usually defined so that a higher selectivity factor refers to better membrane performance. A selectivity factor of 1 means there is no component separation.

Hydrogen flux is a measure of the rate of permeation of hydrogen through a membrane wall. The general equation for flux is shown by Equation 2 (4, 17):

$$J_x = \frac{P(p_{x,feed}^n - p_{x,permeate}^n)}{t} \quad \text{[Eq. 2]}$$

where J_x represents the flux of species x, P_x represents the permeability of species x, $p_{x,feed}$ and $p_{x,permeate}$ are the partial pressures of species x in the feed and permeate streams, t is the membrane thickness, and n is the partial pressure exponent. The value of n is usually between 0.5 and 2 and, like the value of P, depends on the transport mechanism assumed. When n = 1, the equation is called Fick's law. For hydrogen transport through a metal membrane, the value of n is usually 0.5, and the equation reduces to what is referred to as Sievert's law. Sievert's law is a useful way of measuring membrane performance because it takes into account the membrane thickness and the partial pressure of hydrogen on each side of the membrane.

Since most membranes operate on a partial pressure differential, there will always be some hydrogen left behind in the raffinate stream. Therefore, an additional measurement of performance is the recovery or yield, as shown by Equation 3 (4):

$$S = \frac{q_p}{q_f} \quad \text{[Eq. 3]}$$

where S is the yield, q_p is the permeate flow, and q_f is the feed flow. There are numerous other ways to quantify the yield, including calculating the volume reduction in the raffinate or the percentage hydrogen recovery from the feed.

The five basic types of membranes mentioned earlier each have inherent advantages and disadvantages, depending on the desired operating conditions and necessary product specifications. With data presented by Kluiters (4) and modified with Adhikari and Fernando (17) and Ockwig and Nenoff (19), Table 3-1 compares, in general, the relative operational performance of these five membrane types. Typical operational temperature will vary by specific membrane type, but it can be seen that the dense polymer membranes are only applicable at low temperature. Dense ceramic and dense metallic membranes have the highest hydrogen selectivity, and hydrogen flux is highest with dense metallic or microporous ceramic membranes. While dense metallic membranes seem to have the best performance relative to hydrogen, they are also very susceptible to poisoning from many compounds found in syngas, and metal alloys can be very expensive. Dense ceramic membranes also have high potential for commercial applications. They are less susceptible to poisoning than metallic membranes and, depending on the material, can be significantly less inexpensive. Development work is under way with each of these membrane types to increase the resistance to poisoning and reduce cost.

Table 3-1. Properties of Five Hydrogen-Selective Membranes (4, 17, 19)

	Dense Polymer	Microporous Ceramic	Dense Ceramic	Porous Carbon	Dense Metallic
Temperature Range	<100°C	200°–600°C	600°–900°C	500°–900°C	300°–600°C
H_2 Selectivity	Low	Moderate	Very high	Low	Very high
H_2 Flux	Low	High	Moderate	Moderate	High
Known Poisoning Issues	HCl, SO_x, CO_2		H_2S	Organics	H_2S, HCl, CO
Example Materials	Polymers	Silica, alumina, zirconia, titania, zeolites	$SrCeO_{3-\delta}$, $BaCeO_{3-\delta}$	Carbon	Palladium Alloys, Pd–Cu, Pd–Au
Transport Mechanism	Solution/ diffusion	Molecular sieving	Solution/ diffusion	Surface diffusion, molecular sieving	Solution/ diffusion

3.1.6.1 Hydrogen Transport Mechanisms

For porous membranes, there are four types of diffusion mechanisms that can effect hydrogen separation: Knudsen diffusion, surface diffusion, capillary condensation, and molecular sieving. Knudsen diffusion occurs when the Knudsen number, Kn defined by Equation 4, is large (19).

$$Kn = \frac{\lambda}{L} \qquad \text{[Eq. 4]}$$

where λ represents the mean free path of the gas molecules, and L is the pore radius. At Knudsen numbers larger than 10, Knudsen diffusion becomes significant. Surface diffusion refers to gas molecules that are absorbed on the pore wall and migrate along the surface to the other side. Surface and Knudsen diffusion can occur simultaneously. Capillary condensation occurs if a partially condensed phase fills the pores and does not let other molecules penetrate. Molecular sieving occurs when the pores are so small that only the smaller molecules can fit through. Selectivity toward hydrogen is greatest with molecular sieving and is least with the Knudsen diffusion mechanism (4, 19)

This work focuses on palladium-based dense metallic membranes, which rely on a solution/diffusion mechanism to transport hydrogen. The solution/diffusion mechanism is somewhat more complex than the porous diffusion mechanisms, although relatively straightforward in nature. Ockwig and Nenoff (19) have presented a seven-step mechanism in which 1) the hydrogen mixture moves to the surface of the membrane, 2) the H_2 molecules dissociate into H^+ ions and electrons, 3) the ions adsorb into the membrane bulk, 4) the H^+ ions diffuse through the membrane, 5) the H^+ ions desorb from the membrane, 6) the H^+ ions and electrons recombine back to H_2 molecules, and 7) the H_2 from the surface of the membrane. In the

case of metal membranes, only hydrogen undergoes the solution/diffusion mechanism; therefore, the membranes are considered 100% selective to hydrogen.

Figure 3-7 illustrates the mechanism of separation in a seven-step process that depicts hydrogen transport through dense metallic membranes as atoms. The mechanism is very similar to that proposed by Ockwig and Nenoff (19) in the case of ion transport membranes. Key points for the mechanism of separation are the catalytic dissociation of hydrogen on the membrane surface and absorption of H atoms into the alloy structure. Both of these key steps can be hindered by the presence of sulfur on the surface of the membrane, reducing the overall flux rate. Sulfur could also be present on the reassociation side of the membrane if a significant leak in the material were ever present during operations. Diffusion of the hydrogen away from the surface is also an important point because under normal operating conditions, the gas is pure hydrogen and, therefore, the partial pressure of hydrogen can be high. In IGCC cases, a sweep gas of nitrogen would be employed to improve the overall efficiency of the separation, temper the combustion flame in the gas turbine, and provide additional mass to drive the turbine.

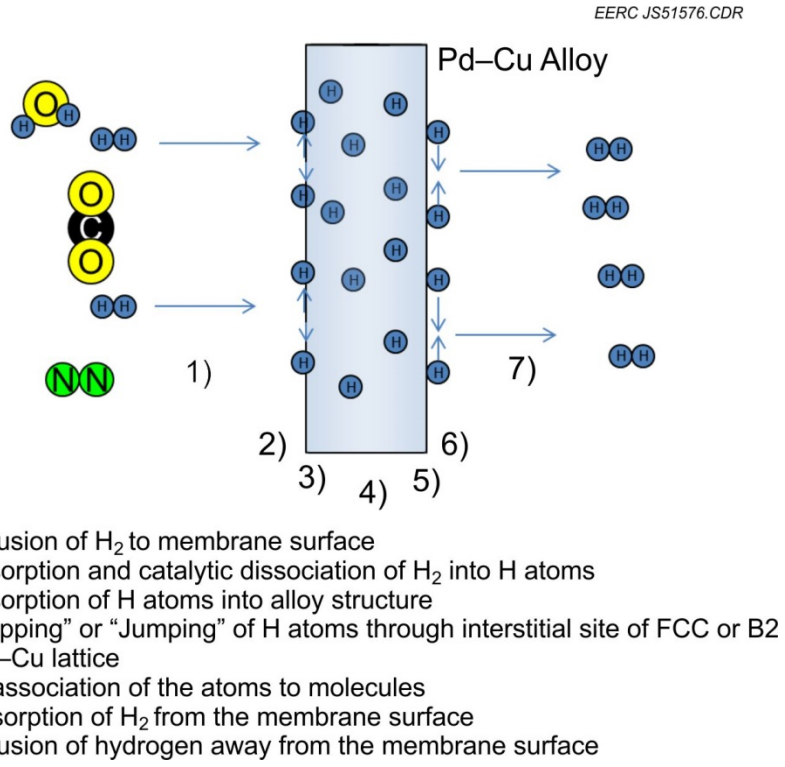

1. Diffusion of H_2 to membrane surface
2. Adsorption and catalytic dissociation of H_2 into H atoms
3. Adsorption of H atoms into alloy structure
4. "Hopping" or "Jumping" of H atoms through interstitial site of FCC or B2 Pd–Cu lattice
5. Reassociation of the atoms to molecules
6. Desorption of H_2 from the membrane surface
7. Diffusion of hydrogen away from the membrane surface

Figure 3-7. Seven-step mechanism of hydrogen separation through dense metallic membranes.

3.1.7 Impact of Sulfur on Membrane Performance

Dense metallic Pd–Cu-based metallic membranes are of great interest to researchers because they hold properties of high selectivity and high flux rates and have shown the potential to resist sulfur poisoning (20). The nature of the Pd–Cu structure is of great importance when it comes to

the permeation of hydrogen through the membrane. Pd–Cu either forms a body-centered cubic structure or a face-centered cubic structure, depicted in Figure 3-8. The bcc structure contains copper atoms at each of the eight corners of the cubic matrix, with a palladium atom at the center of the cube. The fcc structure also contains eight copper atoms at the corners, but also a palladium atom at the center of each face of the cube.

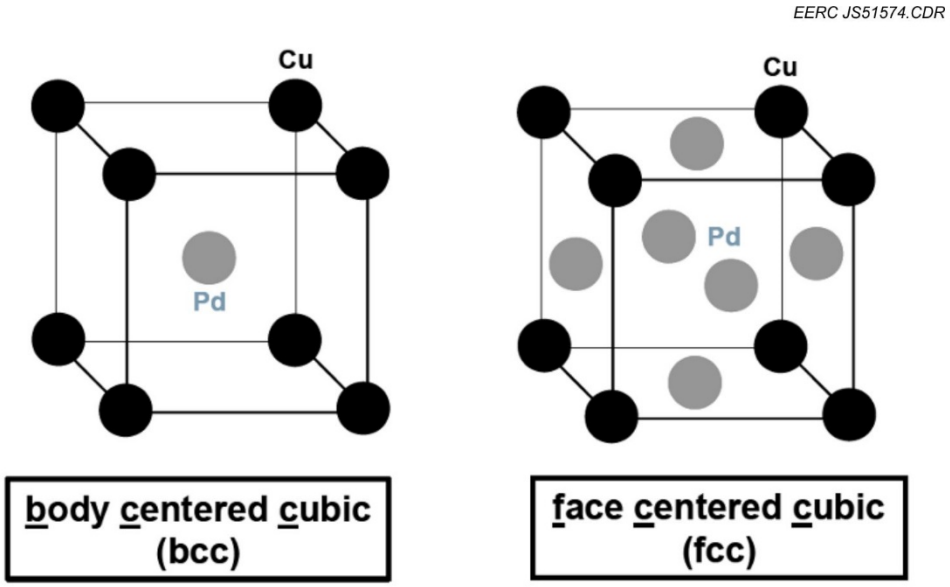

Figure 3-8. Pd–Cu crystalline structure in bcc and fcc orientations (20).

As shown in Figure 3-9, the type of crystalline structure formed depends on both the composition and temperature of the material (20–22). The bcc structure is encountered in the widest temperature range at a concentration of 53 wt% Pd and 47 wt% Cu. It is for this reason that many studies have evaluated this particular composition. Studies also indicate that the bcc structure has higher hydrogen permeability but lower resistance to sulfur than the fcc structure. Rothenberger et al. reported that performance degradations of an order of magnitude were observed when exposing bcc structures to 1000 ppm H_2S, but performance degradations of less than 20% were observed when exposing fcc–crystalline-phase materials to the same conditions (20).

The diffusion of hydrogen through a palladium membrane or a palladium copper alloy has been described in detail by a number of authors (23–25) in an attempt to understand and predict the energies required for hydrogen atoms to diffuse through Pd–Cu lattices. Figure 3-10 depicts possible positions for H atoms to exist in bcc Pd–Cu. Sholl described the movements to and from tetrahedral sites and determined the activation energy required for each of these movements (24). Understanding of the first principles of hydrogen diffusion through metal materials can lead to breakthroughs in development of new materials and crystal arrangements. Kamakoti and Sholl (26) also studied the impact of ternary alloys on hydrogen diffusion and have undertaken a number of studies involving novel metals and amorphous materials for hydrogen separation (27–29).

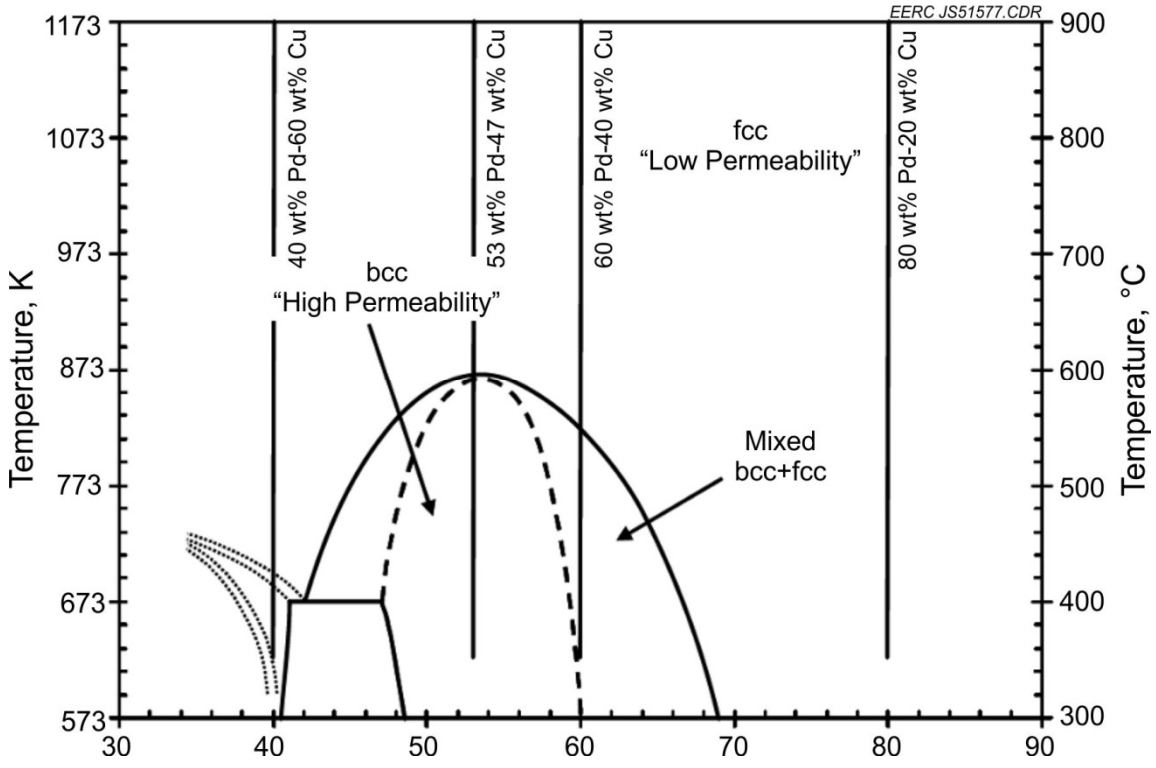

Figure 3-9. Pd–Cu phase diagram (20–22).

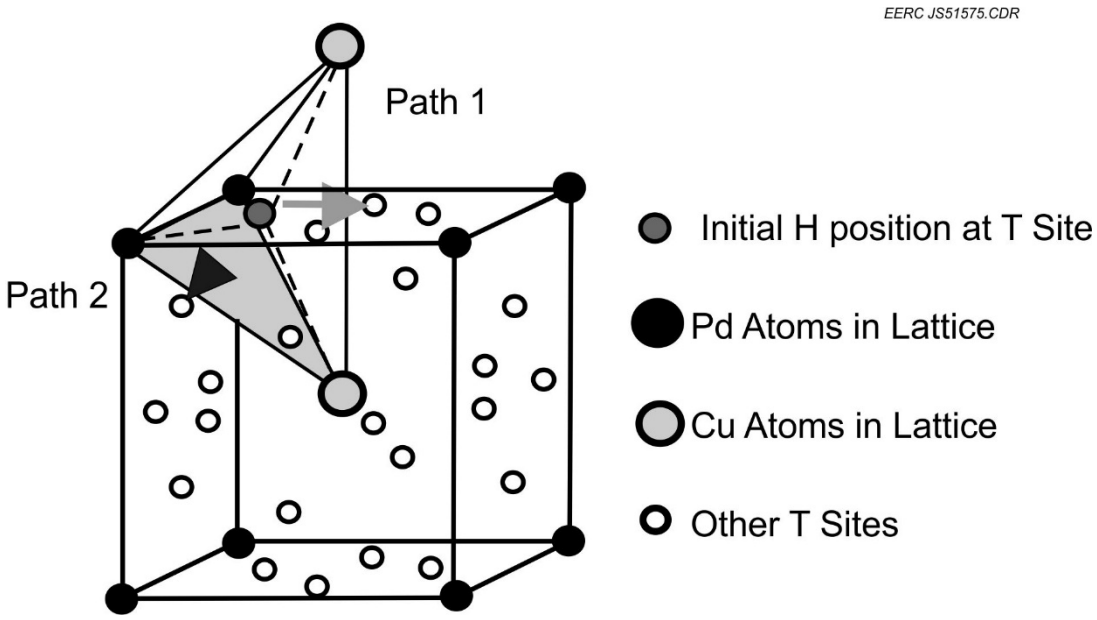

Figure 3-10. Possible pathways for H motion in bcc Pd–Cu (25).

Sulfur poisoning is known to impact the flux rate of hydrogen through Pd and Pd–Cu alloys. O'Brien (30) theorized that hydrogen transport across a membrane is impacted by sulfur poisoning in two manners: 1) by producing a thin sulfide film on the surface of the membrane with low hydrogen permeability and 2) by blocking Pd from catalyzing the hydrogen dissociation reaction and, therefore, slowing the rate of dissociation. O'Brien's permeation experiments and H_2–D_2 experiments showed that both mechanisms indeed impact hydrogen flux rates through Pd–Cu membranes. The study also showed that at elevated temperature (900 K), H_2S has no impact on hydrogen permeation through $Pd_{47}Cu_{53}$ alloys.

Studies by Gabitto and Tsouris (31) concluded that $Pd_{60}Cu_{40}$ alloys represent the best combination of high hydrogen flux and sulfur resistance. Studies have shown that sulfur poisoning of a thin membrane of fcc $Pd_{81}Cu_{19}$ was completely reversible if the sulfur was exposed to the membrane above 450°C (32). If the sulfur was exposed at 400°C, the original membrane performance could not be reestablished. Yang et al. evaluated the performance of a $Pd_{60}Cu_{40}$ membrane covered with a thin coating of nickel to promote resistance to H_2S (33). The results of this study indicated that the H_2S poisoning was reversible and that the membrane shows little performance degradation when operated above 573 K.

3.2 Experimental Methods and Equipment

3.2.1 CSIRO Hydrogen Separation Membrane Tubes

The membrane tubes supplied for this test were a novel design constructed of extruded vanadium alloy. Vanadium is highly permeable to hydrogen and has much lower cost to manufacture compared to palladium alloys. The hydrogen permeability of vanadium is tens of times greater than that of palladium, making vanadium of particular interest for use in hydrogen-selective metal membranes. Self-supporting vanadium-based metal membranes, comprising a vanadium core overlaid with hydrogen dissociation and recombination catalysts, are a low-cost alternative to the current benchmark Pd-based membranes. In this configuration, Pd is applied in submicrometer layers on the inner and outer surface of dense vanadium tubes, thereby minimizing Pd consumption and its high associated cost. The vanadium tube serves the dual purposes of imparting mechanical strength against large transmembrane pressures, and providing a gas-tight medium through which only atomic hydrogen can migrate. This brings the additional benefit of eliminating the requirement for costly porous supports, meaning the economic case for this technology is strong. Ultimately, however, it is the performance in realistic industrial environments which will determine the market potential of this and other metal membrane technologies.

The hydrogen membrane separators tested during this project were formed from vanadium tubing (99.9%), with an outer diameter of 9.5 mm (3/8-in. o.d.), a wall thickness of 0.250 mm, and length of 330 mm, procured from a commercial supplier. The vanadium tubes were treated to remove all traces of grease and oxides. A 500-nm 70%–30% palladium–gold outer layer was applied to the vanadium tube. A 500-nm palladium layer was applied to the inner surface. The tubes were finally annealed under vacuum at 300°C for several hours to remove dissolved H_2 and improve adhesion of the deposited layers. The separator tubes were sealed using commercially available compression fittings and graphite ferrules. Figure 3-11 shows the as-received vanadium

Figure 3-11. Example of as-received tube (bottom), Pd-coated separator (middle), and a separator sealed with compression fittings (top).

tube, the vanadium tube after Pd deposition, and sealed with compression fittings. A 316 SS tube is also shown for comparison at the bottom of Figure 3-11. A total of four membranes were prepared for the campaign. In prior testing, CSIRO provided separators with the same overall dimensions but with thicker tube walls of 0.50 mm and coated with a 500-nm 100% palladium coating on both the inside and outside. Because of the thinner vanadium tube walls of the separators supplied for this testing campaign, pressures were limited to 10 bar (130 psig).

CSIRO reported that in order to determine the baseline membrane performance, one membrane from the batch was subjected to pure gas permeability testing in its lab. The constant pressure method was used, whereby the outer surface of the membrane was exposed to a stream of flowing, pure H_2 at a constant pressure while the inner surface was maintained at 1.0 bar. The steady-state H_2 flux was measured for 10 minutes, after which the feed pressure and temperature conditions were changed.

Figure 3-12 shows the measured H_2 flux (flow per area per time) at several temperatures and pressures reported by CSIRO for the thicker 0.50-mm separators used in prior testing. Flux increases with increasing feed pressure and increasing temperature. Figure 3-13 shows the membrane performance expressed as permeability (mol m^{-1} s^{-1} $Pa^{-0.5}$), as reported by CSIRO. The nonlinearity of the data suggests hydrogen transport is at least partially limited by surface resistances, but the permeability values in excess of 2 to 3 × 10^{-7} mol m^{-1} s^{-1} $Pa^{-0.5}$ are more than 20× that of palladium under the same conditions. No test data were provided by CSIRO for the thinner 0.25-mm separators used during this testing campaign. Because of the limited number of separators furnished for this campaign, it was decided to not sacrifice a separator in order to conduct the test at the EERC.

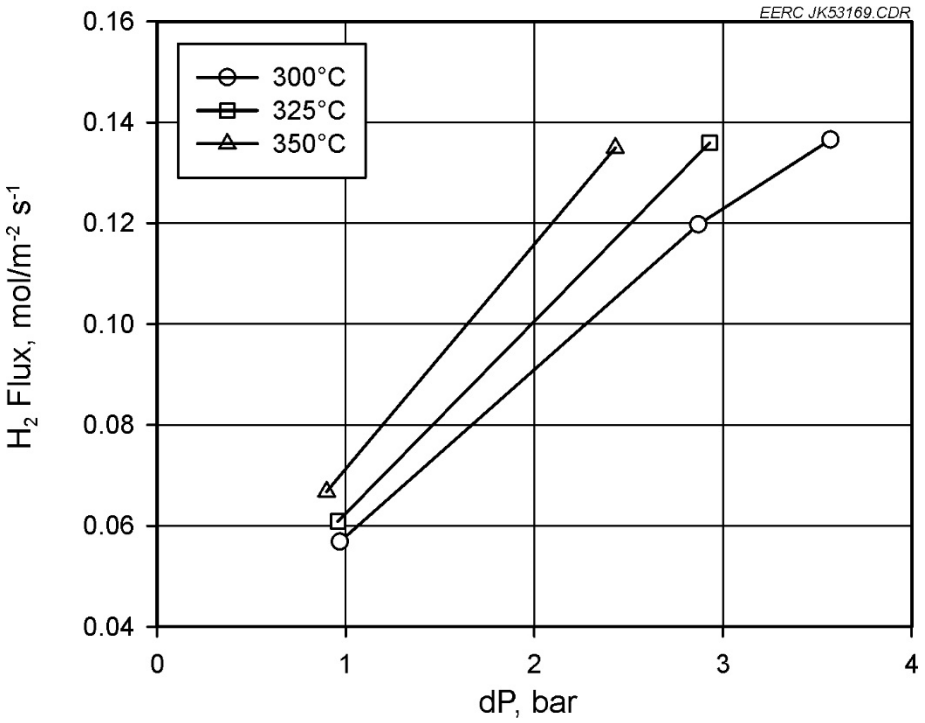

Figure 3-12. Hydrogen flux through 0.50-mm-thick Pd-coated vanadium separators with varying transmembrane pressure and temperature.

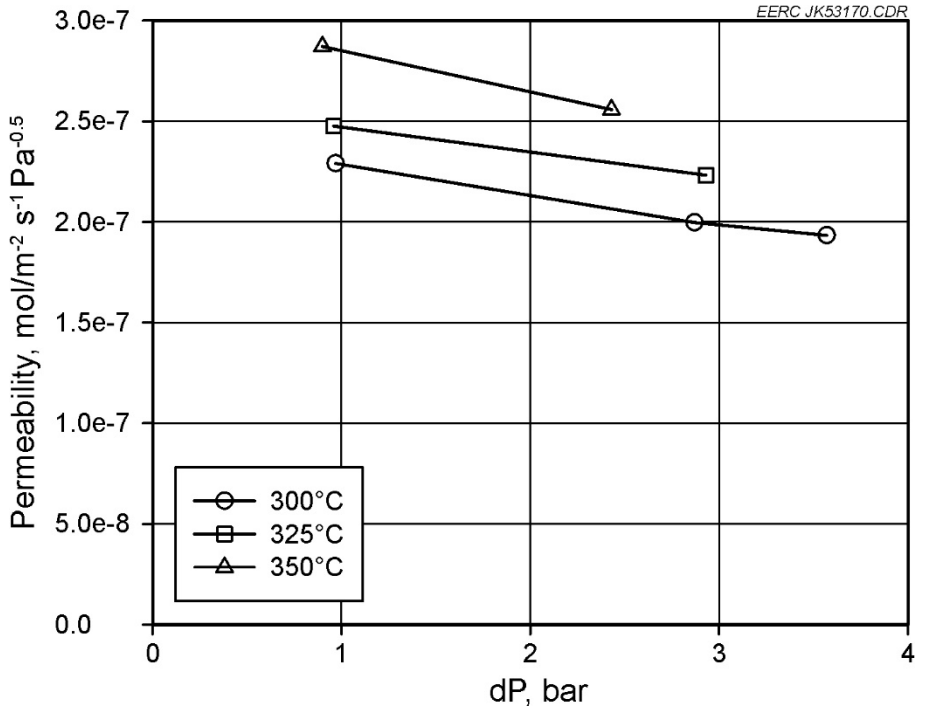

Figure 3-13. Hydrogen permeability of 0.50-mm-thick Pd-coated vanadium membranes with varying transmembrane pressure and temperature.

3.2.2 Fluid-Bed Gasifier

The EERC high-pressure FBG system was designed according to American Society of Mechanical Engineers (ASME) B31.3 Process Piping Code specifications. A design drawing of the main reactor is shown in Figure 3-14. The 3.0-in.-i.d. gasifier is capable of operation at a maximum operating pressure (MOP) of 6.9 MPa (1000 psig) at operational temperatures up to 843°C (1550°F). For temperatures up to 982°C (1800°F), the MOP is limited to 2.0 MPa (300 psig).

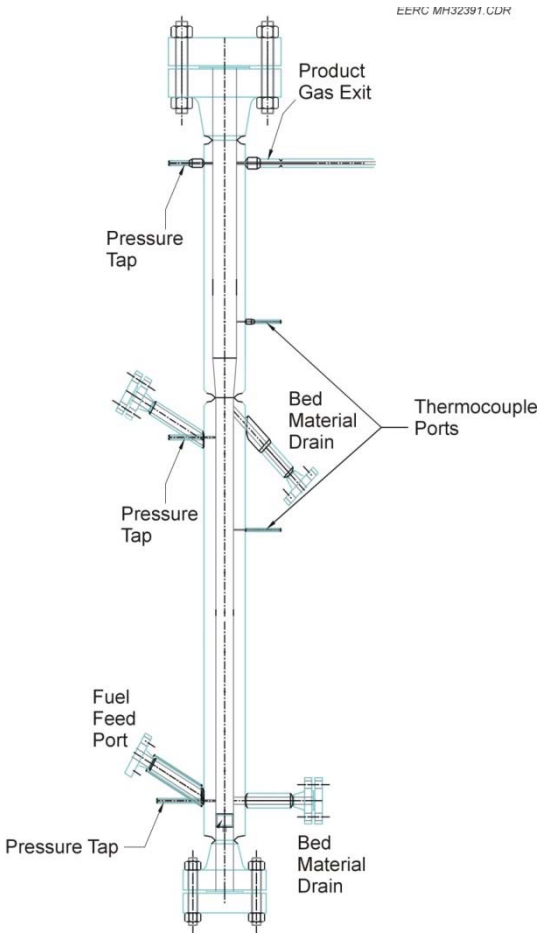

Figure 3-14. Design drawing of the pressurized fluidized gasification reactor.

The reactor uses an auger in the inclined feed port to promote fuel feed into the gasifier at a location immediately above the distributor plate. The distributor plate functions to support the bed material and reacting fuel and allows introduction of the reactant gases (e.g., steam, oxygen, and nitrogen). Ancillary gasifier systems include steam generation (high-pressure pump and electric superheater), and separate electric preheaters for recycle syngas and oxygen/nitrogen.

A cyclone and associated standpipe are used to capture and return coarse entrained reactor solids (degraded bed material, unreacted fuel, and ash) back to the reactor to facilitate enhanced fuel carbon conversion and maintain bed inventory. The solids collecting at the bottom of the recycle standpipe are reintroduced just above the reactor distributor plate using a horizontal auger. Bed material samples can be collected through sample pots located on the standpipe or 5 ft above the distributor plate.

The reactor, cyclone, and standpipe are externally, electrically heated to negate heat losses associated with the high surface area-to-volume ratio of a typical pilot-scale reactor system. The system is highly instrumented with thermocouples, pressure transducers, and mass flow measurement devices to guide system operations and maintain the system within safe operating limits.

The FBG is capable of feeding up to 9.0 kg/hr (20 lb/hr) of pulverized coal or biomass at pressures up to 70 bar absolute (1000 psig). The externally heated bed is initially charged from an independent hopper with silica sand or, in the case of high-alkali fuels, an appropriate fluidization media. Independent mass flow controllers meter the flow of nitrogen, oxygen, steam, and recycled syngas into the bottom of the fluid bed. Various safety interlocks prevent the inadvertent flow of pure oxygen into the bed or reverse flow into the coal feeder. Recycled syngas is injected several inches above the bottom distributor plate, which prevents direct combustion of syngas with oxygen entering at the bottom of the bed.

Coal is fed by a K-Tron® loss-in-weight, twin-screw feeder that provides instantaneous online measurement of the coal feed rate. The feeder is located in a pressure vessel and is capable of feeding at pressures up to 70 bar (1000 psig). The feed system's electronic controls are interfaced to a data acquisition system that allows for local or remote computer control of the fuel feed rate. Above the main feed hopper is the fuel charge lock hopper. The fuel charge hopper is manually charged with fuel through the top valve while at atmospheric pressure. It is then sealed and pressurized. Finally, the fuel feed material is transferred by gravity feed to the weigh hopper of the feeder. Metered coal from the feeder drops through a long section of vertical tubing and is then pushed quickly into the fluid bed through a downward-angled feed auger.

3.2.3 Warm-Gas Conditioning and Sampling Description

The product from the FBG flows through a warm-gas (230°–400°F) conditioning system, as seen in Figure 3-15, composed of a filter and fixed-bed reactors. The syngas passes through a hot candle filter to remove fine particulate. The filter has near-absolute filtration capability.

The warm-gas cleanup system was operated in a manner to achieve maximum H_2 and minimum CO concentration while maintaining acceptably low levels of H_2S. A train of up to seven fixed beds and an adsorbent transport reactor were available for conditioning of the syngas; however, only four fixed beds were necessary for this testing. All are externally heated and instrumented to facilitate accurate temperature monitoring and control. The beds can be loaded with WGS catalyst, heavy metal sorbent, chlorine sorbent, sulfur sorbent, and other materials, as

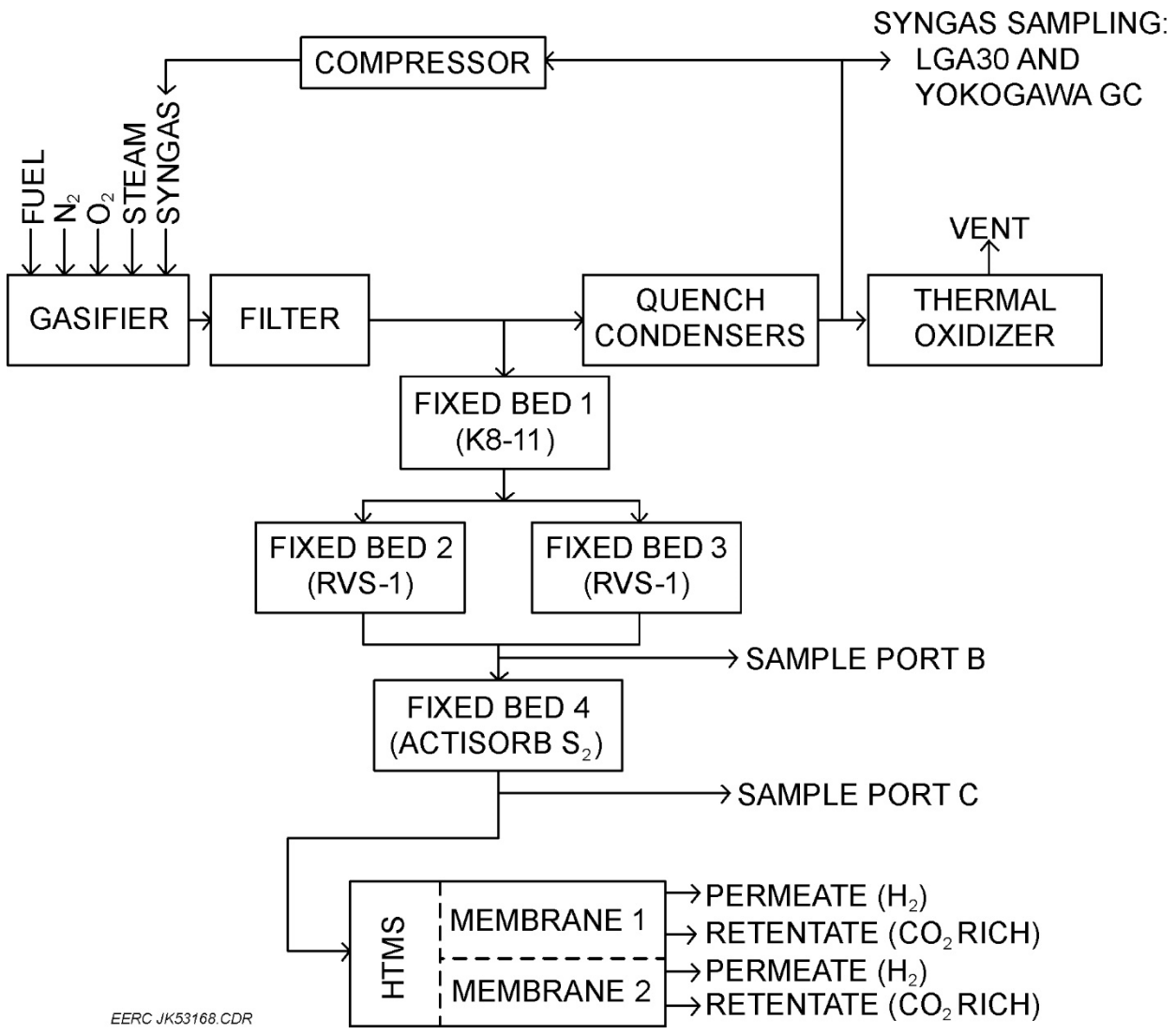

Figure 3-15. Gasification system process diagram.

needed. Referring to Figure 3-15, syngas flows through Fixed Beds 1–4. Slipstreams can be taken from any intermediate point between the filter and fixed beds, thereby promoting flexibility in the utilization of the warm-gas cleanup system.

The first fixed bed was used for WGS. WGS was achieved through the use of Johnson Matthey KATALCO$_{JM}$ K8-11 sour-gas shift catalyst to maximize hydrogen and minimize CO concentrations in the syngas. Observations during prior use of the K8–11 indicate that it may also crack tars. The K8-11 catalyst was reduced and conditioned prior to the start of the run. The first fixed bed operated at approximately 300°C. The feed gas to the HMTS was further conditioned in Fixed Beds 2–4. Süd-Chemie RVS-1 solid sorbent was used in Fixed Beds 2 and 3 to remove sulfur. RVS-1 is a regenerable sorbent that was originally developed by DOE NETL. RVS-1 has demonstrated H_2S <1-ppm operation at the EERC. Fixed Beds 2 and 3 were used in an alternating manner. Once one became saturated and sulfur breakthrough was observed, the other fixed bed

was brought online while the first was isolated for regeneration. Fixed Bed 4 was employed as a polishing bed and was loaded with new Actisorb S2 adsorbent. Actisorb S2 is produced by Süd-Chemie and is a nonregenerable ZnO-based adsorbent capable of removal of H_2S, mercaptans, and COS.

Feed gas to the HMTS is monitored through the use of continuous slipstream sampling at Port C, seen in Figure 3-15. Online analyzers are not capable of measuring high concentrations of water. Since the WGS reaction consumes some of the steam from the FBG's product gas, measurement of the actual water in the HMTS feed gas is necessary. The Port C analyzer slipstream is dried through the use of high-pressure condensers. The syngas flow through the condensers is set to approximately 0.57 scmh (20 scfh). Steam concentration in the feed gas is periodically quantified through the use of a dry gas meter to measure slipstream volumetric flow and condensed water. This technique permits the determination of the feed gas composition on a wet basis.

Dry gas is fed to a laser gas analyzer (LGA) and gas chromatograph (GC) for online analysis of major gas components and for low-level (ppb) analysis of sulfur species. The EERC has two GCs and up to six Atmosphere Recovery, Inc., LGAs available for use with the gasifiers. The LGAs employ Ramen detectors to stimulate sample gas and emit distinct light spectra. Four LGAs were used for these tests. The LGAs use designations LGA35, LGA39, LGA105, and LGA106. The LGAs are each capable of measuring the real-time concentrations of eight gases at once. Seven of those gases are H_2, CO, CO_2, N_2, H_2S, CH_4, and total hydrocarbons. LGA39, LGA105, and LGA106 are capable of measuring O_2 in addition to the suite of aforementioned gases and are normally dedicated to gasifier control and operation. LGA35 is capable of measuring H_2S instead of O_2. It is generally used to measure the gas compositions from various sample ports.

A Yokogawa GC is paired with LGA39. The Yokogawa GC is capable of measuring CO, CO_2, N_2, O_2, H_2S, COS, CH_4, ethane, ethene, propane, and propene. Referring to Table 3-2, the Yokogawa has high H_2S measurement capabilities and is better suited to syngas that has not had the H_2S removed. LGA35 is paired with a Varian 450 GC. The Varian GC is equipped with two thermal conductivity (TC) detectors and a pulsed-flame photometric detector for ultralow sulfur detection. The first TC detector is dedicated solely to analyzing hydrogen and provides three hydrogen measurements for each 15-minute analysis cycle. The second detector analyzes the gas stream for CO, CO_2, N_2, O_2, H_2S, COS, CH_4, ethane, ethene, propane, and propene. One measurement is provided every 15 minutes for each of those gases. The third detector is capable

Table 3-2. H_2S Detection Ranges

Analyzer	H_2S Detection Limits
LGA35	50–5000 ppm
LGA39	50–5000 ppm
LGA105	50–5000 ppm
LGA106	50–5000 ppm
Varian 450 GC	0.02–1 ppm and 50–3000 ppm
Yokogawa	>50 ppm
Dräger Tubes	0.2–6 ppm, 1–200 ppm, 100–2000 ppm

of ultralow sulfur detection, down to 50 ppb. It provides three H_2S and COS measurements for each 15-minute cycle. Table 3-2 summarizes the H_2S detection limits of the four analyzers used in this test.

The analyzers are calibrated prior to the start of and after each test program. Sample gas streams are manually switched via valves at the sample ports. LGA 39 and the Yokogawa GC were used to continuously monitor syngas produced by the FBG and control the operation of the FBG. LGA47 was used after the fixed beds to continuously monitor the gas composition supplied to the HMTS. LGA106 and LGA105 were used to monitor the gas composition of the permeate and retentate flows exiting the membrane assemblies. Periodic samples are taken from one membrane assembly at a time. The time duration for sampling is generally 1–2 hours. Sample gas tubing from sample ports to the analyzers is 316 SS, polyethylene (PE), polytetrafluoroethylene (PTFE), or fluorinated ethylene propylene (FEP), with no line longer than 25 m.

Sample gas transit times to the analyzers are estimated to be less than 1 minute, depending on the individual sample gas flow rate. Gas is cooled and quenched before transport to the analyzers, so measurements are on a dry basis. Analyzer sample locations are indicated in Table 3-3. Since two membrane assemblies were tested simultaneously, LGA105 was calibrated for high hydrogen concentrations and used for measurement of the permeate streams. LGA106 was calibrated for measurement of retentate streams.

Table 3-3. Analyzer Sample Locations

Analyzer	Gas Stream	Location
LGA39	FBG product gas	Gasifier exit
LGA47	Feed	Port C
LGA106	Permeate	Port E
LGA105	Retentate	Port D
Yokogawa	FBG product gas	Gasifier exit

In addition to analyzer sampling from various points throughout the system, Dräger tubes are used. H_2S, HCl, HCN, NH_3, and other trace gases can be checked to verify low-level chromatograph data. Dräger tube and gas bag samples may be drawn from each of the sample ports on the membrane skid as well as from several other ports on the gasifier system. Dräger tube sampling is typically performed most frequently at Sample Port B and other points downstream from the H_2S sorbent beds as a means of detecting the start of breakthrough and, thereby, maintaining appropriate H_2S exposures.

Because of the high temperature and pressure of the syngas supplied to the HTMS, direct measurement of H_2O is not feasible. A moisture-sampling system was employed to measure the fraction of water in the syngas supplied to the HTMS. A metering valve diverted a slipstream to a water-cooled indirect quench pot and a secondary ice bath to remove condensables from the syngas at sample Port C. Following the quench and ice bath, a gas regulator dropped the pressure to approximately 135 kPa (5 psig) and the dry syngas flow was measured with a dry gas meter. Syngas from the water balance system was sent to the Varian GC and LGA35 for real-time analysis. The condensing train was drained in 2- to 3-hour intervals, the recovered water was

weighed, and total volume of syngas taken during the sample interval was recorded from the dry gas meter.

3.2.4 Hydrogen Membrane Test System

The HMTS is capable of simultaneously testing multiple hydrogen separation membranes. The HMTS is composed of controlled heaters; purge gas mass flow controllers; water-cooled quench pots for gas cooling; retentate flow control; and instrumentation for temperature, pressure, flow measurement, and a highly instrumented control system. Figure 3-16 provides an example of instrumentation graphing. The HMTS uses a reconfigurable, high-speed data acquisition and control system. User control and data logging are via a remotely located personal computer. The control computer utilizes a custom-written program with a graphical user interface. The control program is usually modified to meet the specific needs of the test. Figure 3-17 shows the main HMTS control window used for testing two membranes. Three membranes have been simultaneously tested with the HMTS.

Flow measurement on the HMTS is done through the use of dry gas meters (DGMs). The DGMs are rated for 200 scfh (5.66 scmh) at 0 psig (101 kPa). Full-scale accuracy is 1% with 1/100 ft^3 resolution on the dial face of the meters. The meter shaft on each DGM is coupled to a high-resolution encoder, which is connected to the control system. DGM flows are averaged. Figure 3-17 shows an example two of the DGM trend windows.

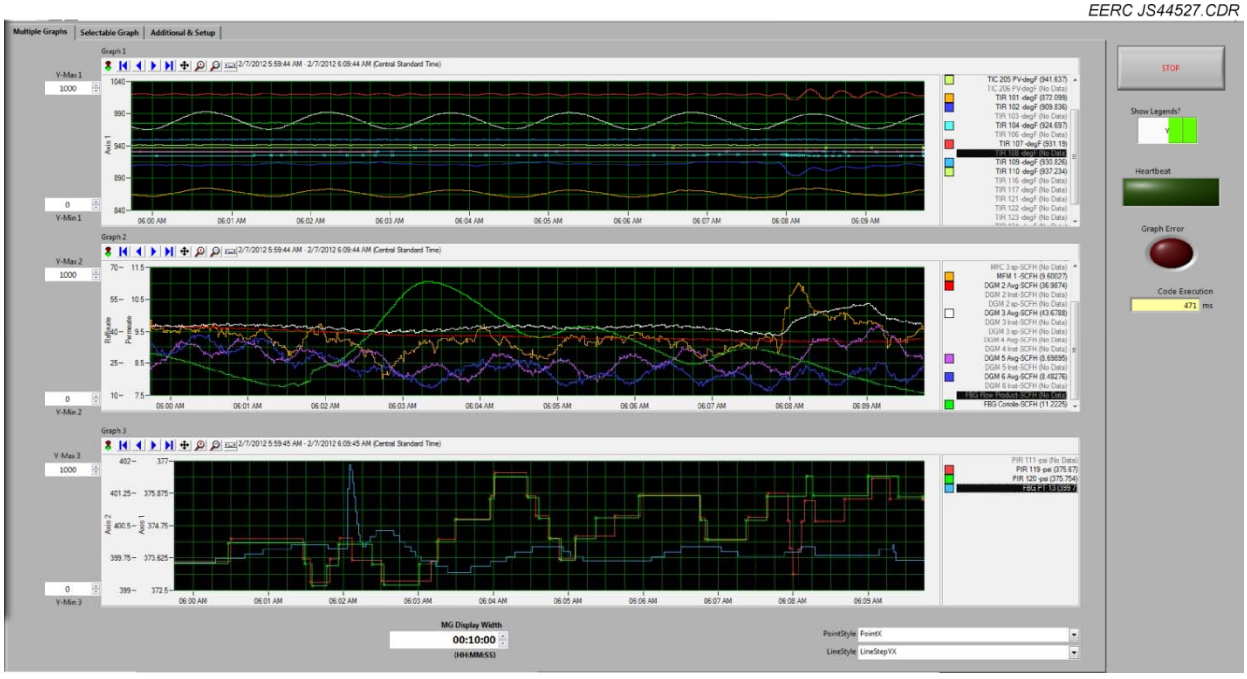

Figure 3-16. HMTS instrumentation trend graphing.

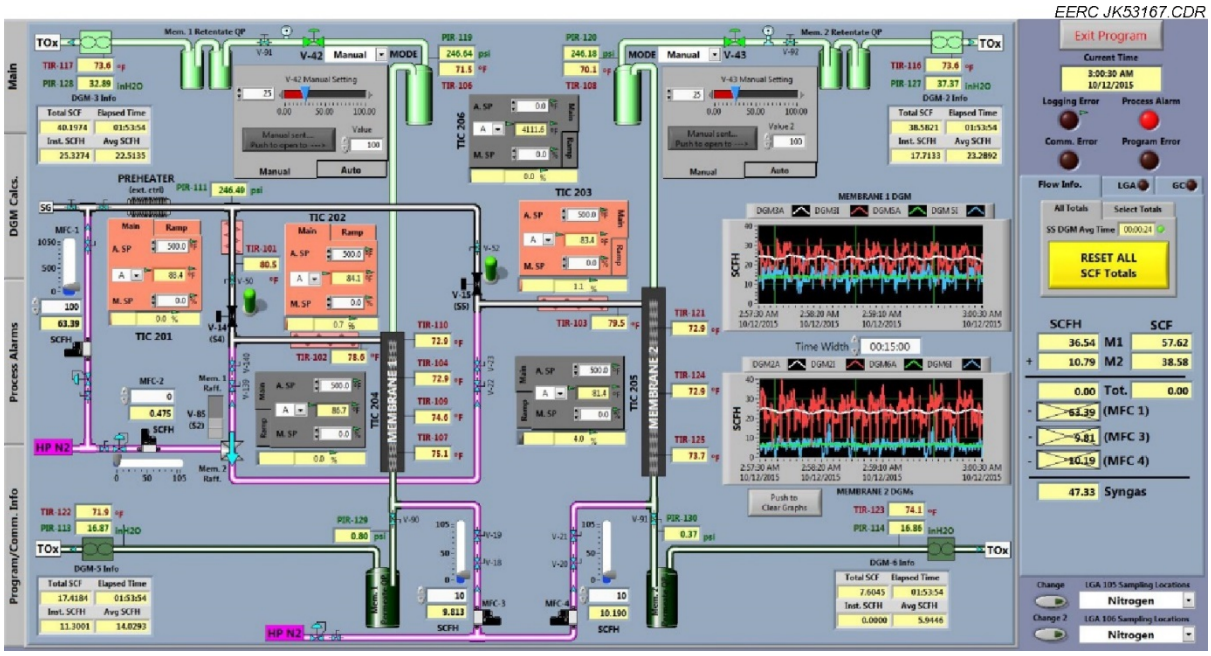

Figure 3-17. HMTS controls.

Figure 3-18 shows the piping and instrumentation diagram (P&ID) of the HMTS. The design of the HMTS allows for individual controlled purge flows to each side of a membrane as well as custom supply gas blending and transitioning. Retentate flow control is done through the use of high-accuracy, pneumatically actuated flow control valves. The flow coefficient of the valves may be changed by changing seat and stem. Heater controllers feature both ramp-up and ramp-down control. Pressure transmitters use a digital sensor, providing stable and precise pressure measurement. The pressure transmitter's CPU (central processing unit) directly counts the sensor output frequencies without any additional A/D (analog/digital) conversion.

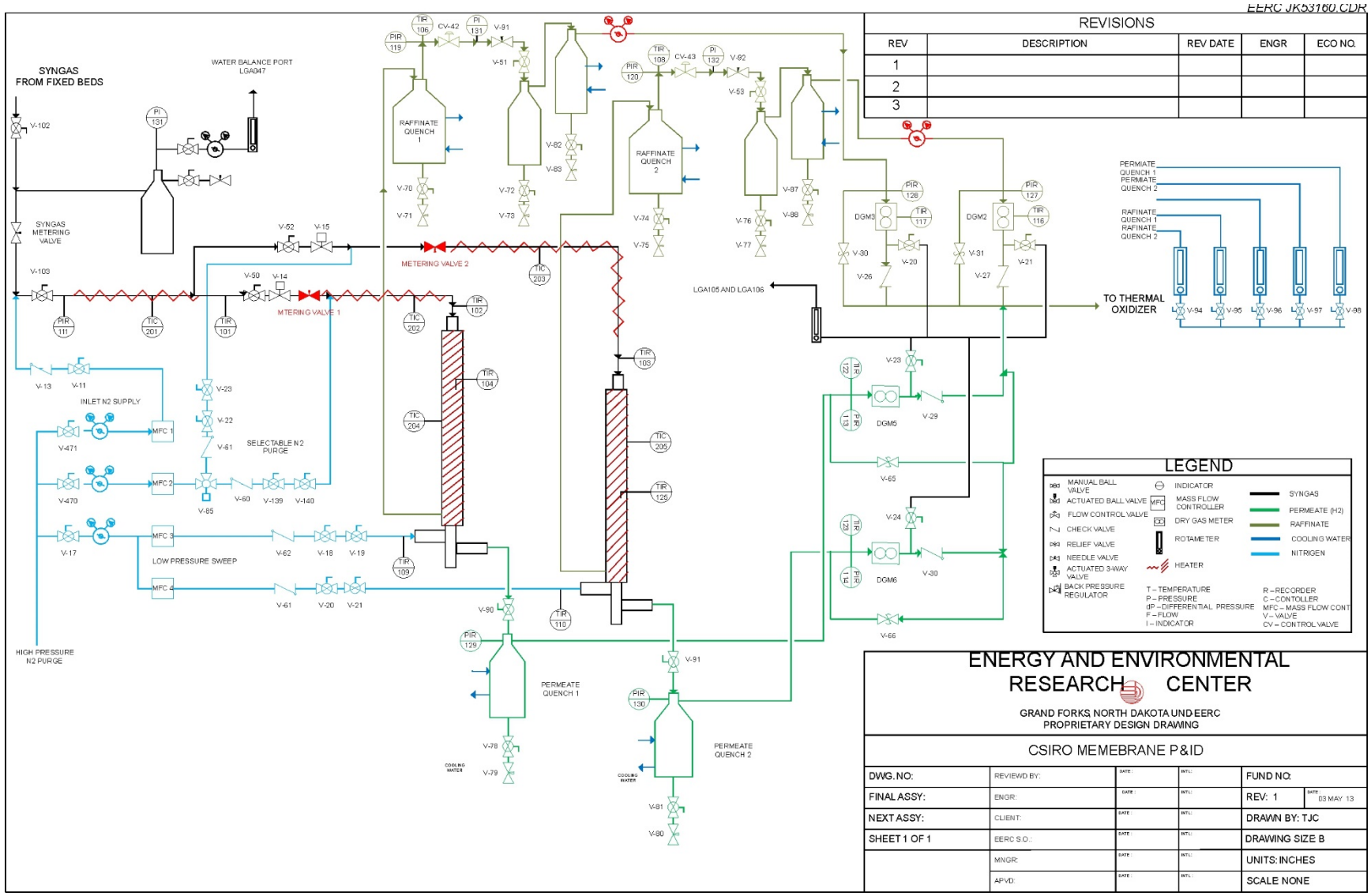

Figure 3-18. HMTS P&ID.

3.3 Testing Program

At the direction of CSIRO, a conservative approach was undertaken to observe the effects of coal-derived syngas on the separator tubes since these were the first tests using coal-derived syngas on the thin-wall separators. This conservative approach involved maintaining consistent pressures, temperatures, and flows. As a result, a parametric test matrix was not undertaken. Test Program H2M-017 was conducted during the week of July 25–29, 2016. Prior test programs were conducted using thicker-walled separators. These prior CSIRO separator test results are tabulated toward the end of this report, along with those of H2M-017, to provide a comparative view across the entire CSIRO testing program. The first test program, H2M-015, was conducted during the week of October 12–16, 2015, and the second test program, H2M-016, was conducted during the week of October 26–31, 2015.

The FBG was used to gasify North Dakota lignite coal from the Freedom Mine near Beulah, North Dakota. Originally, Australian brown coal from the Loy Yang Mine was discussed as the preferred feedstock. International transport issues prevented its use. An as-received sample of this fuel was submitted for proximate, ultimate, heating value, and x-ray fluorescence (XRF) analyses, with the results shown in Table 3-4. The Freedom coal was crushed to −10-mesh size and then air-dried for these tests to bring the moisture closer to the Loy Yang brown coal. The lower moisture also facilitates better fuel feeding into the FBG.

During each test program, the gasifier was first brought online independent of the back-end syngas-conditioning systems. During gasifier start-up, there was a chance that high-tar pyrolyzing conditions or oxygen breakthrough could occur. Once the gasifier was at steady-state conditions, Fixed Bed 1 was brought online to promote WGS, as discussed previously. The WGS catalyst used was presulfided Johnson Matthey KATALCO$_{JM}$ K8-11 sour shift catalyst. The slipstream flow of product gas from the FBG was routed through Fixed Bed 1 at a rate of approximately 50 scfh to match the anticipated flows of HMTS and the HMTS feed gas sampling. Excess syngas was routed to other back-end systems for concurrent testing or was vented through the FBG pressure control valves and then to the thermal oxidizer.

After the gasifier operation and WGS reactions were verified, the slipstream of syngas was sent through either Fixed Bed 2 or 3, with one online and the other on standby or regenerating. Each of these fixed beds contained regenerable, zinc-based RVS-1 sulfur adsorbent. Syngas was then sent through Fixed Bed 4, which was used as a polishing bed, and then to the HMTS. Fixed Bed 4 was loaded with Süd-Chemie ActiSorb S2, a nonregenerable sorbent capable of removing H_2S, thiophenes, mercaptans, and COS.

Syngas was allowed to flow through Sample Port C with a flow rate of approximately 0.57 scmh (20 scfm). The flow through Sample Port C went through high-pressure condensers which are used for bulk removal of water from the syngas. The steam component of the syngas was determined as a function of the totalizing dry gas meter, time duration, condensed water measurement, temperature measurement, pressure measurement, and LGA35 dry syngas composition measurement. Sample Port B was also used for Dräger tube measurements

Table 3-4. Freedom Mine Coal Analysis

	As Received
Proximate, wt%	
Ash	3.77
Fixed Carbon	31.94
Moisture	37.00
Volatile Matter	27.29
Ultimate, wt%	
Ash	3.77
Carbon	41.98
Hydrogen	7.04
Nitrogen	0.57
Oxygen	45.95
Sulfur	0.69
Heating Value, Btu/lb	7091
XRF, wt%	
AL_2O_3	9.38
BaO	0.27
CaO	20.17
Fe_2O_3	7.63
K_2O	0.44
MgO	8.98
MnO	0.09
Na_2O	3.22
P_2O_5	0.41
SiO_2	14.45
SO_3	21.11
SrO	0.58
TiO_2	0.19

downstream from the fixed beds. H_2S was the molecule of critical concern for these measurements. A Dräger tube was used for indications of H_2S concentrations. These tubes have a range of 0.2–6 ppm, using n=1 pump of the calibrated Accuro® sample pump. If no indication was obtained after one pump, multiple pumps were sometimes drawn until an indication was observed. The objective was to keep the H_2S level entering Fixed Bed 4 (ActiSorb S2) to less than 4 ppm. If the H_2S concentration was observed to be trending up, a switch between Fixed Beds 2 and 3 was made. The fixed bed coming offline was then regenerated.

Two membrane assemblies were loaded into the HMTS and tested simultaneously. The assemblies consist of the housing, external feed gas heat exchanger coil, thermocouples, membrane tube (separator), and compression fittings. The housings were disassembled for installation of the separator through the use of compression fittings. Personnel wore rubber gloves when handling the separator tube to reduce the risk of surface contamination. The HMTS assembly locations were designated Membrane 1 and Membrane 2. Each membrane assembly was installed in a separate clam shell heater. An assembly could be removed from the HMTS independent of the other's

operation for replacement of the separator tube, if needed. The membrane assemblies were slowly pressurized with N_2 and then checked for leaks. Nitrogen flow was established with the retentate flow rates set to approximately 0.57–0.71 scmh (20–25 scfh) of nitrogen. Nitrogen purge flows through the permeate side of each membrane assembly were set at approximately 0.14 scmh (5 scfh). The membrane assemblies were then heated to their operating temperatures using ramp control. Heat-traced feed lines were adjusted to balance temperatures as the target temperatures were approached. Once stable target temperatures were achieved, the nitrogen purges to the permeate side of the assemblies were discontinued and baseline leak rates to the permeate side were determined. Adjustments were made to the N_2 feed pressure such that it was equal to the syngas pressure. Syngas was fed to the membranes while N_2 to the feed was discontinued. Initially, manual transition from N_2 to syngas was attempted. Later, in an attempt to provide better start-up dilution, the fixed beds were filled with nitrogen and syngas was then allowed through the fixed beds to the HMTS. Retentate flows and temperatures were monitored and adjusted as necessary. Permeate flows and compositions were monitored for indications of membrane leaks and failures. Periodic calculations were performed as an approximate indication of performance.

Membranes were taken offline by supplying preheated N_2 feed while discontinuing syngas feed. No attempt was made to gradually transition to N_2. The N_2 feed flow rate was maintained at approximately 0.57–0.71 scmh (20–25 scfh). The permeate flow was monitored for an indication of leaking across the separator and seals. The permeate side of the membrane assembly was purged with preheated N_2 at approximately 0.14 scmh (5 scfh). Temperatures were ramped down to ambient followed by a gradual reduction in pressures. Once down to near-ambient temperature and pressure, N_2 flows were discontinued. It should be noted that standard conditions used were 15.6°C (60°F) and 101 kPa (14.7 psig).

3.3.1 Test Program H2M-017

The objective of testing during H2M-017 was to subject the separators to syngas for the maximum possible time and observe their performance characteristics. CSIRO specified 320°–330°C (608°–626°F) as the target temperatures for membrane assemblies. The target feed flow rate for the separators was 0.71–0.0.85 scmh (25–30 scfh). The target feed pressure was 10 bar (130 psig) throughout.

Overall, gasification with the lignite fuel produced syngas quality similar to that experienced in previous FBG tests with similar feedstocks. The carbon conversions were somewhat lower because of operation at lower O_2/fuel ratios. The lower O_2/fuel ratios were chosen based on the potential of generating bed agglomerates. The HMTS was operated concurrently with the EFG and $DeSNO_x$ system. The EFG was operating in combustion mode to simulate high-temperature oxy-fired combustion with flue gas recycle conditions. The $DeSNO_x$ system was employed to demonstrate high-pressure impurity removal from the combustion flue gas stream. Because of the small hydrogen separator sizes, the HMTS was using only a small slipstream portion of the syngas produced by the FBG, whereas the EFG and $DeSNO_x$ system was capable of using all the syngas.

Average gasifier operating conditions for H2M-017 can be seen in Table 3-5.

Table 3-5. Average Gasifier Operating Conditions for H2M-017

Start Date:	10/15/2015	
Start Time:	13:00	
End Date:	10/16/2015	
End Time:	01:00	
FBG Temperatures	°F	°C
O_2/Steam Inlet	560	293
Recycle Inlet	898	481
Lower Reactor Bed	1535	835
Upper Freeboard	1544	851
Reactor Extension	1318	714
Cyclone Exit	1159	626
Filer Vessel Average	755	402
Flows	lb/hr	kg/hr
Fuel Feed Rate	9.56	4.34
Steam	21.6	9.80
Recycle Syngas	63.6	28.8
	scfh	slph
Oxygen	63.2	1789
Syngas Purges	145	4106
Product Gas	129	3652
Pressures	psig	kPa
Gasifier	298	2155
Filter Vessel	293	2221
Quench Pot	287	2080
Recycle Gas Surge Tank	448	3190

The composition of the feed gas is shown in Figure 3-19. It can be seen that there were significant challenges in maintaining consistent feed gas composition. Operational issues associated with the gasifier system stemmed from fouling of the cyclone and breaking of a filter. The HMTS was online during the two periods between the thick black vertical lines. The analyzers utilize gas-conditioning condensers to avoid water saturation and tar fouling. As a result, the analyzers return values on a dry basis. To determine the water content in the feed gas, a sample stream of wet feed gas was routed through a pair of condensers. The volume of gas and mass of water were periodically measured on a timed basis and logged. During postprocessing, the moisture content of the feed gas was determined and added back into the dry gas analyses to arrive at the wet gas compositions. This accounts for the appearance of step changes in the water content of the feed gas.

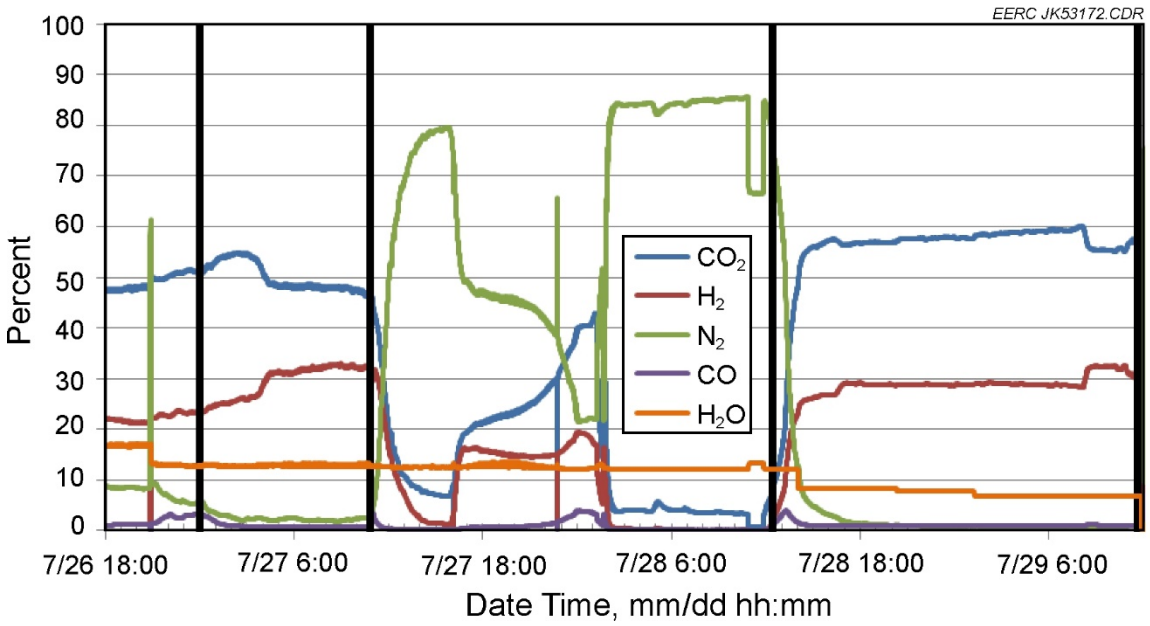

Figure 3-19. Feed gas composition for H2M-017.

Table 3-6 summarizes the location on the HMTS, CSIRO separator numbers, feed gas type, and test periods. Changes in the feed gas composition were a result of changes in FBG operation. Two membrane assemblies were installed in the HMTS on July 26, 2016. The Membrane 1 assembly contained Separator Tube 268, and the Membrane 2 assembly contained Separator Tube 265. The membrane assemblies were preheated to 325°C (617°F), with approximately 0.57 scmh (20 scfh) of nitrogen through each assembly. The fixed beds were brought online, and syngas flow was established to Sample Port C and the water balance system. H_2S levels were monitored with Dräger tubes, and levels were observed at less than 1 ppm. The membranes were adjusted to match the system pressure; N_2 flow was manually reduced while allowing syngas flow to increase.

Table 3-6. H2M-017 Membrane Assemblies, Separator Numbers, Feed Gas, and Test Periods

Membrane Location	CSIRO Separator No.	Feed	Start Date	Start Time	End Date	End Time	Duration hh:mm
1	268	Syngas	7/27/16	00:00	7/27/16	10:50	10:50
1	267	Syngas	7/28/16	12:25	7/29/16	11:36	23:21
2	265	Syngas	7/27/16	00:00	7/27/16	10:50	10:50
2	266	Syngas	7/28/16	12:25	7/29/16	11:36	23:21

Figures 3-20 and 3-21 show the temperature and pressures of Separators 268 and 265, respectively. Both indicate an internal temperature spike of more than 100°C as syngas was introduced. The increase in temperature is due to rapid hydrogen penetration into the separator's matrix. The hydrogen penetration also causes rapid expansion of the separators. Prior testing of CSIRO's thicker separators often resulted in catastrophic failure or development of leaks due to internal stresses caused by the rapid introduction of hydrogen-rich syngas. The thin-wall separators, demonstrated during H2M-017, produced high-temperature spikes upon exposure to hydrogen but also showed much better resiliency during start-up, with no evidence of leaks during operation. Permeate gas compositions remained at 100% for thin-wall separators. During operation of the HMTS, pressures fluctuated because of the need to manually adjust feed pressure regulators and flow control valves. Separators 268 and 265 were taken off-line on July 27 at 10:50 because of plugging of the FBG cyclone and a broken filter. After transitioning back to nitrogen, the HMTS was not being monitored closely. During this period, Separators 268 and 265 were subjected to abrupt pressure and temperature loss, resulting in cracking. Flows of nitrogen purge gas through to the permeate side increased dramatically as a result of the cracking (Figures 3-22 and 3-23). The permeate analyzer was not online at the time the leaks occurred. An example of one of the cracked separators is shown in Figure 3-24.

Separators 268 and 265 were replaced with Separators 267 and 266. A different technique of providing better start-up gas transitioning was used by filling the entire fixed-bed system with nitrogen and then opening the fixed-bed system syngas inlet valve while turning off the nitrogen purge. A more controlled and gradual transition from nitrogen to syngas was achieved. As a result, the start-up temperature spikes were reduced by approximately 50°C (Figures 3-25 and 3-26).

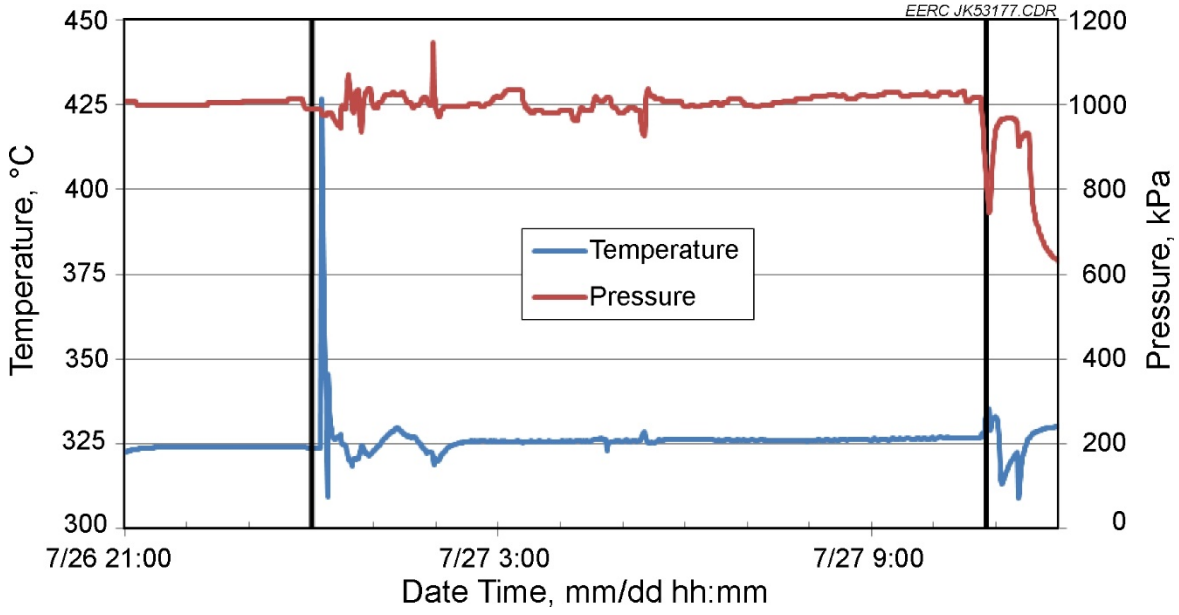

Figure 3-20. Temperature and pressure of Separator 268.

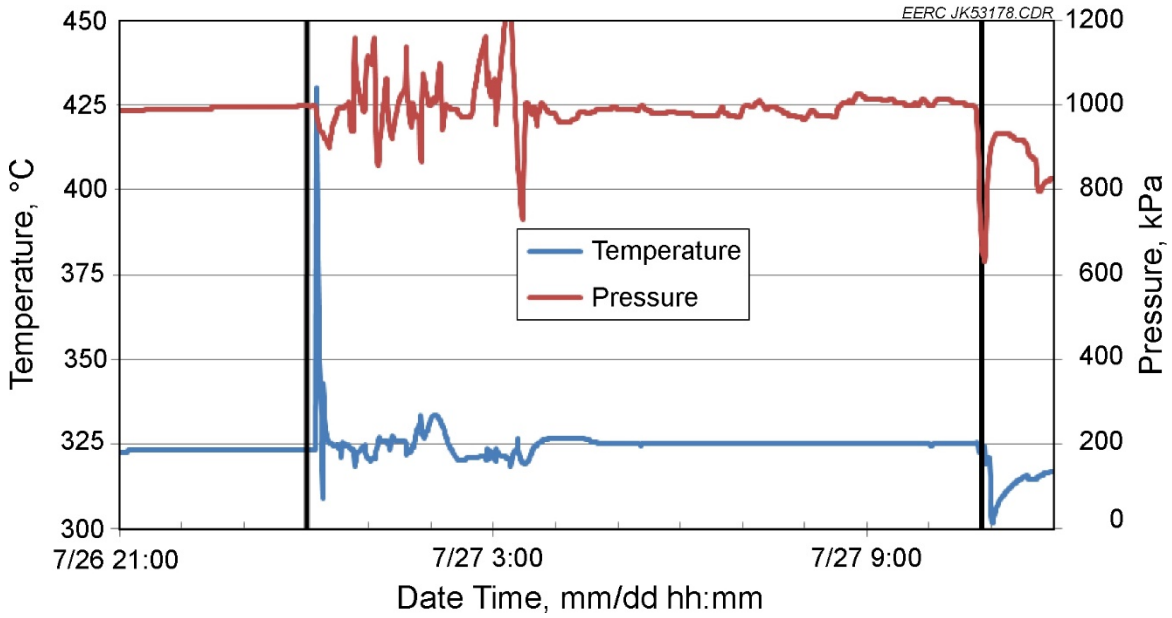

Figure 3-21. Temperature and pressure of Separator 265.

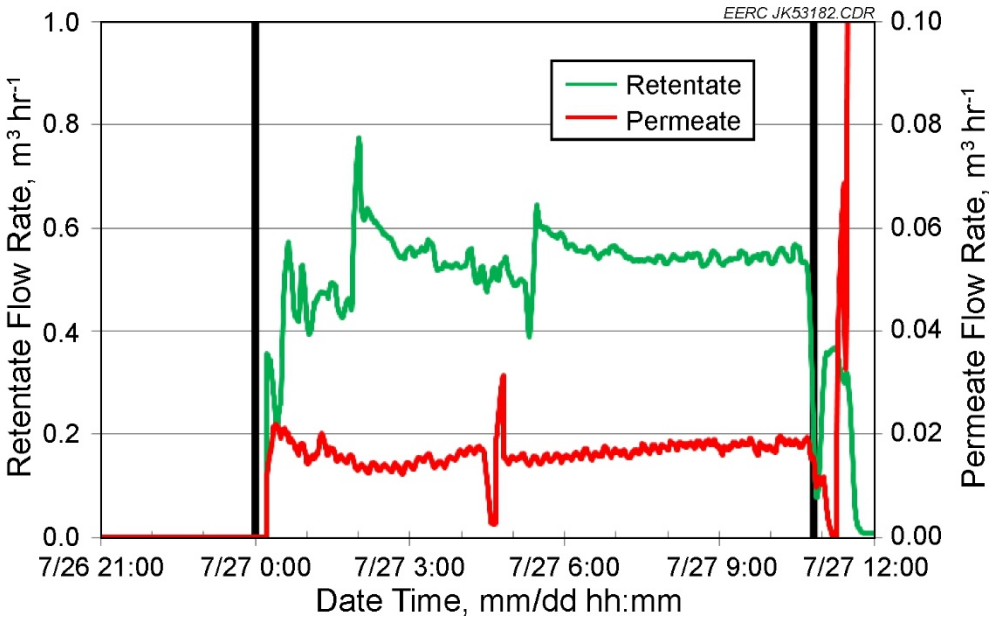

Figure 3-22. Flows of Separator 268.

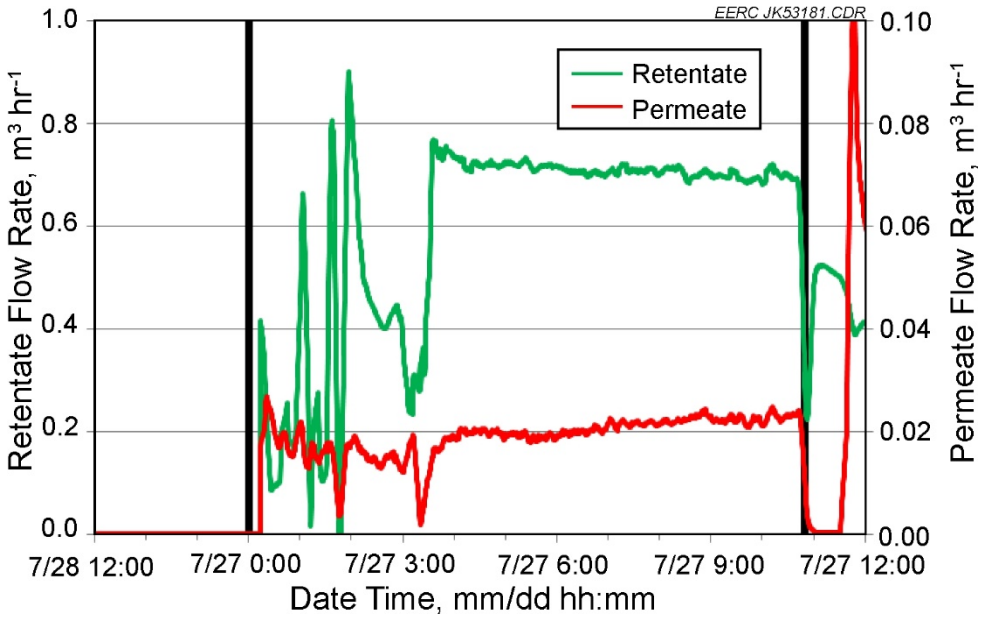

Figure 3-23. Flows of Separator 265.

Figure 3-24. Crack in Separator 268.

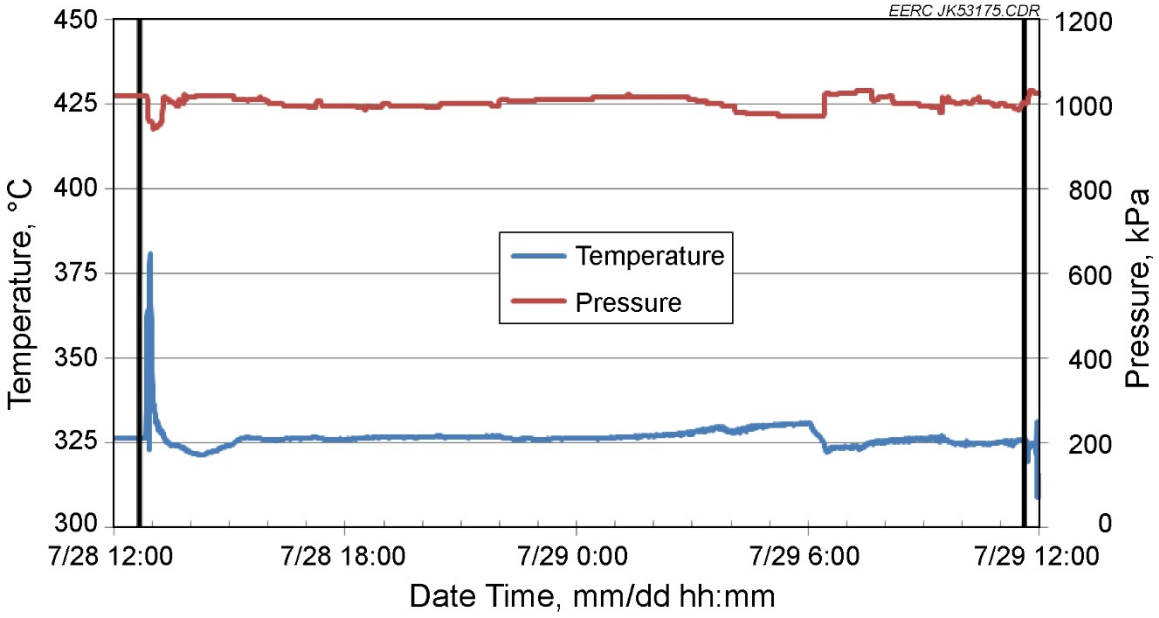

Figure 3-25. Temperature and pressure of Separator 267.

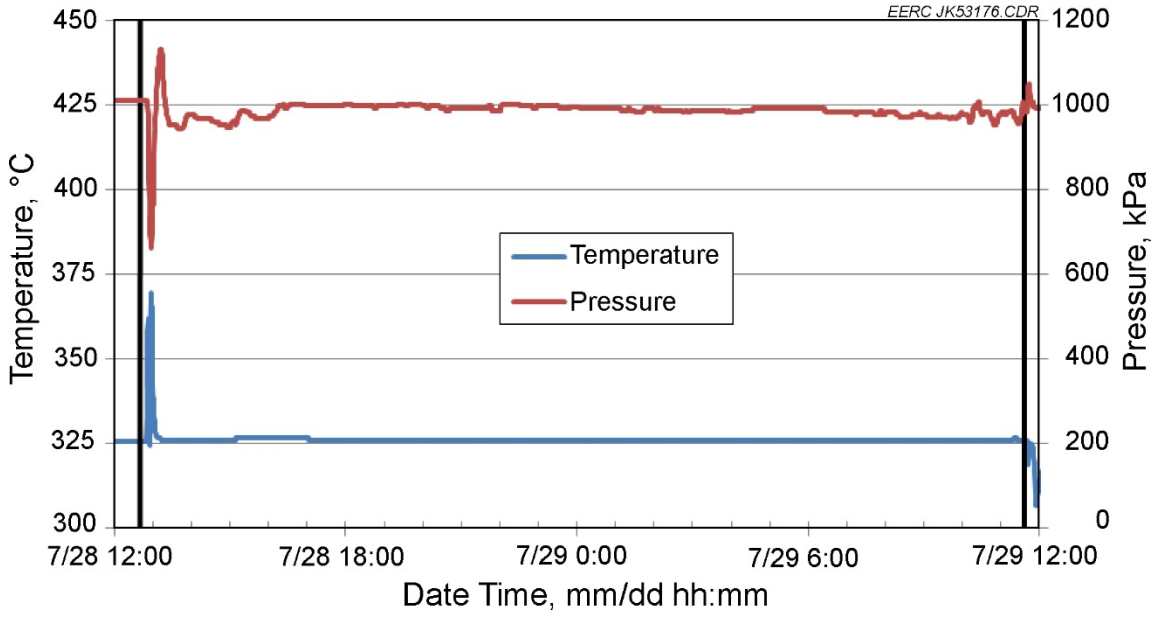

Figure 3-26. Temperature and pressure of Separator 266.

The retentate and permeate flows are shown in Figures 3-27 and 3-28. The retentate flow of Separator 267 was very inconsistent because of tar accumulation in the flow control valve. Permeate flows of both Separator 267 and 266 increased near the end of testing because of a change in gasifier operating conditions that resulted in increased H_2 in the feed gas, as seen in Figure 3-19. As with Separators 268 and 265, Separators 267 and 266 remained leak-free throughout their operation. The spike in permeate flows after completion of the test period was due to the use of nitrogen purge gas.

Table 3-7 shows the steady-state periods, with H2M-017 near the bottom. Each run number (H2M-015, H2M-016, or H2M-017) is followed by the separator number, the steady-state period number associated with the separator, the separator's location in the test rig, the feed gas and, finally, the steady-state times. The first two runs (H2M-015 and H2M-016) utilized separators with a 500-µm-thick vanadium support structure with a 1-µm Pd layer. In comparison, H2M-017 used separators with a 250-µm-thick vanadium support with 0.5-µm 100% Pd and 70%–30% Pd–Au membrane layers. Table 3-8 shows the operating conditions during the steady-state periods. No sweep gas was used to enhance the partial differential pressure on the permeate side of the membrane.

Table 3-9 summarizes performance data for all CSIRO H_2 separators tested at the EERC. The last line in the table includes performance data from a large separator assembly that was previously tested at the EERC for purposes of comparison. Because of limited operating conditions, the pressure exponent was not optimized for performance calculations. Therefore, in all cases, the pressure exponent used was assumed to be n = 0.5. The CO_2 concentration factor represents the separator's ability to concentrate CO_2 in the syngas, which could be interpreted as a percent increase. The separators tested in H2M-017 were leak-free.

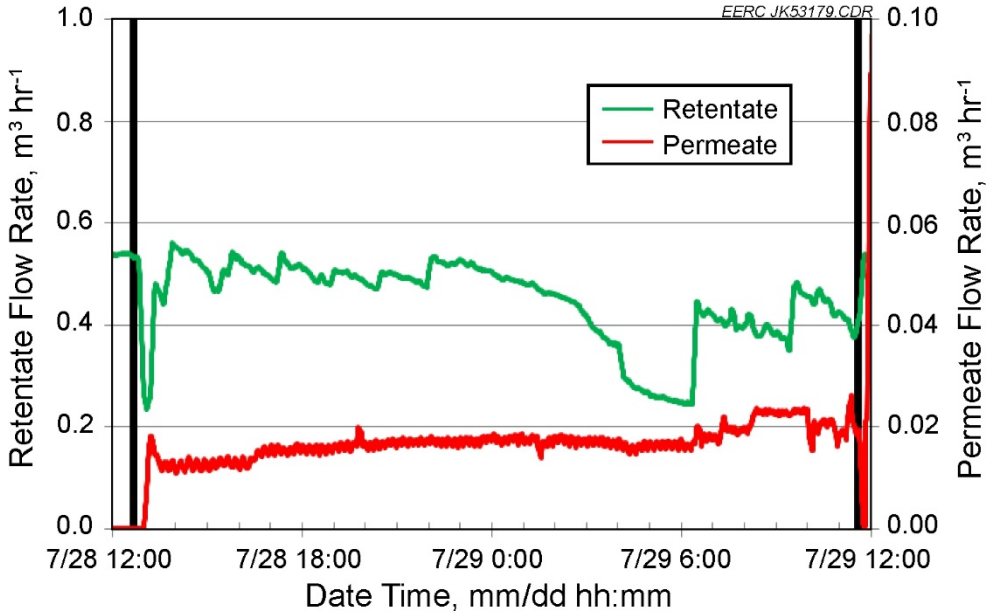

Figure 3-27. Flows of Separator 267.

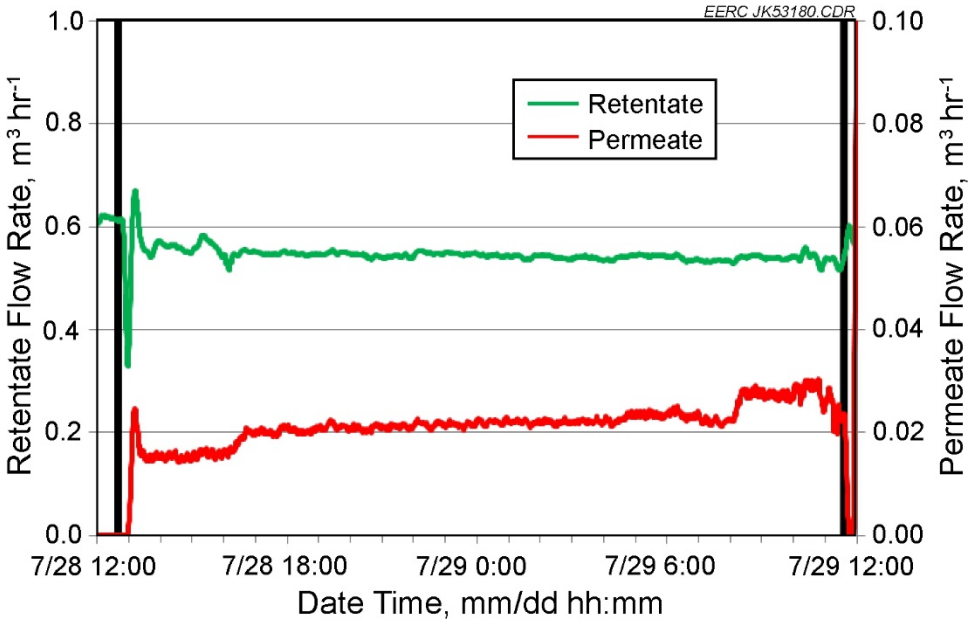

Figure 3-28. Flows of Separator 266.

Table 3-7. Steady-State Periods

Run No.	CSIRO Separator No.	Steady-State Period	Membrane Location	Feed	Steady-State Times				
					Start Date	Start Time	End Date	End Time	Duration, hh:mm
H2M-015	213	1	1	Hydrogen	10/13/15	13:10	10/13/15	13:45	0:35
H2M-015	211	1	1	Hydrogen	10/15/15	12:03	10/15/15	12:18	0:15
H2M-015	209	1	1	Syngas	10/15/15	16:43	10/16/15	1:35	8:52
H2M-015	212	1	2	Hydrogen	10/13/15	13:10	10/13/15	13:45	0:35
H2M-015	210	1	2	Hydrogen	10/15/15	12:03	10/15/15	12:51	0:48
H2M-015	210	2	2	Syngas	10/15/15	12:56	10/15/15	14:53	1:57
H2M-015	208	1	2	Syngas	10/15/15	16:43	10/16/15	1:35	8:52
H2M-016	207	1	1	Syngas	10/27/15	14:38	10/28/15	11:08	20:30
H2M-016	207	2	1	Syngas	10/28/15	16:07	10/30/15	6:58	38:51
H2M-016	207	3	1	Syngas	10/30/15	9:51	10/31/15	8:10	22:19
H2M-016	207	4	1	Syngas	10/31/15	10:36	10/31/15	12:08	1:32
H2M-016	206	1	2	Syngas	10/28/15	19:48	10/29/15	11:55	16:07
H2M-016	206	2	2	Syngas	10/29/15	14:18	10/30/15	6:28	16:10
H2M-016	218	1	2	Syngas	10/30/15	12:48	10/31/15	0:10	11:22
H2M-016	218	2	2	Syngas	10/31/15	0:15	10/31/15	9:01	8:46
H2M-017	268	1	1	Syngas	7/27/16	1:33	7/27/16	3:38	2:05
H2M-017	268	2	1	Syngas	7/27/16	4:55	7/27/16	10:29	5:34
H2M-017	267	1	1	Syngas	7/28/16	14:36	7/28/16	16:22	1:46
H2M-017	267	2	1	Syngas	7/28/16	16:55	7/29/16	7:49	14:54
H2M-017	267	3	1	Syngas	7/29/16	8:48	7/29/16	10:00	1:12
H2M-017	265	1	2	Syngas	7/27/16	4:31	7/27/16	10:29	5:58
H2M-017	266	1	2	Syngas	7/28/16	14:36	7/28/16	16:22	1:46
H2M-017	266	2	2	Syngas	7/28/16	16:55	7/29/16	7:49	14:54
H2M-017	266	3	2	Syngas	7/29/16	8:48	7/29/16	10:46	1:58

Table 3-8. Operating Conditions

Run No.	CSIRO Separator No.	Steady-State Period	Feed Pressure, kPa	Retentate Flow, sm^3/hr	Retentate H_2 Conc., mol%	Membrane Temp., °C	Permeate Flow, sm^3/hr	Permeate Pressure, kPa	Feed H_2 Conc. (wet basis), mol%	Permeate H_2 Conc. (wet basis), %	Augment H_2 Flow, sm^3/hr	Feed Flow, sm^3/hr	Leaking Gas Fraction, %	Feed H_2 Partial Pressure, kPa	Permeate H_2 Partial Pressure (leak-free basis), kPa	H_2 Partial Pressure Difference (leak-free basis), kPad
H2M-015	213	1	1159	0.000	100.0	315	0.057	102.0	100.0	100.0	0.212	0.269	ND	1159	102	1057
H2M-015	211	1	498	0.000	100.0	313	0.062	102.0	100.0	100.0	0.142	0.204	ND	498	102	396
H2M-015	209	1	2880	0.694	20.4	300	0.007	101.4	18.2	ND	0.000	0.700	ND	524	ND	ND
H2M-015	212	1	1159	0.000	100.0	336	0.068	102.0	100.0	100.0	0.187	0.255	ND	1159	102	1057
H2M-015	210	1	498	0.000	100.0	344	0.062	102.0	100.0	100.0	0.130	0.193	ND	498	102	396
H2M-015	210	2	2871	0.739	25.0	326	0.099	103.4	18.2	37.5	0.000	0.838	81.3	523	39	484
H2M-015	208	1	2877	0.702	20.5	326	0.008	101.9	20.7	87.8	0.000	0.710	15.9	595	89	505
H2M-016	207	1	2199	0.903	26.3	327	0.014	102.2	27.1	76.7	0.000	0.917	33.1	597	78	518
H2M-016	207	2	2201	0.691	24.8	350	0.027	102.3	26.7	97.4	0.000	0.718	3.1	588	100	489
H2M-016	207	3	2198	0.802	24.2	350	0.030	102.2	26.2	100.0	0.000	0.832	0.2	576	102	474
H2M-016	207	4	2195	0.744	23.4	373	0.097	102.6	25.8	47.2	0.000	0.841	70.9	567	48	518
H2M-016	206	1	2201	0.705	26.0	301	0.031	101.7	27.0	55.5	0.000	0.735	59.8	595	56	538
H2M-016	206	2	2200	0.610	23.7	352	0.040	101.4	26.3	83.1	0.000	0.651	20.9	578	84	494
H2M-016	218	1	2197	0.839	23.5	352	0.041	100.4	26.2	100.0	0.000	0.880	0.1	576	100	476
H2M-016	218	2	2198	0.577	22.9	349	0.036	100.4	26.2	99.2	0.000	0.613	1.4	577	100	477
H2M-017	0	1	1008	0.434	24.2	325	0.014	96.9	25.8	100.0	0.000	0.449	0.0	260	97	163
H2M-017	2	2	1011	0.707	30.7	326	0.017	102.8	32.0	100.0	0.000	0.724	0.0	323	103	221
H2M-017	0	1	1013	0.557	25.2	325	0.013	102.8	26.4	100.0	0.000	0.569	0.0	268	103	165
H2M-017	1	2	1002	0.544	26.1	327	0.017	102.7	28.8	100.0	0.000	0.561	0.0	289	103	186
H2M-017	1	3	999	0.540	28.8	326	0.023	98.0	32.4	100.0	0.000	0.563	0.0	324	98	226
H2M-017	1	1	1011	0.708	30.6	326	0.017	103.0	31.9	100.0	0.000	0.724	0.0	323	103	220
H2M-017	1	1	1013	0.557	25.2	325	0.013	102.8	26.4	100.0	0.000	0.569	0.0	268	103	165
H2M-017	0	2	1002	0.544	26.1	327	0.017	102.7	28.8	100.0	0.000	0.561	0.0	289	103	186
H2M-017	2	3	1002	0.542	28.8	325	0.022	99.4	32.3	100.0	0.000	0.564	0.0	324	99	224

ND = no data.

Table 3-9. Separator Performance Data

Run No.	CSIRO Separator No.	Steady-State Period	H_2 Flux Flow (leak-free basis), scmh	H_2 Flux (leak-free basis) mol/(m^2*s)	H_2 Permeance (leak-free basis) mol/ (m^2*s Pa$^{0.5}$)	H_2 Flux at 689.5 kPad (DOE 100 psid) (leak-free basis) mol/(m^2*s)	H_2 Flux at 689.5 kPad (DOE 100 psid) Sievert's Law (leak-free basis) mol/(m^2*s)	H_2 Recovery (leak-free basis), %	CO_2 Concentration Factor, wet basis
H2M-015	213	1	0.057	0.0729	6.90E-05	4.76E-02	2.09E-02	21.1	ND
H2M-015	211	1	0.062	0.0802	2.03E-04	1.40E-01	4.50E-02	30.6	ND
H2M-015	209	1	ND	ND	ND	ND	ND	ND	ND
H2M-015	212	1	0.068	0.0875	8.28E-05	5.71E-02	6.60E-02	26.7	ND
H2M-015	210	1	0.062	0.0802	2.03E-04	1.40E-01	1.19E-01	32.4	ND
H2M-015	210	2	0.037	0.0479	9.89E-05	6.82E-02	5.20E-02	16.7	ND
H2M-015	208	1	0.007	0.0093	1.84E-05	1.27E-02	1.12E-02	4.8	ND
H2M-016	207	1	0.011	0.0139	2.68E-05	1.85E-02	1.61E-02	4.3	1.0358
H2M-016	207	2	0.026	0.0338	6.92E-05	4.77E-02	4.28E-02	13.3	1.0613
H2M-016	207	3	0.030	0.0384	8.11E-05	5.59E-02	4.99E-02	13.4	1.0714
H2M-016	207	4	0.046	0.0589	1.14E-04	7.84E-02	6.32E-02	20.8	1.0682
H2M-016	206	1	0.017	0.0221	4.10E-05	2.83E-02	2.36E-02	8.5	1.0477
H2M-016	206	2	0.033	0.0431	8.72E-05	6.01E-02	5.23E-02	18.8	1.0740
H2M-016	218	1	0.041	0.0533	1.12E-04	7.72E-02	6.88E-02	17.3	1.0668
H2M-016	218	2	0.036	0.0462	9.68E-05	6.68E-02	5.94E-02	21.3	1.0829
H2M-017	268	1	0.014	0.0185	1.13E-04	7.82E-02	5.32E-02	12.0	1.0537
H2M-017	268	2	0.017	0.0217	9.84E-05	6.79E-02	5.00E-02	7.2	1.0444
H2M-017	267	1	0.013	0.0164	9.94E-05	6.86E-02	4.76E-02	8.3	1.0619
H2M-017	267	2	0.017	0.0217	1.17E-04	8.05E-02	5.72E-02	10.6	1.0530
H2M-017	267	3	0.023	0.0294	1.30E-04	8.98E-02	6.56E-02	12.8	1.0625

ND = no data.

Continued . . .

Table 3-9. Separator Performance Data (continued)

Run No.	CSIRO Separator No.	Steady-State Period	H_2 Flux Flow (leak-free basis), scmh	H_2 Flux (leak-free basis) mol/(m^2*s)	H_2 Permeance (leak-free basis) mol/ (m^2*s Pa$^{0.5}$)	H_2 Flux at 689.5 kPad (DOE 100 psid) (leak-free basis) mol/(m^2*s)	H_2 Flux at 689.5 kPad (DOE 100 psid) Sievert's Law (leak-free basis) mol/(m^2*s)	H_2 Recovery (leak-free basis), %	CO_2 Concentration Factor, wet basis
H2M-017	265	1	0.017	0.0215	9.77E-05	6.74E-02	4.96E-02	7.1	1.0441
H2M-017	266	1	0.013	0.0164	9.94E-05	6.86E-02	4.76E-02	8.3	1.0619
H2M-017	266	2	0.017	0.0217	1.17E-04	8.05E-02	5.72E-02	10.6	1.0530
H2M-017	266	3	0.022	0.0281	1.25E-04	8.62E-02	6.31E-02	12.2	1.0607
Large separator assembly previously tested.				0.0203	3.58E-04	3.58E-02	2.90E-02	11.2	ND

ND = No Data

Figure 3-29 represents the relative hydrogen flux rates of the separators by plotting permeance against the partial differential pressure. Because of the limited operating conditions, the data maintain tight clusters for H2M-016 and H2M-017. H2M-015 had pure hydrogen and syngas feed conditions which caused a wider distribution of the data. Figure 3-30 shows the permeance of the separators at their operating temperatures. CSIRO had specified a matrix of operating conditions for testing during H2M-015. As discussed previously, challenges with failures of the thicker support structure due to thermally induced stresses were encountered. Therefore, CSIRO's objective for H2M-016 and H2M-017 was to simply expose the separators to gasifier syngas at fixed pressure, temperature, and feed flow rates.

It can be noted that as the H_2 permeance increased, so did the CO_2 concentration factor, as shown in Figure 3-31. Placing multiple separators in series, such that the retentate from one feeds the next would further concentrate the CO_2. As the hydrogen is further removed from the syngas stream, CO_2, N_2, CO, and H_2O would be left as the major constituents. Water is easily condensed out of the syngas stream. The CO_2 could be removed using a physical solvent system or PSA system.

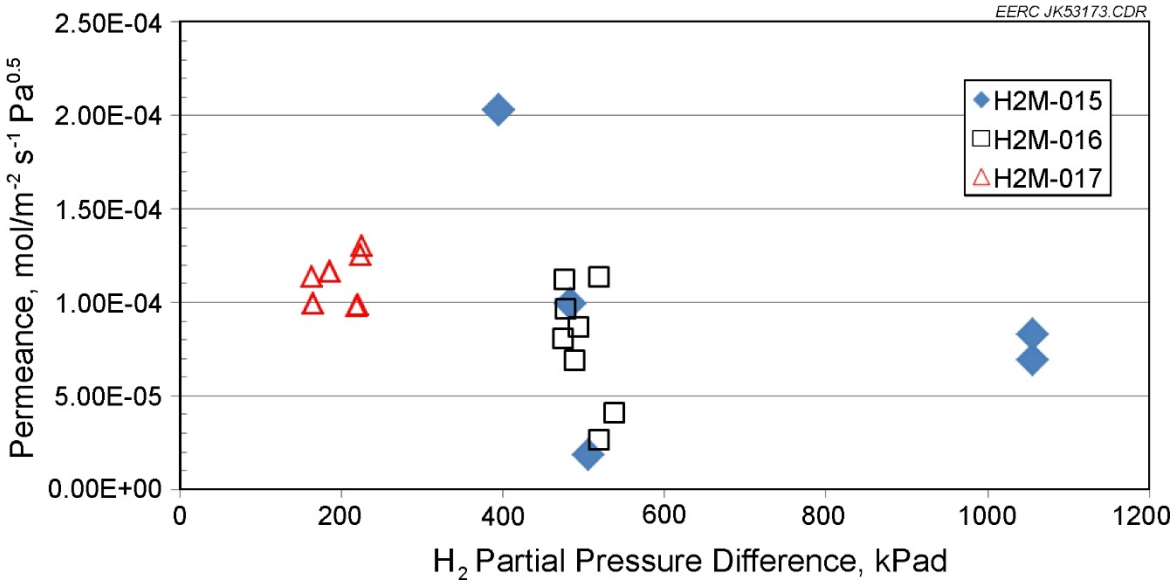

Figure 3-29. Flux plotted as permeance against partial differential pressure.

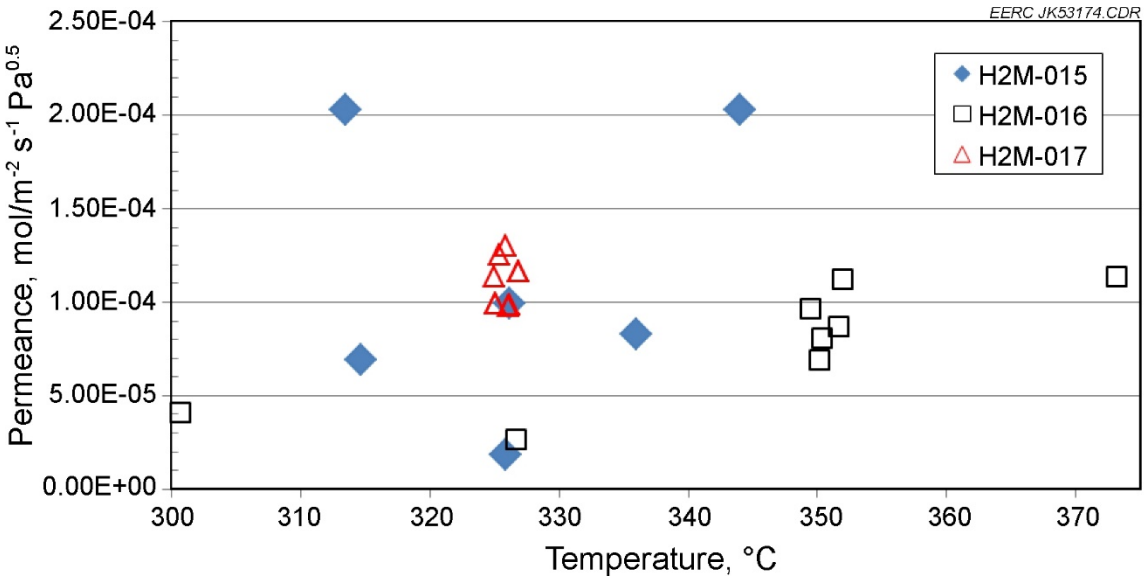

Figure 3-30. Permeance vs. temperature.

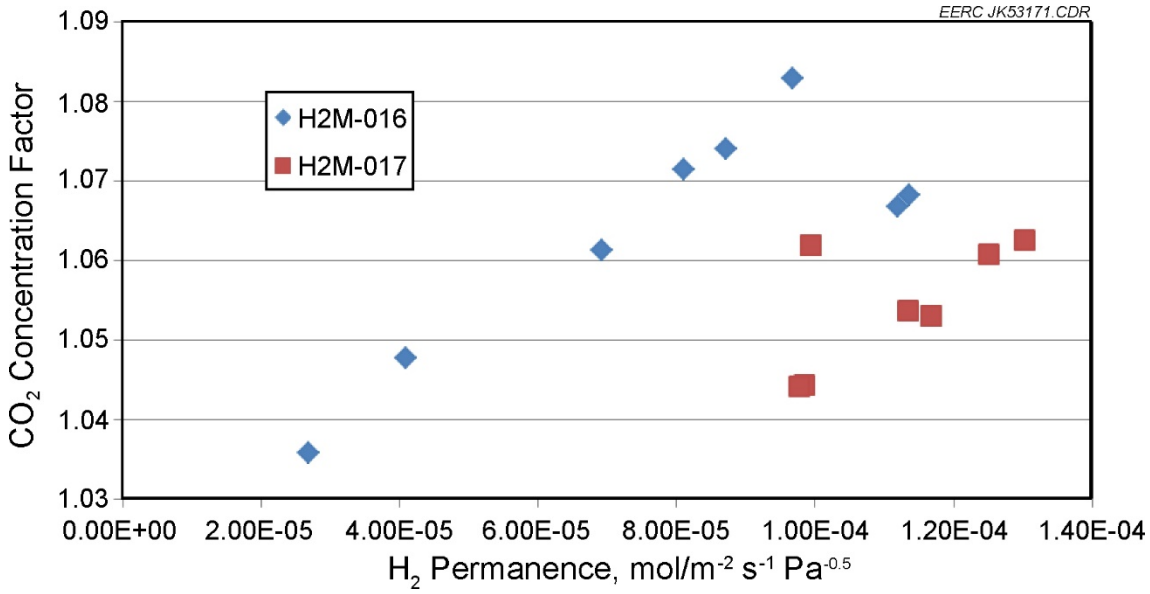

Figure 3-31. CO_2 concentration factor vs. H_2 permeance.

3.4 Conclusions and Recommendations

The EERC carried out a third weeklong campaign (H2M-017) to evaluate hydrogen separation membranes that were made by CSIRO using the HMTS. The syngas was generated by the high-pressure FBG. Gas cleanup consisted of a WGS reactor to increase the hydrogen content of the syngas and H_2S reactors to reduce the H_2S content to <1 ppm. No sweep gas was used on the permeate side of the membrane. This would have enhanced the partial pressure difference, but the use of sweep gas is generally considered a means of adding a contaminant to the hydrogen in the permeate stream.

The separators employed in H2M-017 had a novel design. The support structure was 250-µm porous vanadium, with the actual membrane composed of a 50-µm 100% palladium layer on the vanadium and a subsequent 50-µm 70%–30% Pd–Au layer over the top. The first two weeklong campaigns (H2M-015 and H2M-016) employed 500-µm-thick porous vanadium supports with a 1–2-µm palladium membrane layer.

As expected, the thin vanadium support structure facilitated better hydrogen flow through the membrane at lower transmembrane differential pressures. This makes them good candidates for medium-pressure gasifiers. The hydrogen selectivity of the membranes was very good, with no other components of the syngas detected in the permeate stream.

In general, when CSIRO's separators were first exposed to hydrogen, there was a large temperature spike due to the exothermic absorption of hydrogen into the membrane. Once hydrogen permeates through, the endothermic desorption reaction stabilizes and the membrane will return to the original temperature. If the temperature spike is too large, it can cause unwanted reactions at the Pd–V interface, resulting in performance degradation or fracture failure due to induced thermal expansion stresses. We believe this was the cause of some of the previous fracture failures associated with the thicker separators used in H2M-015 and H2M-016. The thin separators that were tested in H2M-017 appeared to be much more tolerant of the temperature spikes. We believe this is due to the thinner vanadium support structure, which reduced mechanical stresses induced by the temperature spikes.

The transmembrane pressure boundaries of the new thin-wall separator design are also an unknown at this time. Increasing the transmembrane pressure would increase the hydrogen flux, so it is important to know the operational pressure limits. The separator resistance to trace constituents of gasifier-generated syngas is also an unknown. Long-term exposure to syngas needs to be conducted to determine the effects of these trace constituents on the separators. Life cycle testing of the separators still needs to be conducted to determine their robustness in situ.

The 3/8-in. tubular separators used in all three testing campaigns were installed in our HMTS through the use of compression fittings. The ferrules in the compression fitting were made of graphite. In H2M-015 and H2M-016, these graphite ferrules were observed to leak as the separator went through gas and temperature cycling. Gas cycling is when the separators are started with nitrogen purge gas, exposed to hydrogen or syngas containing hydrogen, then again exposed to nitrogen purge gas and so on. We believe the tubular separator is expanding and contracting through these swings in gas composition and operating temperature, while the compression

fitting's ferrule is not flexible enough to expand and contract with the separator. Therefore, a notable challenge exists in determining how to bond the separator tube to a conventional SS tube. This could potentially be done with orbital laser welding or diffusion bonding. The metallurgy at the joint will also require significant investigation to determine its resistance to syngas constituents as well as expand and contract in concert with the separator throughout its life.

As the CSIRO separator technology is validated, scaling up to larger separator tube bundles will be required. Past testing of large hydrogen membrane separation assemblies has indicated that the internal aerodynamics of the retentate side are of concern. The issue is to ensure that the syngas is adequately turbulent to distribute the hydrogen within the tube bundle and to provide for relatively uniform temperature distribution.

4.0 ACTIVITY 4 – EVALUATION OF NEXT-GENERATION POWER CYCLES WITH CARBON CAPTURE

4.1 Overview of Next-Generation Power Cycles

Many versions of next-generation power cycles are being developed that promise high efficiency, better environmental performance, and increased opportunity for economical carbon capture. Many have seen significant development work; others are still under laboratory-scale development. All have key challenges that would need to be overcome to progress to demonstration and commercial scale. Many offer the promise of a continued future for the use of coal even in light of potential regulations for CO_2 emissions. The Electric Power Research Institute (EPRI) recently published a summary report on advanced power cycles that have the potential to meet the targets (34). A number of these cycles also need major advancements in the cycle technology before they are considered commercially viable.

Some of the most notable advanced cycle technologies include the following:

- Supercritical CO_2 cycles
- IGCC
- Integrated gasification solid oxide fuel cell (SOFC)
- Ultrasupercritical (USC) boilers
- Oxygen-fired combustion
- Chemical-looping combustion or gasification

4.1.1 Supercritical CO_2 Cycles

Utilization of supercritical CO_2 to drive a turbine and generate power has the potential to significantly increase cycle efficiency over traditional steam cycles. Indirect-fired Brayton cycles operate similar to a traditional combustion system, and can utilize any source of energy available to heat the CO_2. Directly fired cycles offer the potential to generate power at very high efficiencies while producing a CO_2 stream that is ready for sequestration. One such cycle that is currently in an advanced stage of development is the Allam Cycle, which can be operated using coal or natural gas.

The Allam Cycle is a high-pressure, highly recuperative, oxygen-fired, supercritical CO_2 cycle that makes carbon purification part of the core power generation process (35). This cycle utilizes supercritical carbon dioxide as a very high pressure working fluid through a very compact high-pressure turbine. In a coal-fired Allam Cycle, coal is gasified in an appropriately selected commercial oxygen-blown gasifier to generate syngas. This syngas is compressed to the operating pressure of the syngas combustor/turbine (typically 4350 psia) before being combusted with an oxygen–carbon dioxide mixture to achieve turbine inlet temperatures around 1150°C. Exhaust heat from the system is recycled back to the turbine to produce a highly efficient cycle. The products from the process are electricity and a stream of relatively pure CO_2 ready for sequestration or utilization.

The major new components that need to be demonstrated are the high-pressure syngas combustor and the supercritical CO_2 turbine expander. These are currently undergoing testing and development by Toshiba for a 25-MWe natural gas-fired demonstration system in Texas. Toshiba currently makes USC steam turbines that operate in this pressure range and also manufactures gas turbines that operate at temperatures even higher than the supercritical CO_2 turbine inlet temperature. Thus the technology is derived from combining steam and gas turbine technologies together into one machine without the need for new specialized materials of construction. A second concern is the potential for corrosion (especially aqueous corrosion) of various materials in the supercritical CO_2 cycle.

Cycle efficiencies are projected to be greater than 47% on a HHV basis for a lignite feedstock while producing a near-sequestration-ready CO_2 stream requiring some O_2 reduction and dehydration (35). Higher-ranked coals are projected to achieve over 50% cycle efficiency. According to the recent EPRI report, the coal gasification/supercritical CO_2 cycle can offer a 25% increase in net cycle efficiency when compared to an IGCC with 90% CCS (34).

4.1.2 Integrated Gasification Combined Cycle

IGCC is a readily available technology for coal feedstocks. Certain gasifier technologies are more suited to utilize high-reactivity feedstocks, such as lignite, and other high-temperature gasifiers are well-suited for bituminous coal. Only the most efficient IGCC with a high-quality bituminous coal would be able to meet the U.S. Environmental Protection Agency's (EPA's) Clean Power Plan (CPP) standards without the need for CCS (34). Any lignite-fueled IGCC plant would need to incorporate a significant amount of carbon capture into its project; however, it is inherently more efficient to capture CO_2 from an IGCC system versus a conventional boiler. The overall IGCC thermal efficiency would still drop from approximately 38% to approximately 30% by incorporating 90% CO_2 capture (35). Development of gas turbines capable of operating at turbine inlet temperatures approaching 1700°C instead of the current nominal 1400°C firing would lead to a 16% increase in thermal efficiency, resulting in a lignite-fueled IGCC achieving EPA CO_2 emissions standards without CCS (34). The fact that fighter jet engine manufacturers have built jet engines operating with 1982°C turbine inlets suggests that this may be feasible in the future, but it is projected to be at least 10 years before this would be commercially available for an IGCC application (35).

4.1.3 Integrated Gasification Solid Oxide Fuel Cell

The cycle projected to have the lowest heat rates and CO_2 emissions includes an integrated gasification system in which the syngas is fed to a SOFC. Syngas and air react on the anode and cathode sides of the cell to produce heat, direct current, and some residual unreacted syngas, which is combusted to produce heat for steam and additional power. The SOFC can be operated at atmospheric pressure or at elevated pressures for increased efficiency. Projected thermal efficiencies range from approximately 44% to 52% depending on the pressure of the SOFC (34). The cycle with the highest calculated efficiency is pressurized SOFC with its residual syngas burner feeding a 1500°C class gas turbine and a HRSG (heat recovery steam generator) steam turbine third cycle. The IGFC (integrated gasification fuel cell)/integrated gasification triple cell cycles probably have the lowest technical readiness because the SOFCs are still in early development, with very limited size and operating experience to date.

4.1.4 Ultrasupercritical Combustion

Current state-of-the-art USC boilers are operating with steam temperatures and pressures around 650°C and 4000 psi. Current materials research with some nickel alloys suggests that steam temperatures and pressures up to 760°C and 5100 psi may be possible (34). For lignite-fired systems, EPA's CPP emission limits could not be achieved without at least 20% CO_2 capture. The use of current amine-based processes for CO_2 capture in low-pressure flue gases is projected to increase parasitic loads by up to 30% and nearly double COE in these types of plants (34). Therefore, high-rank coals would be at a significant advantage if carbon capture regulations were implemented. The necessary inlet steam temperature required to eliminate the need for CCS for lignite is an unrealistic 1125°C; therefore, lignite systems may be required to operate under combined heat and power applications. Approximately 17% or more of the steam would need to be extracted from between the intermediate- and low-pressure stages of the steam turbine to achieve this.

4.1.5 Oxygen-Fired Combustion

In order to avoid having to utilize postcombustion amine-based scrubbers for CO_2 capture, some demonstrations of oxygen firing in both supercritical pc (pulverized coal) boilers and CFB (circulating fluidized-bed) boilers have been conducted. The use of oxygen requires that a significant amount (55% to 70%) of the CO_2-rich flue gas be recirculated to the boiler to keep the operating temperatures within the limits for the boiler tube materials. For a supercritical pc boiler, thermal efficiencies have been calculated at around 32% (a reduction of approximately 7.5%) primarily because of the addition of the air separation unit (ASU), CO_2 cleanup, and CO_2 compression and liquefaction equipment parasitic loads (36).

An oxygen-fired, subcritical CFB boiler has also been successfully tested by Alstom Power and shown to require significantly less flue gas recirculation than pc units because of the additional heat dissipation from the circulating solids. This study has shown that the thermal efficiency would drop from approximately 35.5% for an air-blown system without CCS to approximately 26% with oxygen firing and CCS (37). The plant output was reduced by 28%, with the COE increasing by 75% from $45/MWh to $79/MWh. The technology for these types of systems is considered to be

near commercially available since only the integration of a commercially available ASU and a gas-processing system is required.

4.1.6 Chemical-Looping Combustion or Gasification

Chemical-looping technology was originally proposed as a way to oxidize carbonaceous feedstocks without utilizing either air or oxygen directly in the process. This avoids the dilution of the flue or fuel gas with the nitrogen that would enter with the air or avoids the capital and operating costs without the parasitic loads of an ASU. This is accomplished by utilizing a solid oxygen carrier to shuttle oxygen to the feedstock. For coal, these chemical-looping compounds have generally consisted of either iron-, calcium-, nickel-, or copper-based materials being utilized in two interconnected CFB reactor systems (38). In these systems, the solid fuel does not react with the oxygen-rich looping agent directly but is instead gasified with a gasification agent such as steam or CO_2 to produce reduced gas species such as hydrogen, CO, methane, and light hydrocarbons. These species then react with the oxygen present in the looping agent to release primarily heat, carbon dioxide, and water vapor. The hot, oxygen-depleted looping agent is then recirculated back into a second fluid bed where it is reoxidized with air to complete the loop.

A second option is to directly gasify the solid fuel and then send the syngas only to the chemical-looping combustor, although this option does not eliminate the need for an ASU. This technology is still very early in its development, with significant issues to be resolved about the activity and longevity of the chemical-looping agents, along with issues associated with the complexity of operating a twin fluid-bed system. Thermal efficiencies with inherent carbon capture are projected to approach 42% for the in situ gasification process and as high as 44% for the separate gasification and syngas fuels-looping process (38, 39). Chemical looping looks to have superior cycle performance when compared to oxygen-fired combustion systems and IGCC systems with CCS but is considered to be much farther away from technical readiness than these technologies.

4.1.7 Pressurized Oxygen-Fired Combustion

One area of interest that has seen little technology development to date is pressurized oxygen-fired combustion. This technology holds the potential to generate power while producing a highly concentrated, pressurized flue gas stream that is nearly pure CO_2 and sequestration ready. The conditions of the flue gas are such that simple water-scrubbing techniques may be used to oxidize impurities such as SO_x and NO_x and remove from the system. The potential benefits of this technology warrant further investigation.

As a result of the next-generation power cycle technology review, the EERC focused its subsequent efforts on generating additional data and information for pressurized oxy-combustion systems and supercritical CO_2 cycles. These technologies hold promise in realizing highly efficient systems with simplified carbon purification techniques.

4.2 Pressurized Oxy-Combustion

As part of this activity, the EERC evaluated pressurized oxy-combustion technology from the standpoint of CO_2 purification. This type of technology inherently produces a CO_2-rich flue gas, and if techniques can be develop to remove the impurities, the cost of CO_2 capture can be lowered significantly over postcombustion capture systems. An overview of the technology concept is shown in Figure 4-1. In a pressurized system, particulates are easily removed to near-zero levels by commercially available candle filtration technology. The gas is then cooled and sent to a water–gas contactor where the available pressure and reaction chemistry allow for the conversion of sulfur species to sulfuric acid, nitrogen species to nitric acid, and any chorine to hydrochloric acid. Some level of trace metal control can also be achieved in this system. Excess oxygen and remaining moisture can be removed in subsequent process steps. For the purposes of this subactivity, the EERC focused on developing the reactions and chemistry necessary to remove the sulfur and nitrogen species from the flue gas.

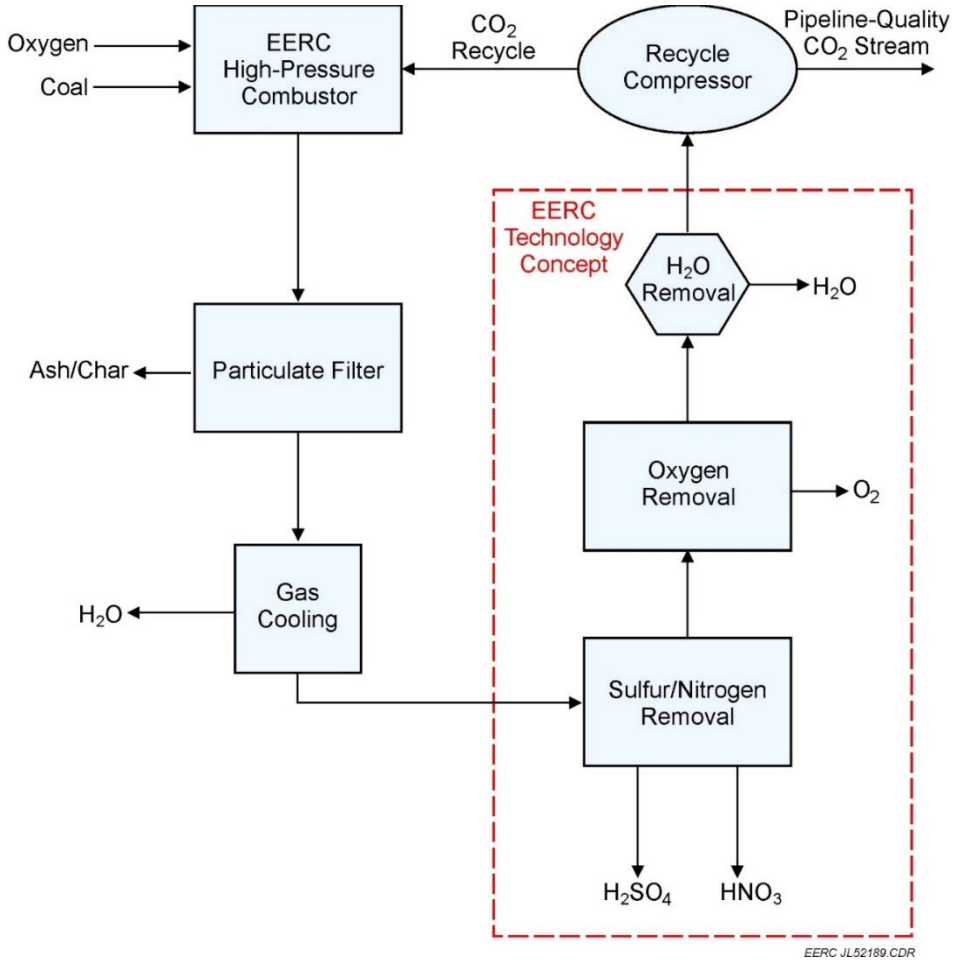

Figure 4-1. Proposed technology approach.

In order to accomplish these goals and increase the understanding of CO_2 impurity removal techniques in next-generation power cycles, the EERC utilized existing equipment to generate flue gas in a pressurized oxygen-fired environment and then tested nitrogen and sulfur species removal. The process uses a simple water scrubber to accomplish the removal in one step and is dependent on oxidation of the contaminant species to sulfuric and nitric acid. The technology, referred to by the team as the $DeSNO_x$ process, has the potential to remove contaminant species in pressurized oxy-fired systems and in direct-fired supercritical CO_2 cycles at low cost.

Two of the EERC's pilot gasifiers and a skid-mounted acid gas absorption system, all capable of operating at a high pressure (450 psig and 300 psig), were selected for the experimental validation of pressurized oxy-combustion and the $DeSNO_x$ process. These systems were integrated into multiple configurations to attain test objectives. The selected pilot systems were originally designed with the goal of testing a wide range coal-to-syngas and liquid fuel conversion processes. Considering the objectives, these subsystems were modified to generate flue gas. The system descriptions of the equipment used and modified for this activity are shown below, followed by a description of design modifications undertaken to test in this environment.

4.2.1 High-Pressure Fluidized-Bed Gasifier

The high-pressure FBG system at the EERC has been designed according to ASME B31.3 Process Piping Code specifications. The internal reactor dimensions are based upon the existing operational continuous fluid-bed reactor (CFBR) that currently operates up to a MOP of 1.0 MPa (150 psig). After a review of available alloys, Haynes 556® was selected as the material most suitable for fabrication of this high-temperature, high-pressure system. The reactor was designed with the capability to operate at a MOP of 6.9 MPa (1000 psig) at an operational temperature of 843°C (1550°F), 4.5 MPa (650 psig) at an operational temperature of 917°C (1650°F), and 2.0 MPa (300 psig) at an operational temperature of 1800°F. This system was designed to be externally electrically heated in a similar manner to the CFBR. The 2500-lb 316H SS flanged connections at the top and bottom of the reactor are limited to a maximum operating temperature of 677°C (1250°F) for a MOP of 6.9 MPa (1000 psig), 732°C (1350°F) for a MOP of 4.5 MPa (650 psig), and 816°C (1500°F) for a MOP of 2.0 MPa (300 psig). A concept drawing of the FBG reactor, feed system, and syngas quench system is shown in Figure 4-2.

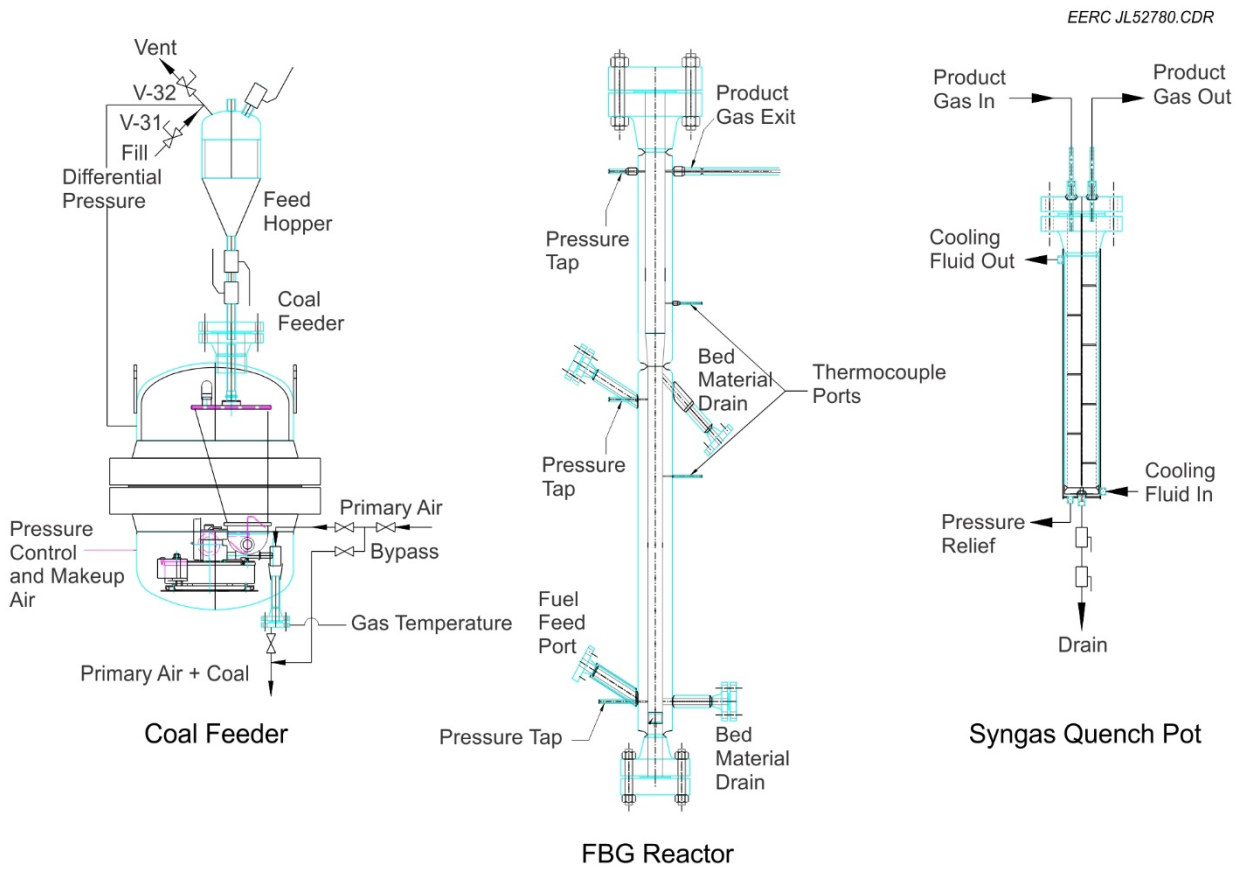

Figure 4-2. Cross-sectional view of the FBG, gasifier feed system, and syngas quench system.

4.2.2 Entrained-Flow Gasifier

The EFG is a dry feed, downfired system. Figure 4-3 shows cross-sectional and photographic views of the EFG. The reactor tube is vertically housed in a pressure vessel of approximately 24 in. i.d. and 7 ft in length. The EFG fires nominally 8–12 lb/hr of fuel and produces up to 20 scfm of fuel gas. The maximum working pressure is 300 psig. The reactor has the capability to operate in an oxygen- or air-blown mode. A supplemental electrical heating system is capable of attaining a nominal temperature of 1565°C (2850°F) and is separated into four independent zones so that a consistent temperature can be maintained throughout the length of the furnace. The radially spaced heating elements preheat the centrally located alumina reactor tube, and refractory walls outside the heating elements provide insulation. Type S thermocouples are used to monitor and control the temperatures of the heating zones and reactor tube. All of the gasification reactions occur inside of the reactor tube, and slag can flow on the tube wall. The pressure inside the alumina reactor tube is balanced with a slight positive nitrogen pressure outside of the alumina reactor tube.

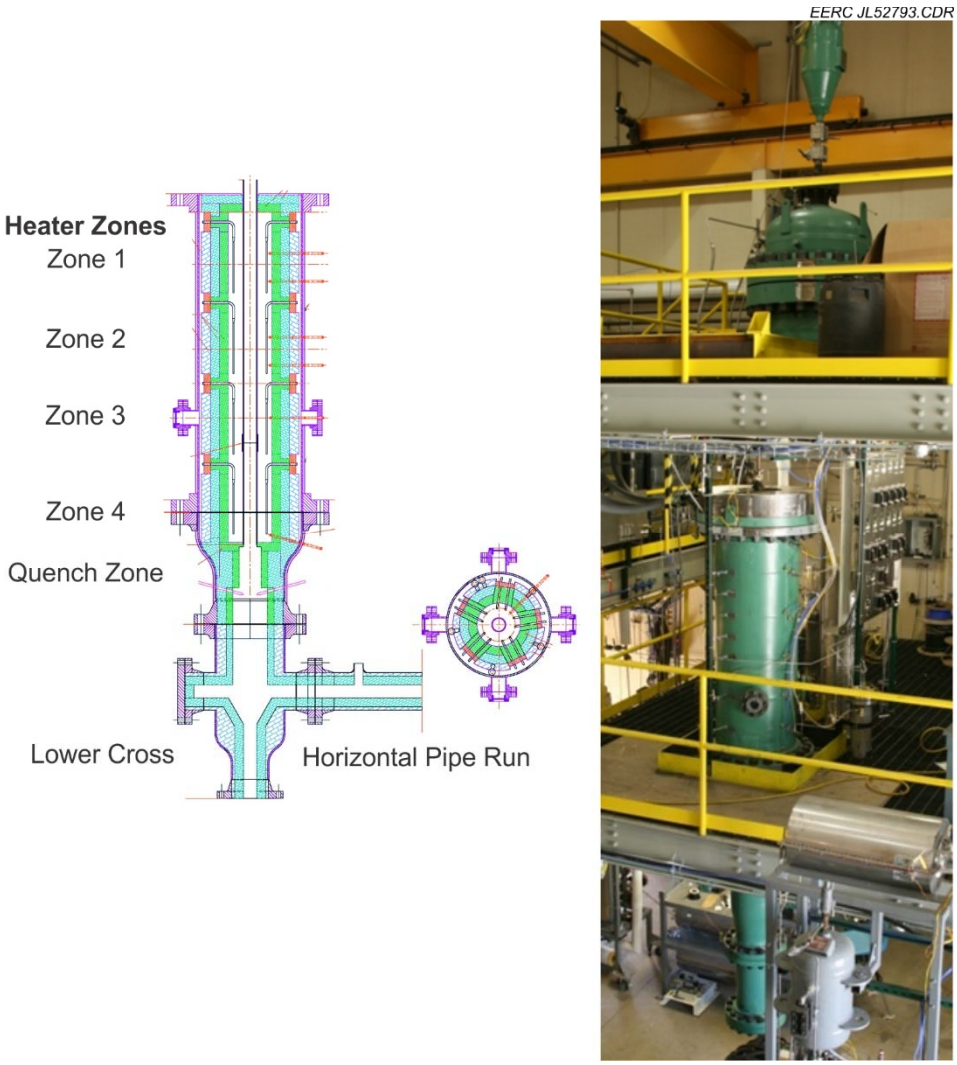

Figure 4-3. Schematic and photograph of the bench-scale EFG.

Product gas exits at the bottom of the furnace tube and enters a gas quench zone capable of injecting any liquid, gas, or mix thereof as the quench fluid. Syngas makes a 90° turn as it flows through a cross-pipe section and then exits the main unit on its way to the back-end subsystems. Denser slag, ash, and char that lose entrainment from the syngas stream will drop down through the cross and accumulate in a refractory-lined slag trap. The system must be depressurized and cooled a bit for slag trap samples to be collected. Design provisions for the installation of valving allow for periodic sampling without depressurizing and cooling the system.

The EFG shares the feeder and all back-end systems with the FBG. A significant cost saving is passed along to clients through the use of the shared equipment. The EFG may be connected in tandem with the FBG for a two-stage approach to torrefaction, pyrolysis, and gasification.

4.2.3 Particulate Filter System

The particulate matter in the syngas produced in gasifiers (FBG and EFG) is cleaned in a filter system consisting of hot-gas candle filters designed to operate at high temperatures and high pressures. The vessel can handle a gas flow up to 30 scfm at 843°C (1550°F) and 1000 psig. The filters are sealed in the tube sheet by a bolted metal plate and fiber gaskets which counteract the upward force imparted across the candle filter by the filter's differential pressure. The vessel is sized such that it can handle three candle filters up to 18 in. long with a 2.375-in. diameter and enables gas face velocities as low as 2.5 ft/minute during the test. Higher-face-velocity gas would be achieved by using shorter candles or higher gas flow rates. Ports are added in the filter vessel for allowing temperature and pressure measurements to be obtained. The ash letdown station consists of two high-temperature valves to act as lock hoppers to isolate the ash hopper from the filter vessel.

The filter vessel's backpulse system may be operated with either nitrogen or recycle syngas. The backpulse system is designed to supply a minimum of three candle volumes per pulse for the longest candle filters and even higher volumes for the shorter candle filters. The length and volume of nitrogen displaced into the vessel are controlled by the regulated pressure of the cold-gas reservoir and the solenoid valves used to control the timing of the cold-gas pulse. Optionally, a heated backpulse gas could be utilized. An electrically heated ½-in. pipe is used to connect the gasifier to the filter system.

4.2.4 Syngas Quench System

Two sets of three (six total) water-cooled quench pots condense moisture and organics from the gas stream. These quench pots were designed for operation up to 1000 psig. The design of these quench pots was based on what was successfully used with the CFBR. This design is very efficient in the removal of organics and moisture while not plugging off. It has evolved over years of operation. Either water or a chilled glycol–water mixture is circulated through the outer jacket of each quench pot to cool the product gas.

4.2.5 Product Gas Measurement and Analysis

For both the FBG and EFG, pressure, temperature, fuel feed rate, steam flow, and other gas flows are independent variables. Syngas production is one of the dependent variables. The sensed pressure originates at the gasifier with the control signal to the back-pressure control valves (BPCVs) processed by the gasifier control program. Product syngas is routed through a set of flow control valves, which operate as BPCVs. The volumetric flow of product syngas is measured by both a high-pressure Coriolis meter and a low-pressure dry gas meter. Temperature, pressure, and molecular weight corrections are made in real time by the gasifier control program.

A slipstream of dry gas may be fed to LGA and GC analyzers for online analysis of the main gas components and low-level (ppb) analysis of sulfur species. The EERC has up to five Atmosphere Recovery, Inc., LGAs available for use with the gasifiers. The LGAs employ Raman detectors to stimulate sample gas and emit distinct light spectra. Two LGAs are dedicated to the gasifiers and have the designations LGA35 and LGA39. The LGAs are each capable of measuring

the real-time concentrations of eight gases at once. Seven of those gases are H_2, CO, CO_2, N_2, H_2S, CH_4, and total hydrocarbons. LGA39 is capable of measuring O_2 in addition to the suite of gases above and is usually dedicated to gasifier control and operation. In comparison, LGA35 is capable of measuring H_2O instead of O_2. It is used to measure the gas compositions from various sample ports. LGAs 49, 105, and 106 are configured similarly to LGA35 but are not strictly dedicated to gasifier operations.

A Varian GC is equipped with two TC detectors for bulk and trace gas measurement and a pulsed-flame photometric detector for ultralow sulfur detection. The first TC detector is dedicated solely to analyzing H_2 and provides three H_2 measurements for each 15-minute analysis cycle. The second detector is configured to analyze the gas stream for CO, CO_2, N_2, O_2, H_2S, COS, CH_4, C_3H_6, C_3H_8, C_2H_4, and C_2H_6. A measurement is provided every 15 minutes for each of the gases. The third detector can detect ultralow H_2S levels, down to 0.02–1 ppm. Figure 4-4 shows the gas-sweetening absorption system (GSAS) process flow diagram and system photo.

A Yokogawa GC is paired with LGA39 to provide redundancy and for analyzing hydrocarbon and other trace syngas species. The Yokogawa GC is capable of measuring CO, CO_2, N_2, O_2, H_2S, COS, CH_4, ethane, ethylene, propane, and propene. The Yokogawa has high H_2S measurement capabilities and is better-suited to syngas that has not had the H_2S removed. LGA35 is typically paired with the Varian 450 GC.

The analyzers are calibrated before the start of and after each test program. Sample gas streams are manually switched via selector valves. Since LGA35 and the Varian are typically paired and are used in conjunction with the back-end processing systems, periodic samples may be taken from various points in the system. The time duration for sampling from a port is 1 hr. This period is adequate in allowing the Varian to complete sufficient cycles to flush previous sample gas and acquires measurements with a high degree of confidence in their accuracy. Sample gas tubing from sample ports to the analyzers is PE, with no line longer than 50 ft. Sample gas transit times to the analyzers are estimated to be less than 1 minute, depending on the individual sample gas flow rate. Gas is cooled and quenched before transport to the analyzers, so measurements are on a dry basis.

In addition to analyzer sampling from various points throughout the system, Dräger tubes may be used. H_2S, HCl, HCN, NH_3, and other trace gases can be checked to verify low-level chromatograph data. Dräger tube and gas bag samples may also be drawn from several ports on the gasifier system.

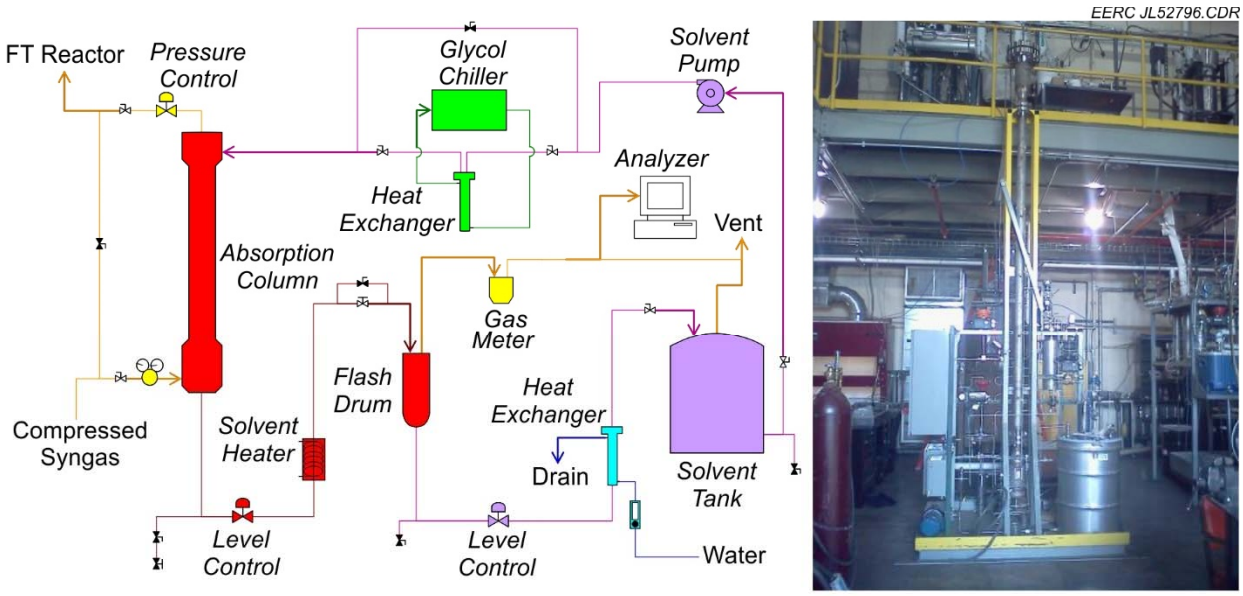

Figure 4-4. GSAS process flow diagram and system photo.

4.2.6 Acid Gas Absorption System (AGAS)

The EERC has designed, built, and tested a skid-mounted CO_2 and H_2S AGAS. The AGAS uses physical solvents such as Rectisol and SELEXOL to remove CO_2 and various contaminants from dry syngas at pressures of up to 1000 psig. In this project, the AGAS was used as contactor for the DeSNO$_x$ tests. The AGAS allows the EERC to produce syngas that more closely resembles that generated in full-scale commercial gasification and it also allows the EERC to test solvents and technologies for natural gas sweetening and liquids capture. The ability to remove CO_2 from gas streams allows the EERC to test processes incorporating CCS.

Up to 1000 scfh of pressure-regulated gas is injected from the lower section of the absorption column. The syngas or gas produced in the gasifiers can be directly fed after passing through the quench system. As an alternative, the syngas can be precompressed prior to feeding into the Fischer–Tropsch (FT) system. The solvent is injected from the top of the column, and mass exchange occurs in the column packed bed as the sweet gas passes through a demister to remove entrained solvent droplets. The sour gas-rich solvent collects in the bottom disengager, where gas bubbles have sufficient residence time to escape from the liquid. The solvent then flows through a control valve, a heat exchanger, and a flow constrictor before passing into a flash drum. The flow constrictor maintains some pressure upstream of the flash drum, preventing excessive cavitation in the control valve and heat exchanger.

As solvent warms and depressurizes inside the heated flash drum, CO_2 and other gases vaporize from the solvent. A flowmeter records the rate of acid gas exiting the flash drum, while a continuous gas analyzer records the gas composition. These measurements permit online mass and carbon balance calculations.

Lean solvent exits the flash drum through a level-controlling valve and then passes through a water-cooled heat exchanger on its way to a storage tank. A pump pulls solvent from the bottom of this tank and sends it through a glycol-cooled heat exchanger. The chilled lean solvent then sprays through a nozzle into the top of the absorption column, completing the solvent loop.

4.3 System Modifications

The test objectives required production of a CO_2-rich flue gas stream containing impurities expected in the coal-to-power conversion cycle. The high-pressure FBG pilot system was modified to operated under direct oxy-coal combustion mode as a single-stage approach to flue gas production. Under the last test campaign, the FBG was operated as a gasifier while the syngas produced in the FBG was combusted in the EFG. The system modification also included addition of CO_2 purges instead of N_2 purges to simulate the low-nitrogen-containing pressurized oxy-combustion operating conditions.

The primary focus of the testing was to determine the operability of a pressurized oxy-combustion system and the viability of the DeSNO$_x$ process. During both modes of operation (single- and two-stage), a slipstream of particle-free flue gas was routed to the modified acid gas scrubber (DeSNO$_x$ column) system. The DeSNO$_x$ column was modified to operate in a water-based open-loop process instead of its standard solvent-based closed-loop operational mode. The process evolved during the project, and the operation was fine-tuned so that the freshwater injection and acidic water removal were at a constant rate. Thus the scrubber water pH of the DeSNO$_x$ process was maintained at nearly a constant value.

Scrubbed gas flow control and measurement were attained by integrating the DeSNO$_x$ column to the back-end gas-handling systems of an existing FT system. The sweetened CO_2-rich flue gas was vented downstream of this system. In addition, the gas pressure booster pump integrated with the FT system was used to provide high-pressure purge and recycle gas, which helped to prevent N_2 dilution in the process gas stream.

The gas-sampling systems for measuring trace and bulk gas composition were modified. A high-level P&ID of the single and two-stage processes incorporating the system modification is represented in Figures 4-5 and 4-6.

4.4 Reconfigured System Operational Features

4.4.1 Single-Stage Operational Mode

The FBG converted to operate in a direct oxy-coal combustion mode is shown in Figure 4-5. The existing HGFV was used for particulate control. The HGFV employs a ceramic candle filter as described earlier. The backpulsing gas injection utilized recycled flue gas. The particle-free flue gas stream was bifurcated into the DeSNO$_x$ column feed and recycle/exhaust lines. The heat-traced piping was installed for transferring a slipstream of the temperature-regulated flue gas to the DeSNO$_x$ column. Flue gas recycle was achieved through the use of the syngas compressor. The recycle/exhaust flue gas stream was cooled in a quench train before transport to the recycle compressor, while a slipstream was vented through a dry gas meter.

The $DeSNO_x$ column was reconfigured for operation as a packed-bed column with water recirculation. The packing material used was 316 SS Koch–Glitsch IMTP 15. The EERC's liquid fuels system was used for downstream liquid condensing, gas flow control, and gas flow measurement. The $DeSNO_x$ column was constructed from 304 SS, while the back end of the FT condensation train was constructed entirely out of 316 SS.

As shown in Figure 4-5, seven gas sample ports (designated as Ports A–G) were incorporated into the system to facilitate a high degree of flexibility in extractive gas and water sampling. Owing to the high operating pressures, the original system included safety reliefs and system vents at appropriate locations. The addition of the sampling port required pressure and temperature regulation for specific interface with the sensitive analytical instrumentation. An internal safety review was conducted as part of the system design process.

LGAs, CEMs, and a Fourier transform infrared (FTIR) spectrometer were used to analyze gases in and out of the $DeSNO_x$ column. The LGAs were utilized for measuring flue gas composition of the primary species (bulk gas measurement). The combustion CEM was capable of measuring NO_x, SO_x, and CO_2 gases, but special care was taken to deal with the challenge faced with the condensing gas-conditioning system. The FTIR was operated with an internal temperature of 190°C, thereby avoiding gas cooling and condensing system challenges. The use of FTIR was found to be valuable because of its ability to measure multicomponent trace gas composition with precision.

LGAs were planned to be used extensively for bulk gas determinations. The LGAs require a relatively dry gas to avoid water condensation problems because they utilize Peltier coolers at the detectors. The EERC has up to six LGAs available for use. Four LGAs were used for these tests, designated LGA35, LGA39, LGA105, and LGA106. The LGAs are each capable of measuring the real-time concentrations of eight gases at once. Seven of those gases are H_2, CO, CO_2, N_2, H_2S, CH_4, and total hydrocarbons. LGA39 and LGA035 both measure H_2S, with LGA039 measuring O_2 and LGA035 measuring H_2O. LGA105 and LGA106 are also capable of measuring O_2 and H_2O.

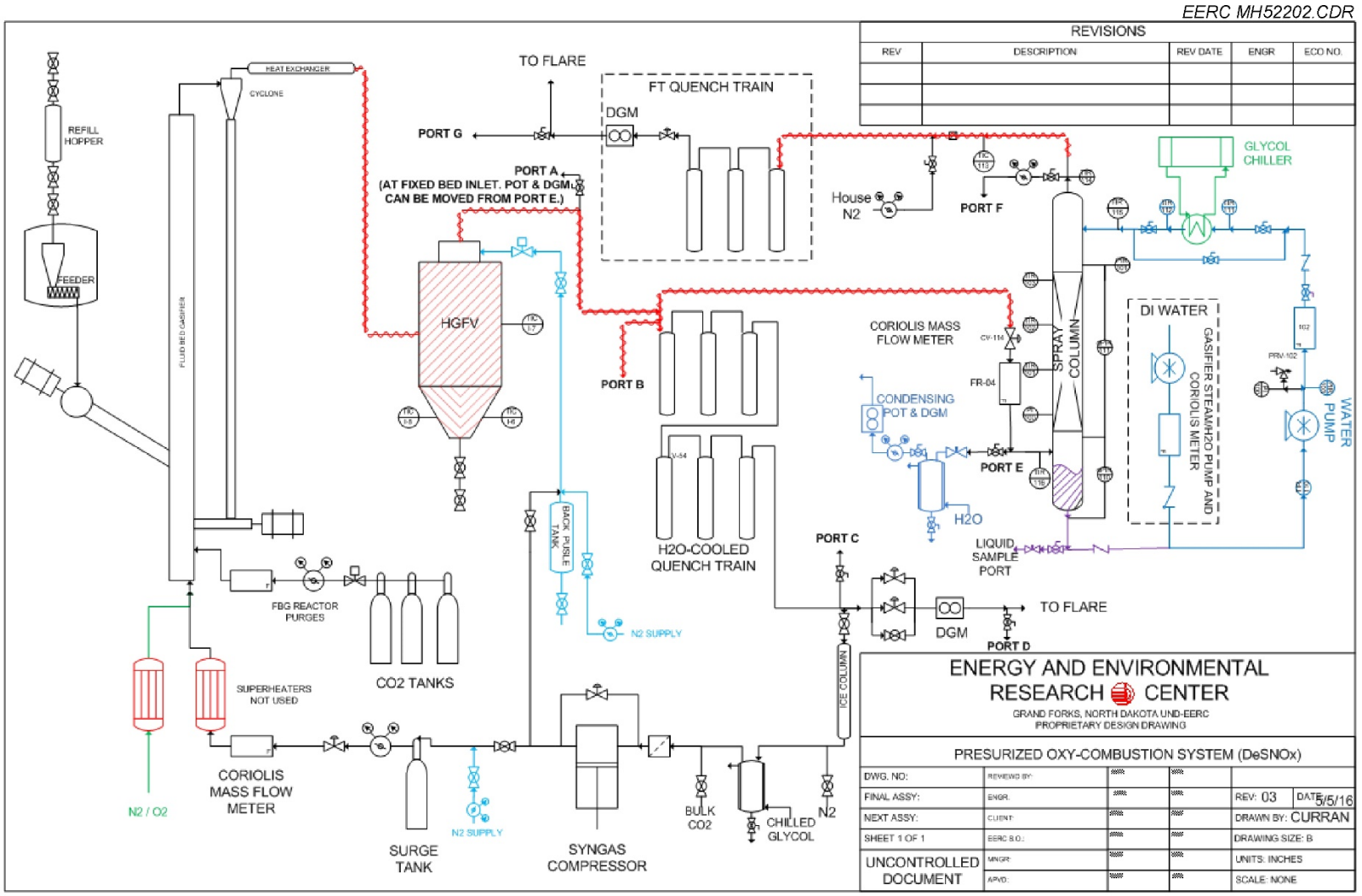

Figure 4-5. High-level P&ID of single-stage test system designed to test DeSNO$_x$ process.

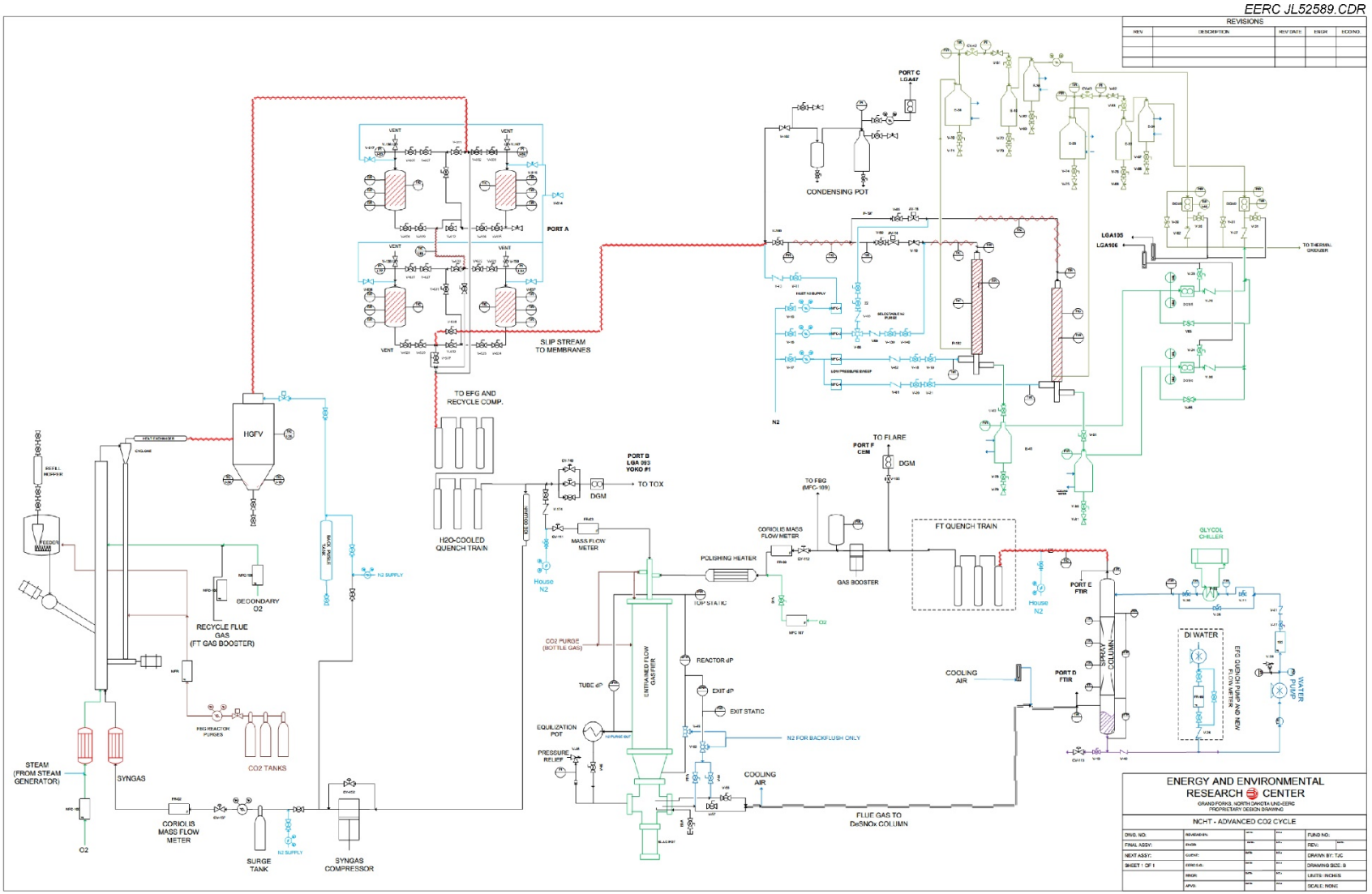

Figure 4-6. High-level P&ID of two-stage test system designed to test DeSNO$_x$ process.

4.4.2 Two-Stage Operational Mode

As shown in the P&ID in Figure 4-6, the distinct changes for the two-stage configuration and operation are as follows:

- FBG operation was in oxy-coal gasification mode.
- Compressed syngas is used as recycle gas to the FBG instead of the flue gas as recycle gas in single-stage operation.
- The EFG is converted into a down-fired oxy-syngas combustor or flue gas generator, with the use of recycle flue gas from the $DeSNO_x$ as diluent for controlling EFG flame temperature.
- Overfire oxygen is added as a bed agglomeration mitigation strategy, with the use of recycle flue gas as dilution gas with the freeboard O_2 in the FBG.
- CO_2 is used for purging instead of N_2 to minimize the amount of N_2 in the system.

Flue gas exiting the EFG went directly to the acid gas removal skid, which was operated as a recirculating water spray column. The FT skid was used to cool, measure, and control the flow of the slipstream gas. The gas leaving the FT skid was primarily CO_2, with 1%–2% O_2. This gas stream was pressurized with a set of gas boosters to provide recycle gas for the EFG inlet and FBG freeboard.

During steady-state operation, the use of nitrogen was allowed only as an operational correction strategy such as blowing out the pressure tap or other plugs. As in single-stage operation, recycled syngas was configured for use as backpulse gas in the filter vessel.

The quench train was operated in a normal manner to cool the syngas gas before sending it to the recycle compressor or venting it through the dry gas meter, as described in single-stage operation.

4.5 Test Plan

Three weeks of testing was conducted, and test plans were developed in concert with project partners. The test dates and their respective goals are presented in Table 4-1.

Table 4-1. Test Dates and Goals

Test Week	Test ID	Test Dates	Test Goal
1	FBG-042	April 18–22, 2016	Commissioning test of modified high-pressure coal combuster and $DeSNO_x$ spray column
2	FBG-043	May 9–13, 2016	Single-stage $DeSNO_x$ process performance evaluation
3	FBG-044	July 25–29, 2016	Two-stage $DeSNO_x$ process performance evaluation with H_2–membrane evaluation

4.5.1 Test Fuels and Preparation

North Dakota lignite coal from the Falkirk and Freedom Mines was used during the 3 weeks of testing. Proximate and ultimate analysis and ash/inorganic analysis of the feed coals are provided in Tables 4-2 and Table 4-3. The coal was sized to −10 mesh in the EERC's fuel preparation facility. To ensure accurately metered and nondisruptive flow in the FBG system, the coal was floor-dried before loading in the coal hopper. A targeted moisture concentration within 20%–22% was maintained during operation.

Falkirk coal was tested during the first week of shakedown testing. The Falkirk coal proved to be especially problematic because of its higher sodium content. During the initial testing, agglomeration-related FBG operational challenges were encountered, resulting in a system shutdown that occurred during shakedown testing; therefore, the use of the Falkirk coal was discontinued. The low-sodium Freedom Mine coal was used with no agglomeration issues encountered.

Limestone was used as a sulfur absorption additive at pressurized fluidized-bed conditions. During the planning phase for the first two tests, it was believed that sulfur production would be higher than desired, causing excessive sulfur loading in the spray column. The first single-stage test utilized limestone in the bed until the agglomeration occurred. Limestone was discontinued after that point for the rest of the test. The second single-stage test (FBG-043) utilized a limestone blend. The blending was discontinued after the second-week test since higher-than-expected sulfur retention in the combustor bed resulted in lower-than-desired sulfur species concentration in the flue gas.

Table 4-2. Composition and Heating Value of North Dakota Lignite Coals on an As-Received and Moisture-Free Basis

	Falkirk Coal Test 1		Freedom Coal 1 Test 1		Freedom Coal 2 Tests 2 and 3	
	As Received	**Dry**	**As Received**	**Dry**	**As Received**	**Dry**
Proximate Analysis, wt%						
Moisture	32.53	N/A[1]	30.37	N/A	37	N/A
Volatile Matter	23.2	34.39	32.15	46.18	27.29	43.32
Fixed Carbon (Ind)	32.63	48.37	33.52	48.14	31.94	50.69
Ash	11.63	17.24	3.95	5.68	3.77	5.99
Ultimate Analysis, wt%						
Hydrogen	6.25	3.86	6.64	4.65	7.04	4.6
Carbon	37.64	55.8	46.73	67.12	41.98	66.64
Nitrogen	0.63	0.94	0.61	0.88	0.57	0.91
Sulfur	0.68	1.01	0.86	1.24	0.69	1.09
Oxygen, Ind	43.17	21.16	41.20	20.43	45.95	20.78
Ash	11.63	17.24	3.95	5.68	3.77	5.99
Heating Value, Btu/lb						
	6290	9323	7966	11,441	7091	11,255

[1] Not applicable.
Note: The coal was floor-dried to achieve a target moisture concentration of 20%–22%.

Table 4-3. Ash Composition of North Dakota Lignite Coals, wt%

Component	Falkirk Coal	Freedom Coal 2 Tests 2 and 3
SiO_2	44.94	16.62
Al_2O_3	12.59	10.79
Fe_2O_3	8.33	8.78
TiO_2	0.50	0.22
P_2O_5	0.20	0.47
CaO	11.55	23.2
MgO	4.40	10.33
Na_2O	5.87	3.7
K_2O	1.78	0.51
SO_3	9.33	24.29
SrO	0.25	0.67
BaO	0.23	0.31
MnO	0.04	0.1

4.5.2 Combustor Operation

The FBG and EFG bed temperature and pressure vs. time profile shown in Figure 4-7 represents the overall operational history of the flue gas production process. The drop in the temperature and pressure is an indication of combustor downtime. As can be observed, during the shakedown test (FBG-042), the FBG was depressurized three times, primarily due to the agglomeration-related combustor operation shutdown. The decision to switch from Falkirk to Freedom coal was essentially to achieve uninterrupted operation of the combustor during subsequent DeSNO$_x$ tests (FBG-043 and FBG-044).

After a combustor/gasifier shutdown, the reactor bottom section was dismantled, examined, and ash agglomerates removed. During this downtime, the cause of the shutdown and other operational challenges was identified as higher-sodium fuel with possibly larger koalin particles, resulting in stagnant fluidization zones. Use of finer koalin and the discontinued use of limestone occurred after start-up. Figure 4-8 shows a photo of an agglomerate from the FBG-042 test period. A 2-in. × 3-in. particle was located in the lower section of the FBG. Light hammering with a short SS rod was required to disengage it from the reactor wall.

As mentioned, the use of Falkirk coal was discontinued, and shakedown testing continued with Freedom Mine coal, with analysis results also shown in Tables 4-2 and 4-3. The Freedom coal was successfully tested during shakedown, and subsequent tests continued to use Freedom coal.

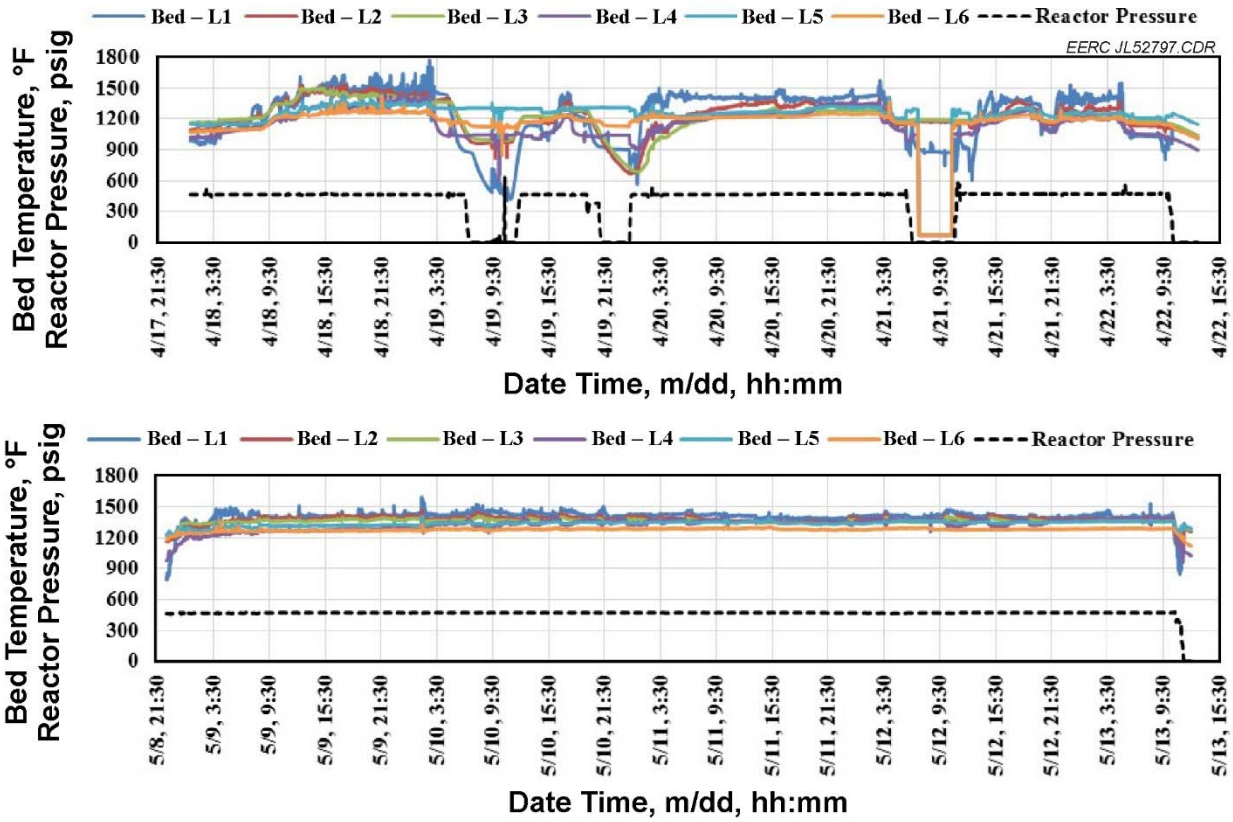

Figure 4-7. Reactor temperature and pressure for FBG-042 and FBG-043.

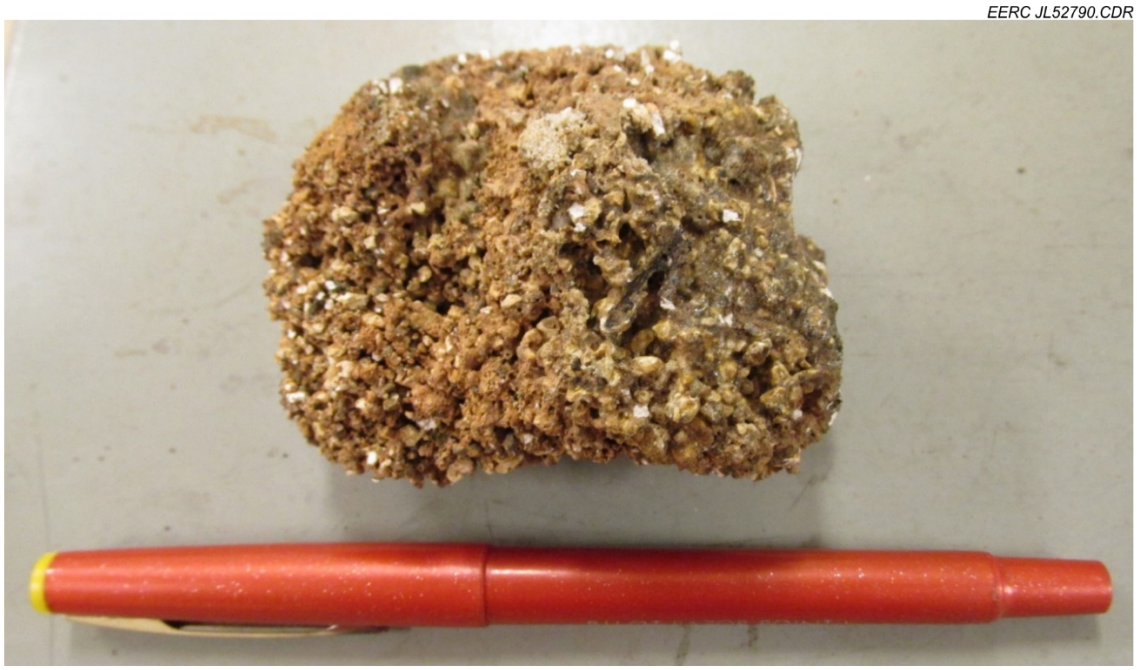

Figure 4-8. Photo of a Falkirk coal ash agglomerate removed during the FBG-042 test period.

The temperature and pressure time history for the FBG-043 test, depicted in Figure 4-7, represents successful flue gas production without any downtime. It should be noted that kaolinite (alkali-gettering agent) use was discontinued during this test (as well as during Test FBG-044). Because the steady production of flue gas with near-constant composition is critical for a DeSNO$_x$ column performance test, Test FBG-043 was considered successful in maintaining steady-state operation.

The temperature–pressure vs. time profile of the FBG during FBG-044 (Figure 4-9) also showed successful production of syngas for an extended duration except for about 4 hours of disruption on the fourth day of operation because of system plugging and loss of bed material, owing to operational challenges in the gasifier. The same profile for the EFG that was used as a syngas combustor for flue gas production shows disruptions primarily due to corrosion-based flue gas leakage from the low-temperature inlet piping near the DeSNO$_x$ column. During the 4-hour gasifier shutdown, the EFG and column were immediately brought online using N_2.

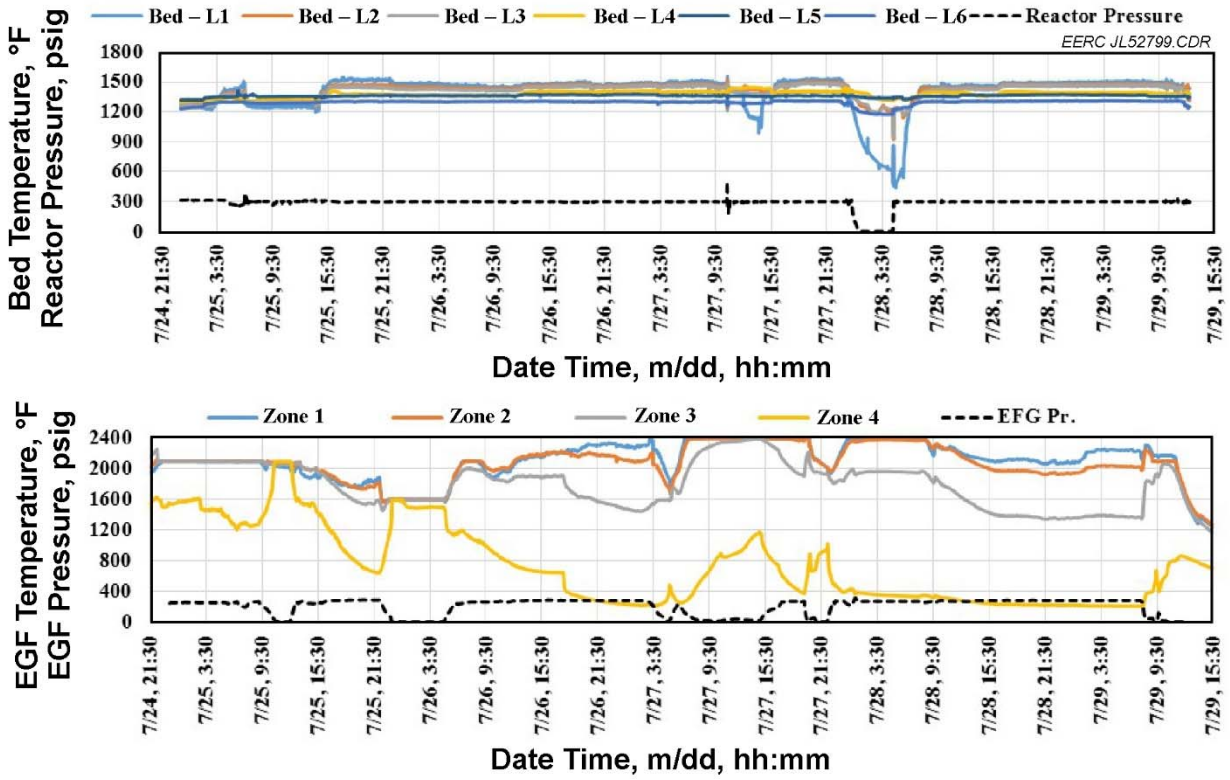

Figure 4-9. Reactor temperature and pressure vs. time profile for FBG-044.

4.5.3 *DeSNO$_x$ Process Evaluation*

The DeSNO$_x$ column was operated at target parameters specified by 8 Rivers Capital (see the test plan in Appendix A). During the first week of shakedown testing (FBG-043), continuous operation of the DeSNO$_x$ column was not achievable because of disrupted operation of the FBG, as discussed in the previous section. However, the test helped to develop a column-operating procedure, an effective gas-sampling and analysis procedure for the DeSNO$_x$ column, and a method for identifying a steady-state operating period procedure for conducting data analysis during the specified steady-state period. Periods where the column was online (especially during the testing on April 20) showed from the FTIR analysis that total NO and NO_2 were decreased from a range of 80 to 100 ppm to around 7 to 9 ppm when sampling after the DeSNO$_x$ column. This demonstrates better than a 90% removal of the NO_x species. The oxy-fired fluid-bed combustor was also making high levels of N_2O similar to the phenomena seen with other fluid-bed combustion systems. This phenomenon is mostly due to the lower operating temperatures experienced in fluid-bed combustors, with increasing operating temperature decreasing the formation of N_2O. Based on FTIR analysis, it appears that the DeSNO$_x$ column does not remove N_2O and may have slightly increased the amount of N_2O.

While FTIR did not measure all of the sulfur present in the flue gas (any H_2SO_4 present as an aerosol would not be measured), the amount of sulfur leaving the column was essentially less than 1 ppm, thereby demonstrating near-100% removal of sulfur in the column. Because limestone was not utilized during testing on April 20, the sulfur levels should have been very high (approximately 3700 ppm, with no inherent capture). These initial results suggest that the DeSNO$_x$ process has real potential to remove the sulfur and nitrogen species in a simple water scrubber. The question will be whether materials of construction can be designed that can handle the corrosive nature of the acidic water.

LGAs, combustion CEMs, and FTIR were used to analyze gases in and out of the DeSNO$_x$ column. The LGAs were used for major gas species composition measurement, and FTIR was used for determining the flue gas composition at the column inlet and outlet. The availability of a single FTIR system posed the challenge of measuring flue gas composition at the DeSNO$_x$ column inlet. Continuous monitoring of the major sulfur and nitrogen species was compromised because of this limitation. It was, therefore, critical that performance analysis be conducted during steady-state operation of the combustors (FBG and EFG) such that near-constant flue gas composition was maintained during the performance analysis period. Under these constant input conditions, intermittently measured average S and N species concentration across the DeSNO$_x$ column could be compared.

4.5.4 *Observed Steady-State Conditions During FBG-043 and FBG-044*

Table 4-4 shows the gas analyzers and the respective locations from which composition data were plotted to identify steady-state periods. The table also shows column-specific steady-state operation periods determined based on the gas analyzers. As can be seen, FTIR was shifted between the inlet and outlet of the DeSNO$_x$ column.

Table 4-4. Gas Analyzers and Locations

	Primary Steady State Based on Flue/Syngas Composition			Column-Specific Steady State		
Test	Analyzer ID	P&ID Location Port	Gas	Analyzer ID	P&ID Location Port	Gas
FBG-043	LGA106	Port A	Flue gas	FTIR	Port B and F across column	Sour and sweet flue gas
				CEM	Port G column outlet	Sweet flue gas
FBG-044	LGA39, Yokogawa process gas analyzer	Port B	Syngas	FTIR	Port D and E	Sour and sweet flue gas
				CEM	Port F	Sweet flue gas

4.5.4.1 FBG-043

LGA106 continuously monitored flue gas composition at the FBG outlet during the entire test period. Steady-state conditions were determined based on observed near-constant flue gas composition measured at the FBG outlet by LGA106. Because CO_2 was the main flue gas component, the beginning and end of the constant CO_2 concentration were one of the primary steady-state identifiers. The transitions and any high-CO-concentration phase during the test regime was considered a non-steady-state period. The high CO concentration was primarily owing to the fuel-rich condition created by small deviations in fuel feed rate. Table 4-5 shows eight steady-state periods (SS-1 to SS-8) with the shortest and the longest duration, 0.85 and 32.5 hr, respectively. Table 4-6 shows the steady-state composition of the flue gas generated during steady-state periods longer than 1 hr.

Table 4-5. Steady-State Periods Based on LGA106 Data for Test FBG-043

	Steady-State Start/End Date and Time				Steady-State
No.	Start	Time	End	Time	Duration
SS-1	5/9	8:49	5/10	1:54	17.08
SS-2	5/10	2:39	5/10	8:33	5.90
SS-3	5/10	10:00	5/10	21:07	11.12
SS-4	5/10	21:42	5/11	10:19	12.62
SS-5	5/11	11:00	5/12	19:28	32.47
SS-6	5/12	19:55	5/13	7:26	11.52
SS-7	5/13	8:20	5/13	9:11	0.85
SS-8	5/13	9:40	5/13	10:40	1.00

Table 4-6. Average Steady-State Composition of Flue Gas for Test FBG-043

No.:		SS-1	SS-2	SS-3	SS-4	SS-5	SS-6
Date and Time	Start:	5/9 08:49	5/10 02:39	5/10 10:00	5/10 21:42	5/11 11:00	5/12 19:55
	End:	5/10 01:54	5/10 08:33	5/10 21:07	5/11 10:19	5/12 19:28	5/13 07:26
Total Duration, hr:		17.08	5.90	11.12	12.62	32.47	11.52
O_2	vol%	2.0	1.1	0.9	0.7	2.8	1.0
N_2		5.1	4.1	3.7	3.6	3.6	3.4
CO_2		87.0	88.8	89.6	89.8	87.8	89.6
H_2O		5.9	6.0	6.0	5.7	6.0	6.4
NO	ppmv	117.10	84.50	106.02	54.45	32.57	71.06
NO_2		6.02	18.38	26.04	3.28	20.85	14.64
N_2O		30.57	21.80	21.15	14.09	31.35	16.35
SO_2		17.70	1.86	2.55	2.03	0.80	2.33
SO_3		1.09	0.66	0.39	0.88	0.05	0.39
COS		2.31	0.36	0.29	0.37	0.13	0.23
H_2SO_4		0.00	0.01	0.02	0.00	0.15	0.00

4.5.4.2 FBG-044

During two-stage operation, the analyzer port configuration significantly changed because the coal was gasified and syngas combusted in the EFG. LGA39 and the Yokogawa gas analyzers were brought online to determine syngas composition. Steady-state determination based on the data from these analyzers was based on the assumption that the elemental balance across the EFG remains constant if syngas composition is not changed.

Table 4-7 shows ten steady-state periods (SS-1 through SS-10), with the shortest and the longest duration, 1.5 and 19.9 hr, respectively. A total of 62.7 hr of steady-state operation of the FBG was recorded. Tables 4-8 and 4-9 show average syngas composition corresponding to the steady state shown in Table 4-7, measured by LGA39 and the Yokogawa analyzer, respectively.

Table 4-7. Steady-State Periods Based on LGA39 and Yokogawa Process Gas Analyzer Data for Test FBG-044

No.	Steady-State Start, Date and Time	Steady-State End, Date and Time	Duration, hr	
SS-1	7/25/16 15:54	7/25/16 17:24	1.51	
SS-2	7/25/16 18:06	7/25/16 22:17	4.19	
SS-3	7/25/16 22:49	7/26/16 7:10	8.36	
SS-4	7/26/16 13:06	7/26/16 20:02	6.94	FTIR steady state
SS-5	7/26/16 20:36	7/27/16 3:21	6.76	FTIR steady state
SS-6	7/27/16 4:16	7/27/16 10:55	6.66	
SS-7	7/27/16 16:21	7/27/16 18:05	1.74	
SS-8	7/27/16 18:30	7/27/16 22:13	3.72	
SS-9	7/28/16 12:04	7/29/16 7:57	19.89	FTIR steady state
SS-10	7/29/16 8:44	7/29/16 11:41	2.96	

Table 4-8. Average Steady-State Composition of Syngas Measured at the Gasifier Outlet by LGA39 for Test FBG-044

No.	CO	O_2	H_2S	N_2	H_2	CO_2	CH_4	HC	Difference (unknown)
	vol%								
SS-1	12.89	0.00	0.32	9.83	24.23	48.46	2.38	0.00	1.89
SS-2	13.19	0.07	0.37	5.13	24.18	53.02	2.07	0.00	1.96
SS-3	8.53	0.05	0.35	26.94	22.69	38.66	1.85	0.00	0.92
SS-4	12.10	0.00	0.34	4.19	18.73	62.21	1.67	0.00	0.75
SS-5	13.43	0.00	0.36	1.60	20.75	60.74	1.97	0.00	1.15
SS-6	13.46	0.01	0.43	1.85	29.19	50.85	2.82	0.00	1.39
SS-7	7.21	0.00	0.22	48.71	17.15	27.48	1.25	0.00	−2.02
SS-8	11.14	0.00	0.37	15.11	22.72	48.86	1.78	0.00	0.02
SS-9	15.19	0.00	0.36	1.25	20.80	59.37	2.58	0.00	0.45
SS-10	14.80	0.01	0.43	0.66	24.58	56.09	3.01	0.00	0.42

Table 4-9. Average Steady-State Composition Syngas Measured at the Gasifier Outlet by Yokogawa Gas Analyzer for Test FBG-044

No.	H_2	O_2	N_2	CH_4	CO	C_3H_6	C_3H_8	CO_2	C_2H_4	C_2H_6	H_2S	COS	Diff.
	vol%												
SS-1	29.2	0.0	10.8	3.9	13.5	0.0059	0.0002	42.31	0.0025	0.116	0.27	0.0000	−0.10
SS-2	29.0	0.1	4.5	3.6	14.5	0.0050	0.0006	49.82	0.0000	0.061	0.35	0.0007	−1.89
SS- 3	25.2	0.1	24.1	2.9	9.3	0.0052	0.0008	36.12	0.0000	0.057	0.32	0.0005	1.93
SS-4	19.7	0.1	4.0	2.7	13.3	0.0049	0.0005	57.37	0.0000	0.038	0.31	0.0007	2.51
SS-5	20.8	0.1	1.5	2.8	14.8	0.0049	0.0008	55.87	0.0000	0.043	0.33	0.0015	3.81
SS-6	27.8	0.1	1.0	0.9	14.8	0.0048	0.0008	46.68	0.0000	0.059	0.39	0.0029	8.32
SS-7	16.4	0.0	42.1	1.5	7.9	0.0059	0.0015	25.29	0.0027	0.061	0.19	0.0012	6.60
SS-8	20.9	0.1	12.6	1.6	12.2	0.0051	0.0009	44.95	0.0000	0.049	0.33	0.0013	7.25
SS-9	19.7	0.1	0.9	2.3	17.0	0.0050	0.0009	54.90	0.0001	0.067	0.32	0.0011	4.71
SS-10	22.9	0.0	0.7	5.3	16.6	0.00	0.00	51.56	0.00	0.078	0.37	0.00	2.45

It should be noted that two-stage operation allowed continuous syngas production, even when the EFG and/or column were not operational, owing to system leaks detected during the test run. The steady state periods shown in Table 4-7 are not indicative of column operation.

As depicted in Table 4-4, the FTIR was the only analyzer designated for measuring flue gas composition downstream of the EFG and DeSNO$_x$ column inlet. Since the impurity retention efficiency of the DeSNO$_x$ column requires both inlet and the outlet gas composition, the operation of the FTIR become a critical factor in evaluating column performance. The steady-state period of measurement was, therefore, overlapping with the availability of the FTIR system.

Table 4-10 shows the steady-state period unique to FTIR measurement that overlapped with the periods in Table 4-7 (marked by gray-shaded rows). It should be noted that the two-stage testing did not produce any N_2O in the flue gas because of higher syngas combustion temperatures experienced in the EFG syngas combustor.

4.6 Performance of the DeSNO$_x$ Column

DeSNO$_x$ spray column performance is determined based on the ability of the column to retain the sulfur and nitrogen species. In the packed-bed column, the mass transfer occurring is a function of the operating conditions, which can be best understood experimentally by initially determining percent retention of these species in the spray solvent (water in the present case). The difference between inlet and outlet concentrations of these species is the key input to the calculation of the retention ratio. This ratio is defined by the difference between the respective species mass injection rate and their output rate divided by the input rate (mass rate represented as mg/hr). This value, when expressed as percent retention, indicates the amount of impurities retained in the water within the column.

Table 4-10. Average Flue Gas Composition by FTIR for Test FBG-044

				SS-9				
No.:		**SS-4**	**SS-5**	**SS-9-1**	**SS-9-2**	**SS-9-3**	**SS-9-4**	**SS-9-5**
Date and Time	**Start:**	**7/26 17:01**	**7/26 20:36**	**7/28 13:00**	**7/28 13:54**	**7/28 15:29**	**7/28 16:39**	**7/28 20:58**
	End:	**7/26 20:02**	**7/27 3:21**	**7/28 13:25**	**7/28 15:26**	**7/28 16:09**	**7/28 20:58**	**7/29 7:51**
Total Duration, s:		**3.02**	**6.76**	**0.43**	**1.55**	**0.66**	**4.31**	**10.88**
H_2O	vol%	5.1	5.7	4.9	4.7	4.5	5.1	4.8
CO_2		83.0	86.4	76.3	84.2	88.1	89.5	88.7
*O_2		4.75	2.86	2.31	2.31	2.31	1.88	3.59
NO	ppmv	2.012	2.290	2.448	2.158	2.052	2.023	2.408
NO_2		0.000	0.000	0.000	0.000	0.000	0.000	0.000
N_2O		0.000	0.000	0.000	0.000	0.000	0.000	0.000
SO_2		765.7	805.7	485.8	644.1	623.5	680.5	600.8
SO_3		0.000	0.000	0.000	0.000	0.000	0.000	0.004
COS		0.20	0.03	0.00	0.10	0.00	0.00	0.14
H_2SO_4		2.92	5.51	0.00	0.28	1.11	0.64	3.18
NH_3		0.034	0.001	0.176	0.139	0.112	0.157	0.075
CO		40.2	2.9	2.7	109.3	6.6	10.9	67.3

The following section describes the primary outcome of the two tests (FBG-043 and FBG-044), including observed retention of sulfur and nitrogen species and the parameters contributing to the observed retention, such as pressure, temperature, flue gas and water injection rate, and gas residence time.

4.7 Column Operation

The temperature and pressure vs. time history depicted in Figures 4-7 and 4-9 showed continuity in operation and the main operating features of the one- and two-stage coal-to-flue gas conversion process during respective test weeks (FBG operated as a combustor during Tests FBG-042 and FBG-043 and as a gasifier for Test FBG-044). Column operation was initiated once a steady flue gas stream at the predetermined gas composition and operating pressures was attained. The measured parameters across the DeSNO$_x$ column (inlet and outlet), primarily temperature,

pressure, fluid flow rates, and gas composition, helped in monitoring column operation and later evaluating column performance. The recorded parameters for the Week 2 and 3 tests are presented in the following sections. An attempt was made to draw a comparison and individual test inferences from the experimental data by presenting near-identical plots for these tests in the same figure.

4.8 Temperature and Pressure vs. Time History

A high-level analysis of the two plots in Figure 4-10 shows that two-stage operation was relatively disruptive compared to single-stage operation, demonstrating that the unique conditions

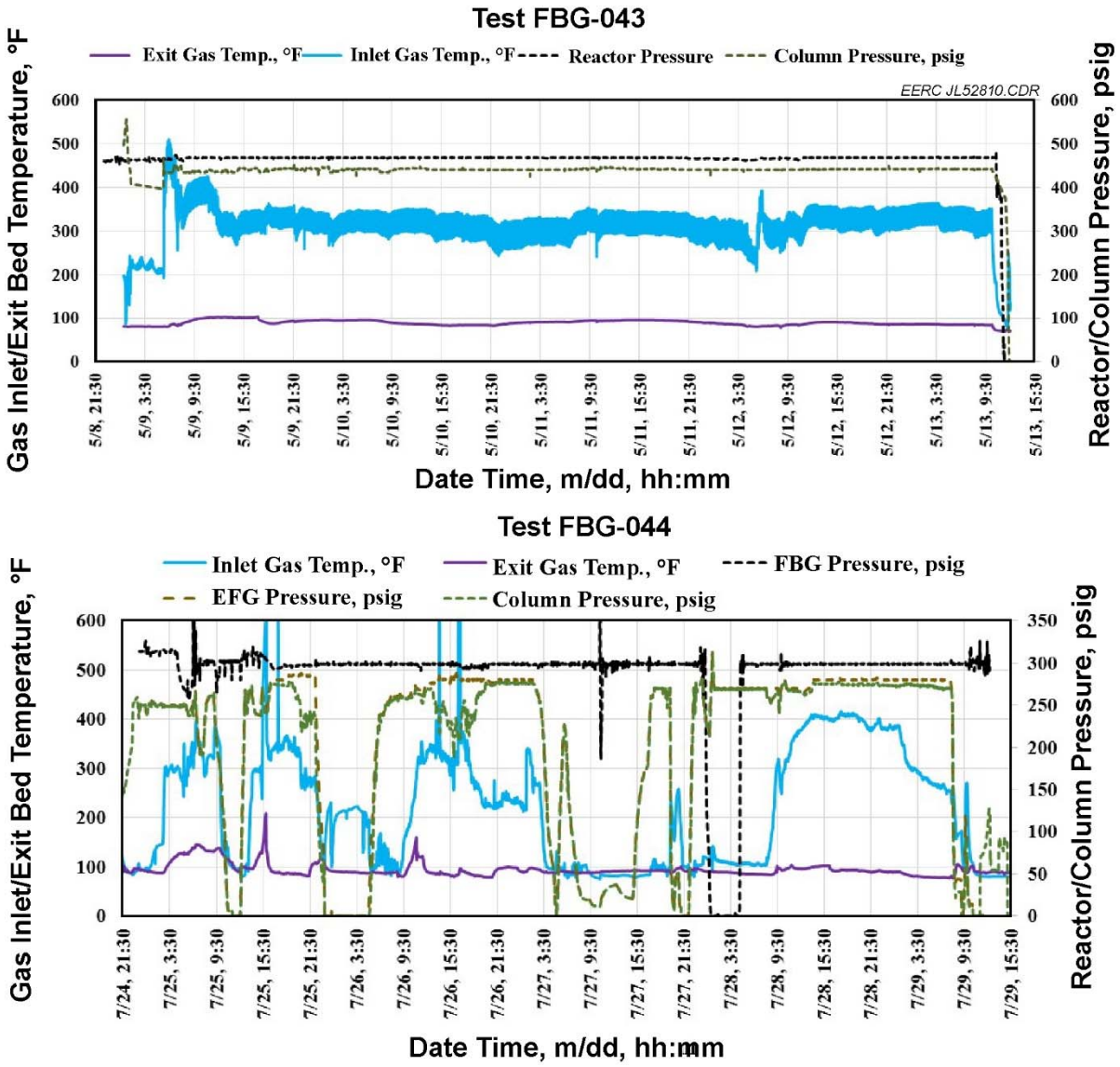

Figure 4-10. Plot of the operating pressures of the reactor (combustor and gasifier) and DeSNO$_x$ column and the temperature of the gas measured at the inlet and outlet of the column.

and complexities of a two-stage gasification process make it less reliable than single-stage process operation. Plugging by agglomerates caused interrupted gasifier operation during the entire FBG-043 test period and once at the end of the third day of the FBG-044 test period. Column operation as represented by column pressure and the gas temperature profile across the column showed the uninterrupted operation for Week 2, while the Week 3 test included five major disruptions, primarily related to gas leaks (four or five times) or a water leak (one time from the recirculation line). The FBG was operated at 468 and 299 psig, respectively, for Tests FBG-043 and FBG-044. Low-pressure operation in the later test was owing to the operating pressure restrictions on the EFG, which was used as a syngas combustor. The column operation pressures did not exceed 445 and 280 psig for Tests FBG-043 and FBG-044, respectively.

The average gas temperature at the column inlet and outlet was 320° and 95°F, respectively, for Test FBG-043. In the case of two-stage test operation, the gas was cooled in a tube-in-tube air heat exchanger. Hence, as can be seen in Figure 4-10, the inlet temperature significantly varied during Test FBG-044 EFG operation. The outlet gas temperature was also impacted because of inlet gas fluctuations, unlike in the earlier test. Except for two peak temperatures recorded at 203° and 154°F during the first and second day of operation, the exit gas temperature was maintained below 100°F, about 5°F higher than that recorded during the earlier test.

4.9 DeSNO$_x$ Flue Gas and Water Flow Rates

The impact of water recirculation and freshwater injection rate on column performance is critical in arriving at an operation optimization strategy, required for developing full-scale technology design. As a part of this learning process, the time history of these parameters along with the pH of the water discharged from the column are plotted for Tests FBG-043 and FBG-044. As can be seen in Figure 4-11, the average recirculation rate was maintained at 27.5 L/hr (7.3 gal/hr) during Test FBG-043 and 112 L/hr (29.5 gal/hr) for Test FBG-044, a value four times greater than the previous test. As part of the study conducted for Test FBG-043, freshwater was injected after 42 hr of operation to understand the variation in pH. A constant column sump water level was maintained during the water injection phase by discharging an equal amount of water injected into the column. As can be observed, the water injection rate and corresponding dilution effect led to the increase in pH. This observation helped to arrive at the strategy of maintaining a continuous freshwater injection and acidic water discharge rate for the following test. Both of these water flow parameters were held constant during Test FBG-044 in accordance with this plan.

A similar time history for Test FBG-044 is presented in Figure 4-11. As can be seen in the figure, the water injection and recirculation rate in the column were maintained constant during Test FBG-043. The pH = 1.57 was an average value observed during the entire test except for a slight increase in the value during the last 6 hr, which will be explained in a later section.

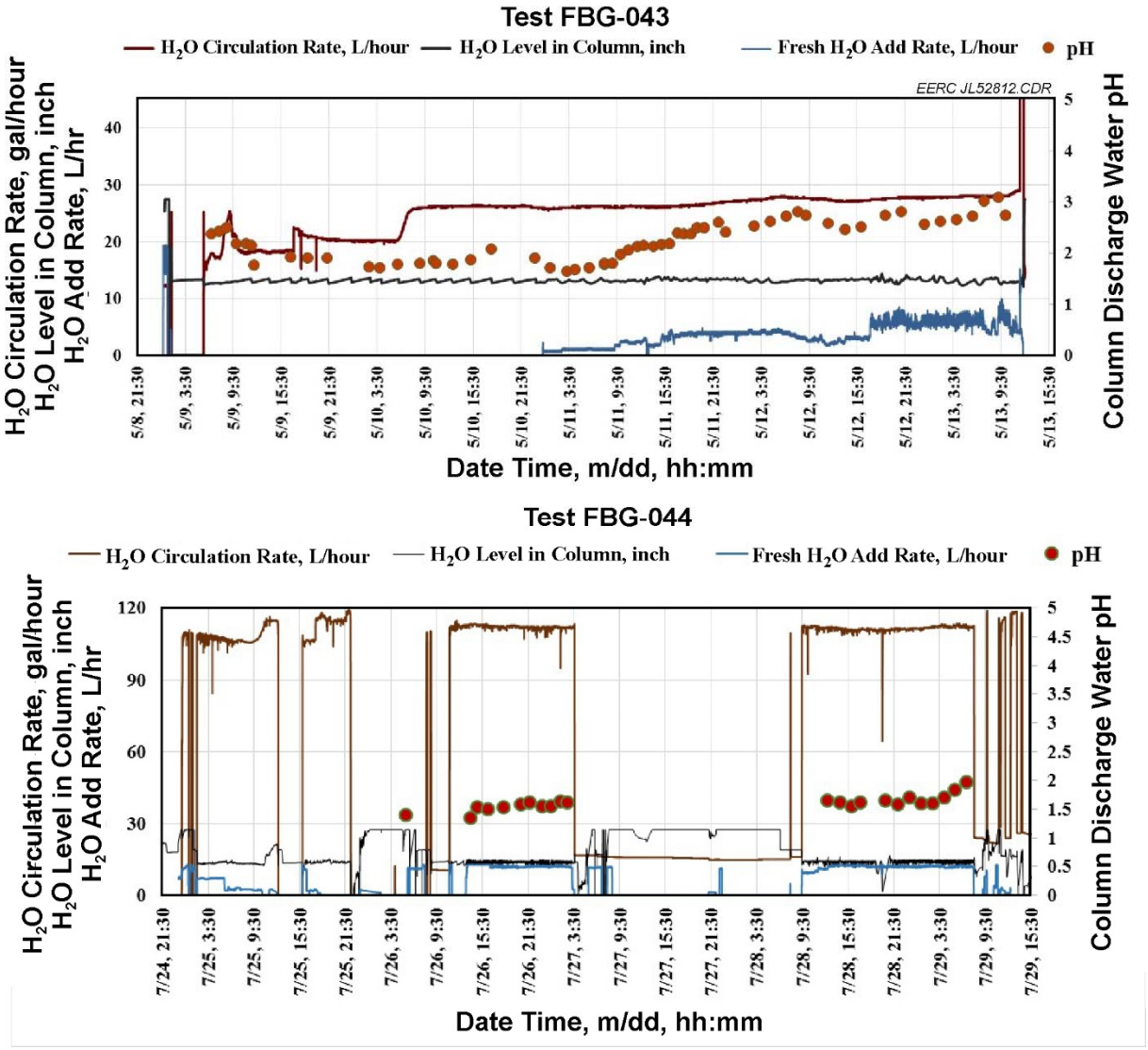

Figure 4-11. Time history of $DeSNO_x$ column water circulation rate, freshwater injection rate, sump water level, and pH obtained for Tests FBG-043 and FBG-044.

4.10 Column Flue Gas Flow Rates

The total impurity loading in the $DeSNO_x$ column is proportional to the flue gas flow rate injected into the column. The gas flow rate also corresponds to the gas residence time in the column during which gas–liquid contact occurs. Tables 4-11 and 4-12 show average gas flow conditions in the column for FBG-043 and FBG-044 at their respective steady-state conditions, including flow rate, pressure, inlet and exit temperature, and calculated residence time (with zero voidage). The tables also show the column dimensions (internal diameter and effective length). Figure 4-12 shows the flow rate vs. time profile for the single-stage and two-stage experiments.

Table 4-11. Average Steady-State Gas and Scrubber Water Flow Rate, Column Pressure and Temperatures, Gas Residence Time, and Column Dimensions for Test FBG-043

No.	Wet Gas Flow Rate at Column Inlet, scfh	Column Pressure, psig	Exit Gas Temp., °F	Inlet Gas Temp., °F	Residence Time, s	$DeSNO_x$ Column Effective Dimensions		
1	94.3	441.9	100.2	320.1	518.7	i.d., in.	Length, in.	Vol., ft^3
2	94.4	441.6	100.6	319.2	517.9	3.07	128	0.548
3	90.7	442.7	90.3	313.6	547.2	Average Water Flow Rate = 7.3 gal/hr		
4	81.5	441.5	102.2	300.1	607.6			
5	84.9	441.8	98.3	303.1	584.7			
6	87.2	442.5	95.3	327.9	560.6			

Table 4-12. Average Steady-State Gas and Scrubbing Water Flow Rate, Column Operating Conditions, Gas Residence Time, and Column Dimensions for Test FBG-044

No.	Wet Gas Flow Rate at Column Inlet, scfh	Column Pressure, psig	Exit Gas Temp., °F	Inlet Gas Temp., °F	Residence Time, s	$DeSNO_x$ Column Effective Dimensions		
SS-4	847.0	238.4	83.2	334.5	32.1	i.d., in.	Length, in.	Vol., ft^3
SS-5	654.5	273.0	94.7	247.3	50.0	3.07	128	0.548
SS-9	869.3	273.0	88.9	358.0	34.8	Average Liquid Flow Rate = 29.6 gal/hr		
	676.8	273.0	88.9	358.0	44.7			

Total gas flow into the column for Test FBG-044 was measured downstream of the column. This flow rate was determined by adding the following three independent gas flow streams:

1) EFG recirculation gas
2) FBG freeboard recycle flue gas
3) Exhaust or gas leaving the system through a vent line

In calculating total flow rate of the flue gas injected into the column on a volume basis, the volume of the condensed gases, mainly moisture, was included. FTIR determined the moisture content in the column-fed gas on volume basis. Tables 4-11 and 4-12 show corrected wet gas flow rates for both tests.

Table 4-11 and 4-12 data clearly show that the gas flow rates for Test FBG-044 are about a magnitude higher than for Test FBG-043. Corresponding to the higher flow rate, Test FBG-044

gas residence time in the column is about an order of magnitude lower in the case of the earlier test. The table shows the average gas flow rate distribution data for the identified steady-state periods. The data show a greater than 80% gas flow is recycled into the column. This recycled gas is used as a diluent in the oxy-syngas combustion process occurring in the EFG. Figure 4-13 shows the flow rate of injected gases in the EFG.

The water recirculation pump was operated at the maximum range of the flowmeter to accommodate the changed impurities throughput resulting from increased gas flow rate in Test FBG-044. The sensible heat from the water was rejected with the help of a glycol-cooled heat exchanger. This indirect water cooling helped to maintain the exit gas temperature (see Figure 4-10) within the targeted 100°F. Table 4-13 shows the flow distribution at the column downstream, showing percent flue gas recycled through the EFG for Test FBG-044.

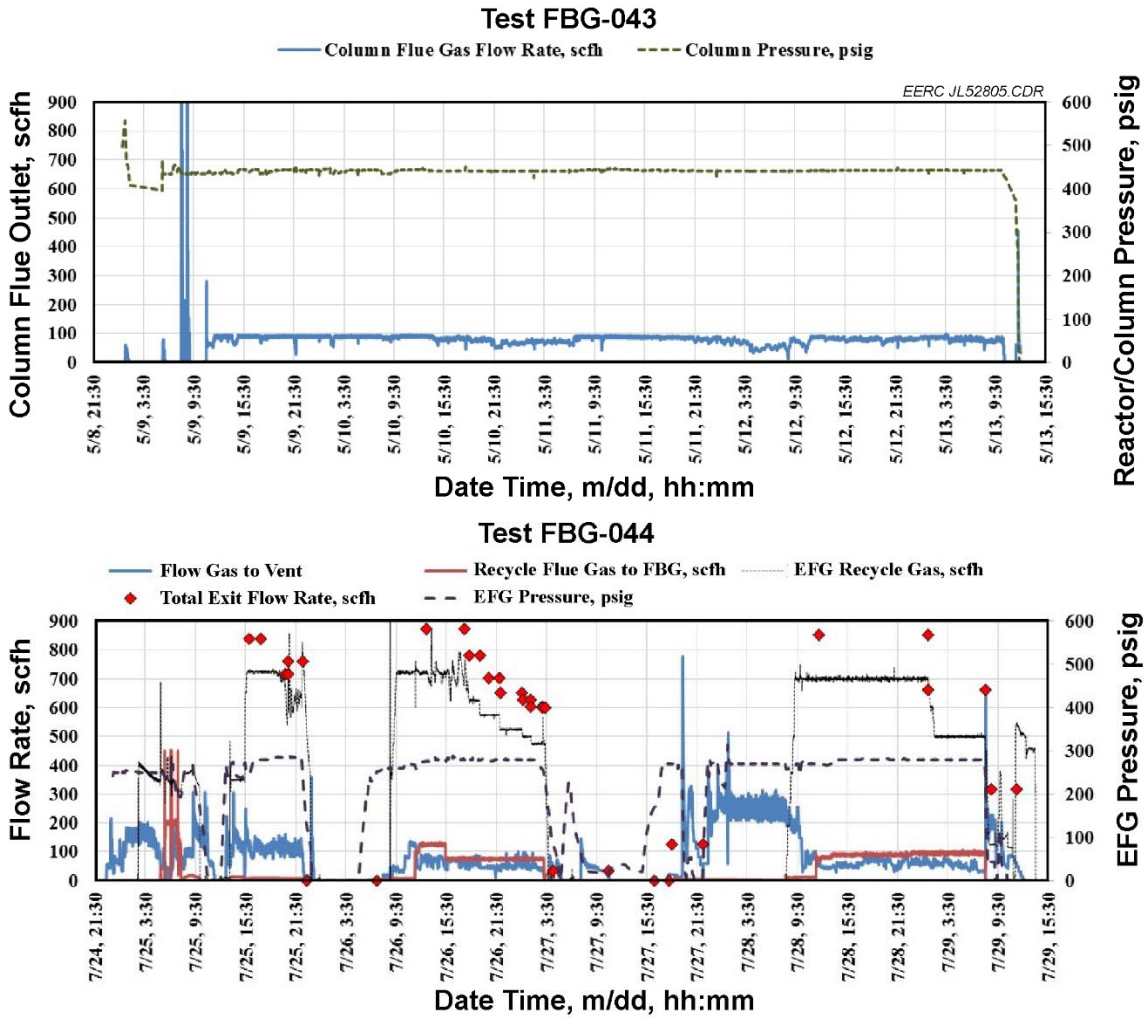

Figure 4-12. Flue gas flow rates vs. time history for Tests FBG-043 and FBG-044. The red dots shown in the FBG-044 plot depict average total flow rate corresponding to the time shown on the x-axis.

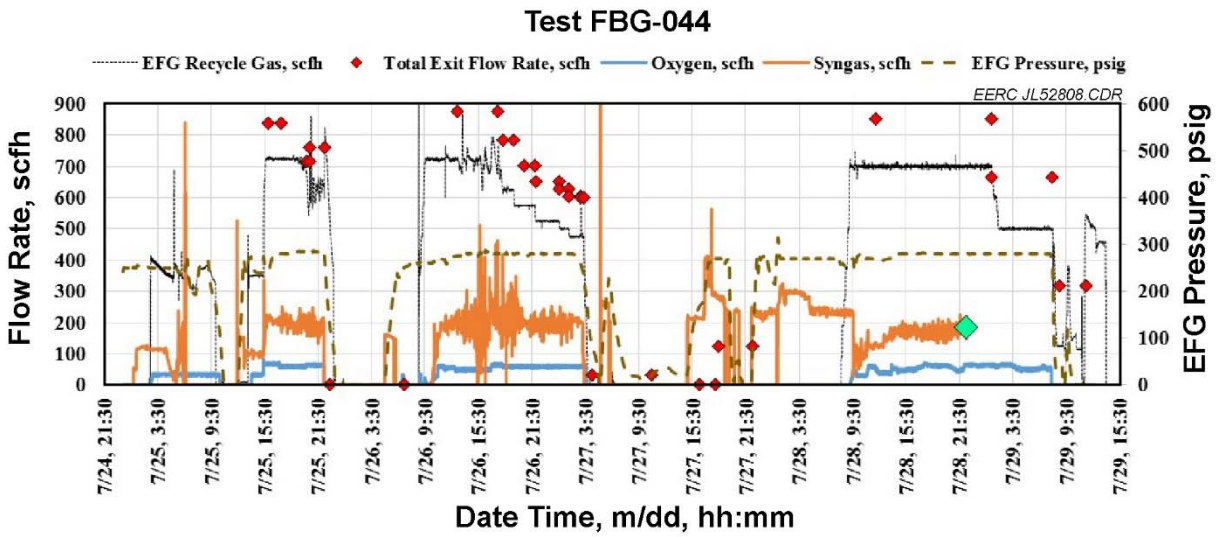

Figure 4-13. EFG pressure and flow rate vs. time history of gases (syngas, oxygen, and recycle gas) injected into the EFG.

4.11 DeSNO$_x$ Column Performance

The percent retention of S and N species is obtained based on their measurement at the column upstream and downstream, respectively. The FTIR and CEM were primarily utilized to determine the sample flue gas concentration at the inlet and outlet of the column. The port locations for respective analyzers was presented in Table 4-4 and was shown in the test-specific P&ID in Figures 4-5 and 4-6. The flue gas composition at the DeSNO$_x$ column inlet were presented in Tables 4-6 and 4-10 for Tests FBG-043 and FBG-044, respectively. Tables 4-14 and 4-15 show the experimental data averaged over the specified steady-state period for N and S species, respectively, for the two tests.

4.12 Nitrogen Species Retention

Table 4-14 shows the amount of N species injected into the DeSNO$_x$ column significantly differed between Tests FBG-043 and FBG-044, owing to the difference in the combustion processes (direct coal combustion vs. syngas combustion). This is primarily the result of the fuel-bound nitrogen being directly converted to NO$_x$ under oxy-combustion conditions seen in the single-stage testing. The fuel-bound nitrogen would be converted to water-soluble ammonia and, to a lesser extent, hydrogen cyanide that would be removed in the moisture condensation train located at the back end of the FBG gasifier. Thus the syngas-fired EFG oxy-combustor would only be combusting a syngas with a very small amount of nitrogen. Hence, any NO$_x$ being formed would likely have come from a thermal mechanism. It is believed that the flame temperature in the oxy-fired EFG syngas combustor was not high enough to generate much thermal NO$_x$. Although the injected flue gas flow rate in Test FBG-043 was an order of magnitude lower, the gaseous N species formed in the case of direct coal combustion were much higher. An attempt to

Table 4-13. DeSNO$_x$ Column Downstream Flue Gas Distribution and Percent EFG Gas Recycle Rate

Steady-State									
					Gas Flow Rate at Column Outlet, scfh				
No.	ID.	Start Date/ Time, m/dd, h:min	End Date/ Time, m/dd, h:min	Period, hr	To EFG	To FBG	To Vent	Total Flow	EFG Recycle
SS-1	SS-1-Int-1	7/25, 15:54	7/25, 17:19	1.4	725	0	113	838	87%
SS-2	SS-2-Int-1	7/25, 20:14	7/25, 20:35	0.3	602	0	114	716	84%
	SS-2-Int-2	7/25, 20:36	7/25, 22:17	1.7	646	0	114	760	85%
SS-3	SS-3-Int-1	7/25, 22:49	7/26, 7:07	8.3	0	0	0	0	0%
SS-4	SS-4-Int-1	7/26, 13:06	7/26, 17:39	4.6	718	92	65.3	875	82%
	SS-4-Int-2	7/26, 18:17	7/26, 19:29	1.2	625	92	65.3	782	80%
SS-5	SS-5-int-1	7/26, 20:36	7/26, 21:50	1.2	575	73	54	702	82%
	SS-5-Int-2	7/26, 21:56	7/27, 0:32	2.6	525	73	54	652	81%
	SS-5-Int-3	7/27, 0:36	7/27, 1:38	1.0	500	73	54	627	80%
	SS-5-Int-4	7/27, 1:38	7/27, 3:01	1.4	475	73	54	602	79%
	SS-5-Int-5	7/27, 3:01	7/27, 3:21	0.3	473	73	54	600	79%
SS-6	SS-6-int-1	7/27, 4:16	7/27, 10:55	6.7	0	0.0	32	32	0%
SS-7	SS-7-int-1	7/27, 16:21	7/27, 18:05	1.7	0	0.0	0	0	0%
SS-8	SS-8-int-1	7/27, 18:30	7/27, 22:13	3.7	0	0.0	125	125	0%
SS-9	SS-9-Int-1	7/28, 12:04	7/29, 1:07	13.1	700	91.4	60.3	852	82%
	SS-9-Int-2	7/29, 1:08	7/29, 7:57	6.8	511	91.4	60.3	663	77%

operate the EFG at a higher temperature without injecting additional nitrogen to promote higher NO_x formation failed to improve the species concentration in the flue gas. The NO_x analyzer-measured composition at the column outlet (CEM) was close to its low calibration/measurement limit. The FTIR had no challenges measuring the lower concentration of both species; however, unlike in Test FBG-043, the FTIR was used more for determining upstream composition than downstream composition. Even though the inlet NO_x as measured by the FTIR was very low (2 to 3 ppm), the outlet as measured by the CEM and by a few spot checks with the FTIR generally showed almost no NO_x (<1 ppm), indicating that the column was still effectively removing most of the NO_x entering it.

Figure 4-14 shows the plot of N species concentration, N_2 concentration in syngas, O_2, and EFG recycle gas vs. time to understand the factors that contribute to column performance.

The syngas–N_2 profile shows the <5% (based on volume) N_2 concentration in the fuel is one of the factors contributing to the low NO_x concentration produced in the syngas. This is unlike the case of the oxy-combustion process observed in Test FBG-043.

Table 4-14a shows that with the exception of SS-4, NO and NO_2 retention exceeds 90% and 80% (on a weight basis), respectively. In addition, with the exception of SS-1, the N_2O retention was negative, which indicates that N_2O was formed during the scrubbing process.

Table 4-14b shows greater than 77% NO reduction was obtained in Test FBG-044. NO_2 and N_2O were below the detection limits of the analyzers. Because no N_2O was measured going into or out of the scrubber column during the two-stage testing, the possibility that the $DeSNO_x$ column itself could promote the formation of N_2O is less of a concern. This phenomenon is likely dependent on residence time as well as the specific gas concentrations.

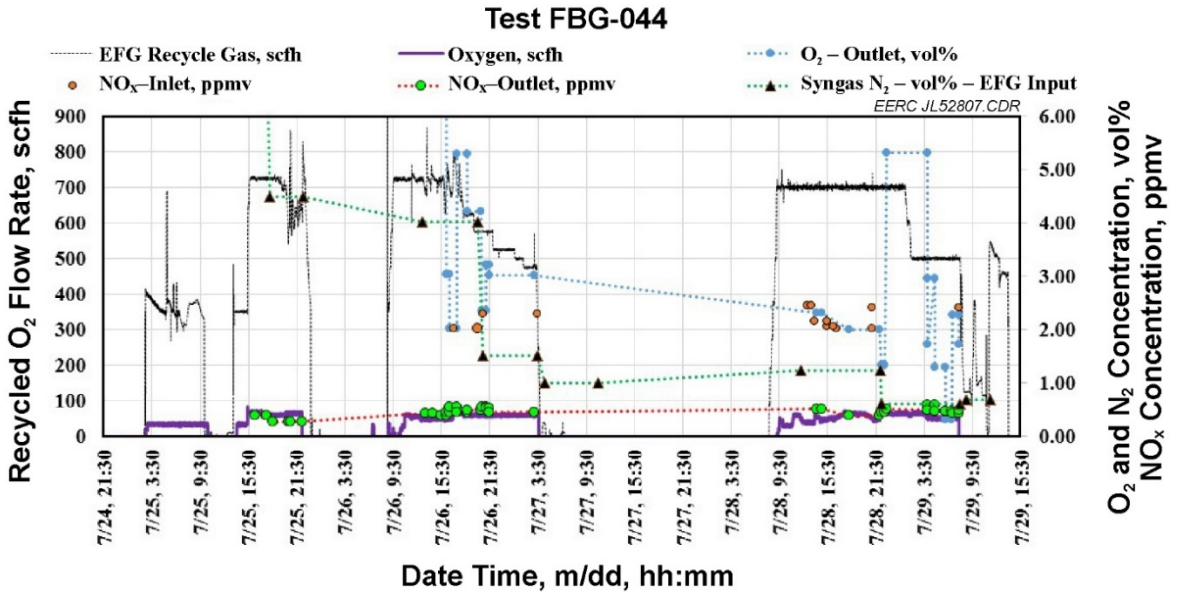

Figure 4-14. Plot of N_2, O_2, and N species concentration and EFG recycle gas flow rate vs. time history for Test FBG-044.

Table 4-14. Nitrogen Species Retention Observed in the DeSNO$_x$ Column for a) Test FBG-043 and b) Test FBG-044

a) FBG-043

Steady-State Period	Port A or B Inlet, mg/hr				Port G Outlet, mg/hr				% Retention of N Species			pH Column Sample			Water Addition Rate, lb/hr
	NO	NO_2	N_2O	Total NO_x	NO	NO_2	N_2O	Total NO_x	NO	NO_2	N_2O	Mean	Max.	Min.	
1	384.4	30.3	147.2	561.8	10.5	6.0	140.4	156.9	97.3	80.3	4.6	2.01	2.48	1.71	0.00
2	276.9	92.3	104.8	474.0	15.8	10.3	118.6	144.7	94.3	88.8	−13.2	1.75	1.78	1.7	0.00
3	334.8	126.1	97.9	558.8	15.3	10.0	114.3	139.5	95.4	92.1	−16.7	1.87	2.07	1.76	0.00
4	154.4	14.3	58.6	227.3	19.2	9.5	85.1	113.9	87.5	33.5	−45.3	1.75	1.96	1.62	2.38
5	96.1	94.3	135.6	326.0	9.1	5.0	170.3	184.4	90.5	94.6	−25.6	2.42	2.79	2.40	7.9
6	215.2	68.0	72.6	355.7	11.2	4.3	121.5	136.9	94.8	93.7	−67.3	2.71	3.00	2.55	13.8

b) FBG-044

SS No.	N Species Concentration at Column Inlet, mg/hr			N Species Concentration at Column Outlet, mg/hr			Percent Retention			O_2 at Column Outlet, vol%	Water Injection Rate into Column, mL/minute
	NO	NO_2	N_2O	NO	NO_2	N_2O	NO	NO_2	N_2O		
SS-4	59.2	0.0	0.0	13.6	0.0	0.0	77.1	0.0	0.0	3.9	197.5
SS-5	52.1	0.0	0.0	10.0	0.0	0.0	80.8	0.0	0.0	3.2	199.6
SS-9	65.2	0.0	0.0	59.9	0.0	0.0	8.1	0.0	0.0	3.7	201.8
	61.1	0.0	0.0	11.6	0.0	0.0	81.1	0.0	0.0	3.7	
	74.1	0.0	0.0	13.6	0.0	0.0	81.6	0.0	0.0	3.7	
	53.4	0.0	0.0	11.3	0.0	0.0	78.8	0.0	0.0	1.7	

Note: Discontinuity in steady-state numbering is the result of either the column or FTIR gas analyzer being nonoperational or unavailable during steady-state operation of the FBG and EFG.

Earlier studies on N_2O formation in the mixture of NO_x, SO_2, and water were conducted by Muzio et al. (40). The study showed the formation of N_2O in the three-reactant system, particularly when the combustion products were stored. The results indicated that several hundred ppm of N_2O was formed. Although current test conditions are different from that of the Muzio et al. study, the general inferences drawn should be considered related to N_2O formation. To further clarify this, equilibrium calculations were conducted to understand the effect of both pressure and temperature on N and S species formation.

At equilibrium, in reacting a mixture of NO, SO_2, and water in weight proportions of 0.036/0.106/99.86 (an observed $DeSNO_x$ column condition during Test FBG-043), Figure 4-15 shows the nondimensional mass fraction (mf) of different N and S species at equilibrium conditions obtained by taking the ratio of mf of these species at 30-bar and 1-bar reactor conditions. As can be seen in the plot in Figure 4-15, both pressure and temperature have a significant effect on not only formation of N_2O (which was measured in the present case) but the relative fraction of five other N species (N_2O_5, N_2O_4, HNO_3, HNO_2, NO_2, N_2O) that also have been shown to have significant impact on these parameters. The increase in the value of the ratio with temperature indicates that the pressure has a noticeable effect on the mf of N or S species at equilibrium. Spray column operation with temperatures of 90° and 100°F could be justified based on these observations of maintaining a low N_2O production. It is not expected that the $DeSNO_x$ process will introduce large amounts of N_2O. However, the species should certainly be monitored in future testing.

4.13 Sulfur Species Retention in the $DeSNO_x$ Column

Table 4-15 shows the amount of S species injected and removed in the $DeSNO_x$ column. As can be seen, the concentrations of S species are significantly different for Tests FBG-043 and FBG-044. Unlike NO_x concentrations in the steady state (higher for Test FBG-043 and lower for Test FBG-044), the S species concentration shows an opposite trend (3 orders of magnitude greater in the case of Test FBG-044 as compared to the earlier test). This order-of-magnitude difference is likely owing to:

1) The use of limestone in direct coal combustion (Test FBG-043) that effectively captured more than 95% sulfur in the combustor bed. Later, the use of limestone was discontinued to produce more S species in the flue gas.

2) Injected flow rate in the column for Test FBG-044, an order of magnitude higher because of more than 80% volume of the flue gas was recycled in the EFG combustor.

SO_2 and SO_3 retention of 98% and 100% were found during Test FBG-043 SS-4 where the low retention for the NO and NO_2 species was observed. Clear inferences could not be drawn except that the S species loading was lower than expected and, therefore, high capture was possible during Test FBG-043. It should be noted that the freshwater injection rate was zero for the first three steady-state periods, SS-1 through SS-3. This resulted in lowering water pH or maintaining a low value during the first three steady-state periods, as seen in Figure 4-11. The drop in SO_3 retention clearly showed the effect of water becoming more acidic. With initiation of freshwater

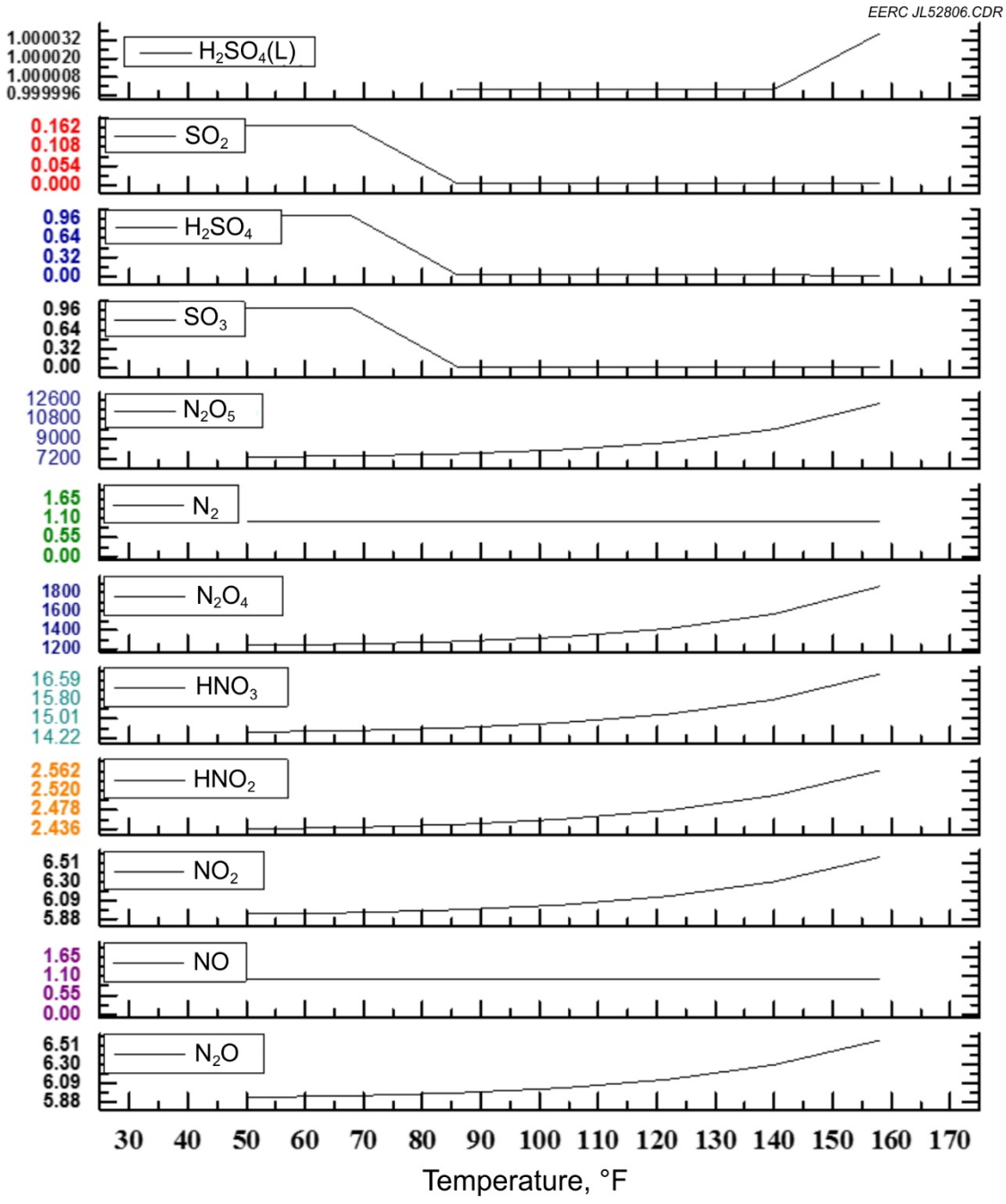

Figure 4-15. Ratio of mass fraction of S and N species formed at 30 bar and 1 bar vs. temperature for a SO_2–NO–H_2O reaction system (reactant weight ratio 0.036/0.106/99.86).

Table 4-15. Sulfur Species Retention Observed in the DeSNO$_x$ Column for a) Test FBG-043 and b) Test FBG-044

a) Test FBG-043

Steady-State Period	Port A or B Inlet, mg/hr				Port A or B Outlet, mg/hr				S Species % Retention				pH Column Sample			Water Addition Rate, lb/hr
	SO_2	SO_3	COS	H_2SO_4	SO_2	SO_3	COS	H_2SO_4	SO_2	SO_3	COS	H_2SO_4	Mean	Max.	Min.	
1	124.0	9.6	15.1	0.0	2.1	0.5	1.7	0.0	98.3	94.6	88.7	–	2.01	2.48	1.71	0.00
2	13.0	5.8	2.3	0.1	1.0	1.2	1.3	0.0	92.6	78.5	43.6	100.0	1.75	1.78	1.7	0.00
3	17.2	3.2	1.8	0.2	0.9	1.2	1.3	0.0	94.6	62.9	30.6	100.0	1.87	2.07	1.76	0.00
4	12.3	6.6	2.1	0.0	0.3	0.0	1.8	0.0	98.0	100.0	16.5	–	1.75	1.96	1.62	2.38
5	5.0	0.4	0.8	1.5	0.0	0.1	0.8	0.0	100.0	74.5	−3.4	100.0	2.42	2.79	2.40	7.9
6	15.0	3.1	1.4	0.0	0.1	0.0	0.9	0.0	99.4	99.4	34.3	–	2.71	3.00	2.55	13.8

b) Test FBG-044

No.	S-Species Concentration at Column Inlet, mg/hr				S-Species Concentration at Column Outlet, mg/hr				Percent Retention				O_2 at Column Outlet, vol%	Water Injection Rate into Column, mL/minute
	SO_2	SO_3	COS	H_2SO_4	SO_2	SO_3	COS	H_2SO_4	SO_2	SO_3	COS	H_2SO_4		
4	48,064.0	0.0	11.9	274.9	12,513.0	0.0	0.0	0.0	74.0	0.0	100.0	100.0	3.9	197.5
5	39,081.6	0.0	1.6	401.1	6053.6	0.0	0.0	0.0	84.5	0.0	100.0	100.0	3.2	199.6
9	41,509.3	0.0	6.3	27.4	2595.5	7.8	0.0	0.0	93.7	0.0	100.0	100.0	3.7	201.8
	43,855.7	0.0	0.3	62.0	6467.2	0.0	0.0	0.0	85.3	0.0	100.0	100.0	3.7	
	34,933.9	0.0	3.3	575.6	5015.2	0.0	0.0	0.0	85.6	0.0	100.0	100.0	3.7	
	30,493.7	0.4	8.8	102.2	16,074.8	0.0	0.0	0.0	47.3	0.0	100.0	100.0	1.7	

Note: Discontinuity in steady-state numbering is due to either the column or FTIR gas analyzer being nonoperational or unavailable during the operation of the FBG and EFG.

injection, the retention increased. The freshwater injection rate increase from 5.2 L/hr (1.4 gph) to 30.4 L/hr (8.0 gph) showed a marked increase in sulfur retention along with the increase in pH (see Figure 4-11). It was concluded from this test that near 100% retention can be achieved if sulfur loading is kept low and freshwater injection in continuously maintained.

This also means that if sulfur (or impurity) loading increases, freshwater injection becomes essential to the maintenance of constant column performance.

Sulfur species, particularly SO_2 retention during Test FBG-044, was observed to be greater than 74% in the case of the highest-recorded inlet sulfur loading. Decrease in SO_2 (sulfur) loading by about 18% showed an increase in retention to values above 84%. Water injection and recirculation rates were maintained constant (see Figure 4-11) during this test.

To understand the effect of excess oxygen in the flue gas, particularly in the case of the two-stage flue gas production process as expected in Allam Cycle power generation, the volume concentration of O_2 corresponding to each steady state is presented in Table 4-15b. As can be seen in SS-9-4, a marked reduction in S retention was observed with reduction in O_2 concentration in the flue gas (to a low value of 47.3%). This was due to less SO_2 being converted to the highly water-soluble SO_3/H_2SO_4 species. If the sulfur species enters the column still as SO_2, the retention will be significantly decreased. The reduction in EFG recycle flow rate (see Figure 4-12, 7/29, 0:30) significantly reduced SO_2 loading in the column. Based on FTIR measurements, the sulfur loading was the lowest at this point in time (36% of the highest value).

Figure 4-16 shows the plot of SO_2 (column inlet and outlet) and O_2 (column outlet) concentration vs. time and EFG recycle gas and oxygen injection rate vs. time for Test FBG-044. Figure 4-17 shows the SS-9 specific plot of SO_2 concentration recorded at the inlet and outlet of the column along with the O_2 concentration profile. Because SO_2 retention was lower, especially when O_2 concentrations were low, changes in recycle flue gas rates to the EFG oxy-combustor would have a significant impact on the sulfur loading to the column. Lower flow rates would recycle less SO_2 back to the column.

Figure 4-17 shows prominently the effect of oxygen variation on SO_2 concentration across the column. Both of these plots show that the increase in oxygen reduces the SO_2 owing to its conversion to SO_3, which eventually is retained in the $DeSNO_x$ column, resulting in decreased SO_2 concentration in the outlet. Quite the opposite effect occurs when the O_2 concentration is reduced. Thus the excess oxygen in the flue gas has a distinctly observable effect on SO_2 capture. However, this leads to the risk of acid corrosion in the column upstream if at a point in time the gas or the flue line temperature drops below the dew point of the complex mixture.

A series of corrosion-related failures were recorded during Test FBG-044 as a result of sulfuric acid condensation in the column inlet piping. A better understanding of the effect of operating conditions (pressure and multicomponent flue gas) on acid dew point in the present context needs to be explored further to avoid corrosion failure recorded during the last test. The observations on corrosion failure are presented in the following section, with the goal of developing future strategies for tackling this challenge.

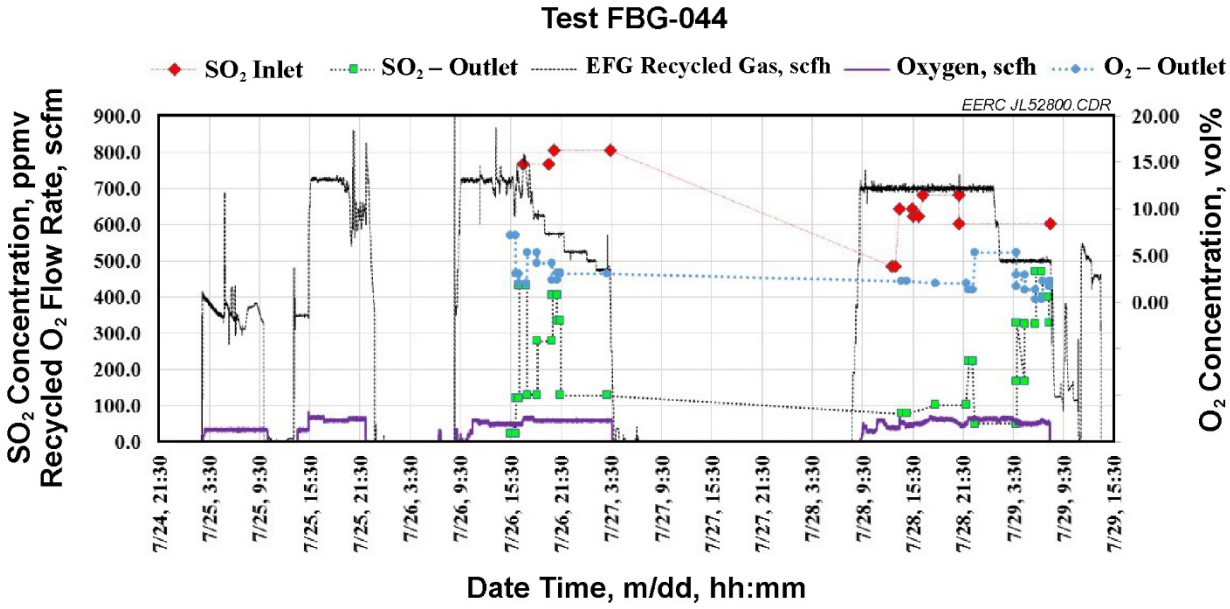

Figure 4-16. Plot showing SO_2, SO_3, and O_2 concentration vs. time and EFG recycle gas and oxygen injection rate vs. time for Test FBG-044.

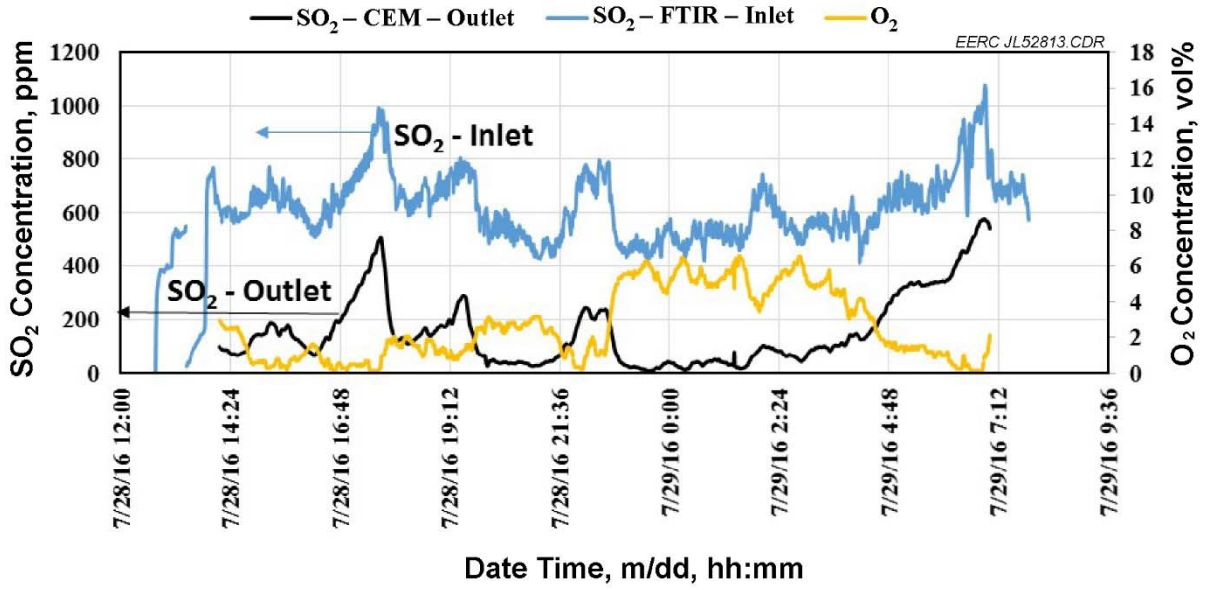

Figure 4-17. Time history of SO_2 concentration recorded at the inlet and outlet of the column along with the O_2 concentration profile.

4.14 Corrosion Failures During Test FBG-044

4.14.1 Accelerated Corrosion Mechanism

During pilot-scale testing, some accelerated corrosion of SS tubing and fittings was experienced on the inlet line and water sump pot and lower 2 ft of the $DeSNO_x$ column. Corrosion through the inlet tubing was experienced in less than 1 week of testing. Observation and analysis of these affected parts indicated that a high level of corrosion with pitting was occurring. Literature review revealed a situation in which the inlet piping to the column was cooled through an air-cooled heat exchanger to get the exit temperature from the EFG down to the desired inlet temperature between 250° to 300°F. At this temperature range, the moisture in the flue gas stream has not yet started to condense; however, the sulfur dioxide has been largely converted to H_2SO_4. It appears that this concentrated sulfuric acid is condensing in the heat exchanger, leading to the high corrosion rates experienced. Figure 4-18 contains an equilibrium diagram for sulfuric acid.

This condensation mechanism results in the deposition of very high concentration sulfuric acid directly on the surface of the SS piping. From the $DeSNO_x$ column observations on metal corrosion, the most corrosion was seen where the flue gas entered the column below the supported packing. As the flue gas started contacting the circulating water, the amount of observable corrosion quickly diminished. Because this region of sulfuric acid condensation before any moisture condensation will exist in the $DeSNO_x$ process, it appears that more exotic alloys may have to be deployed in this condensation area. Materials of construction that may have to be considered for the back end of the recuperator and around the inlet of the water column include Alloy 20, Inconel 825, Inconel 686, and HASTELLOY® C-276. These materials appear to have much better tolerance for concentrated sulfuric acid than more conventional SS; however, some literature suggests even these materials may have operating conditions where the corrosion rates may not be acceptable. The ability to control this corrosion mechanism is likely to drive the decision on whether postcombustion $DeSNO_x$ column desulfurization or conventional precombustion desulfurization is utilized. Obtaining more information on the performance of these alloy materials under the high-concentration sulfuric acid condensation conditions experienced in $DeSNO_x$ column testing will be emphasized in the dynamic corrosion testing and any future $DeSNO_x$ column testing utilizing the EFG. More details on the specific failures follow.

Figure 4-19 shows a corroded carbon steel pipe fitting on the $DeSNO_x$ water circulation line. The water leak detected developed a hole early, necessitating shutdown of the back-end systems for repair. It is interesting to note that the corrosion appeared to follow the heat-affected zone of the weld (see Figure 4-19). This corrosion was most likely incurred during the first two campaigns but ended up manifesting itself at the beginning of the third campaign. The installation of the carbon steel pipe fitting was original to the building of the skid approximately 10 years ago.

A corroded 316/316L SS compression fitting caused a leak, requiring the combustor and $DeSNO_x$ system to be isolated and depressurized for repairs. This fitting was located downstream from the $DeSNO_x$ column. A corrosion pinhole in the 316/31L SS heat exchanger between the combustor and the $DeSNO_x$ system required another isolation and depressurization for repairs (see Figure 4-20). This leak was very substantial, and because it was venting outside with the heat

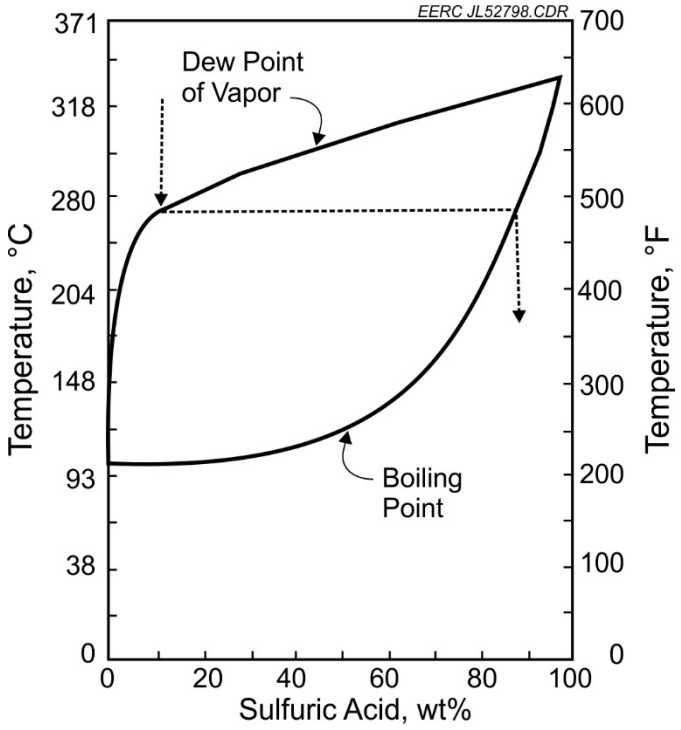

Figure 4-18. Equilibrium diagram for sulfuric acid.

exchanger's cooling air, it went undetected for an extended period of time. Prior to repair, the entire system was losing a large amount of flue gas, but the leak was detected only after personnel detected the flue gas near the vent exit point outside the building. It should be noted that the corrosion occurred at the same location as where cold air was introduced into the outer jacket of the annular heat exchanger. It was surmised that H_2SO_4 was condensing at that spot, resulting in the extreme corrosion of the interior of the tube. There is also evidence of corrosion on the outside of the tube, most likely occurring after the internal corrosion created the pinhole and flue gas began flowing through it. This pinhole is probably the most convincing evidence that cool condensation points must be avoided to prevent localized acid condensation and corrosion.

Table 4-16 shows the corrosion failure event log for the $DeSNO_x$ tests.

Table 4-16. Failure Time Log Event and Description

Event Date and Time	Event Remarks
7/25, 5:53	Leaky tube fitting detected on the quench pot
7/25, 23:24	Leaky water recirculation pipe on the $DeSNO_x$ column skid
7/26 13:28	Loss of recycle gas booster pressure
7/27, 2:28	Leak at the column back end (on the FT skid near recycle gas booster)
7/27, 19:43	Leak in column inlet gas tube-in-tube heat exchanger cooling section
7/29, 7:42	Leak at the inlet to $DeSNO_x$ column

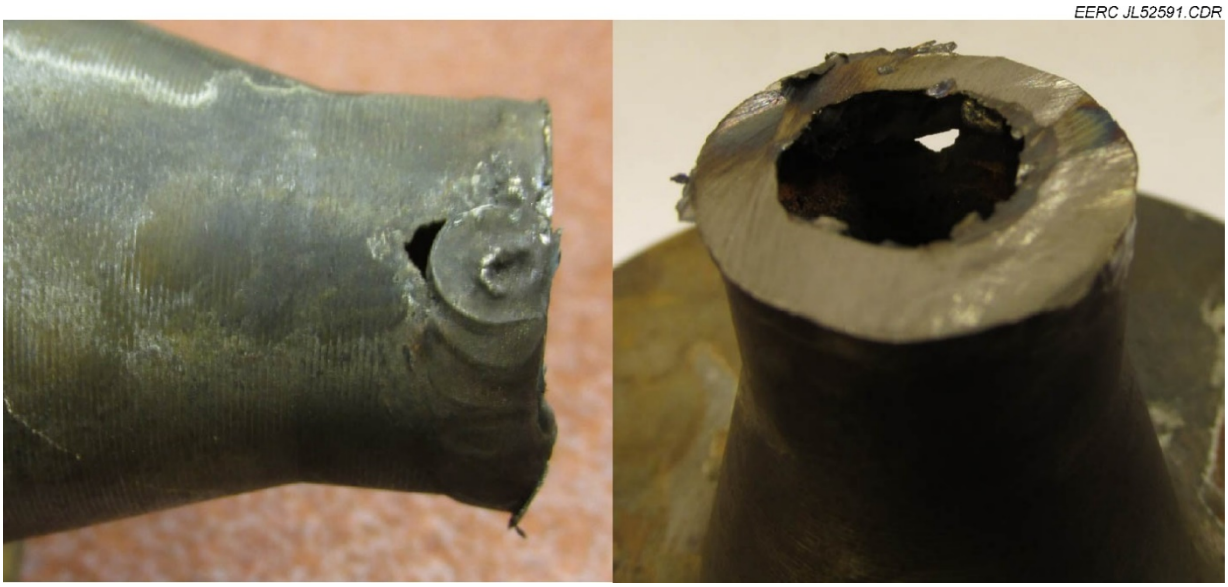

Figure 4-19. Corrosion of carbon steel flange.

Figure 4-21 shows a sectioned piece of 316/316L SS tubing with significant internal deposits. This piece of tubing was located in the water recirculation loop between the column's sump and the water recirculation pump (approximately room temperature). Other deposits in the DeSNO$_x$ water loop had impacted water removal valves during all 3 weeks of testing. On the final day of testing, the 316/316L SS compression fitting at the entrance to the DeSNO$_x$ system started leaking. This resulted in the combustor and DeSNO$_x$ system being shut down about 4 hours early. The gasifier was kept operational to furnish syngas to the HMTS and complete the membrane-testing component of the campaign.

4.15 Conclusions

The 3-week test regime reinforced the team's understanding of the operation and performance of an integrated flue gas production and gas impurities removal process, or DeSNO$_x$ process. Postshakedown tests were targeted at understanding single- and two-stage coal-to-clean flue gas conversion processes with the DeSNO$_x$ scrubber operating as a nitrogen and sulfur species removal system. The following are the primary outcomes of the experimental efforts.

Figure 4-20. Air-cooled heat exchanger corrosion and pinhole (interior and exterior).

Figure 4-21. Internal deposit formation in water recirculation tubing.

4.15.1 Single-Stage Process

- FBG operation in 468-psig oxy-coal (Freedom Mine coal) combustion mode during Test FBG-044 produced flue gas without any agglomeration-related shutdown, which was experienced during an earlier shakedown test (FBG-042) with Falkirk North Dakota lignite because of higher sodium content in the coal.

- Limestone addition to coal caused about 90% sulfur capture in the (solid residue) bed, resulting in low sulfur loading in the gas. A decision was made to avoid limestone addition to the test column at simulated field conditions with higher sulfur loading in the flue gas.

- With a constant water circulation rate of 27.5 L/hr (7.3 gal/hr) and a zero freshwater injection rate, water pH was reduced to a low value of 1.62. Freshwater injection and equivalent acidic

water discharge led to an increase in pH to up to 3.0. This observation led to defining a consistent water injection/discharge strategy for the future tests.

- NO and NO_2 retention exceeded 90% and 80% (on a weight basis), respectively, while N_2O retention was negative, indicating its formation in the scrubber section.

- The NO–SO_2–H_2O mixture at equilibrium conditions revealed the strong impact of pressure and temperature on the formation of N_2O. The study revealed a marked increase in N_2O concentration as the mixture temperature exceeded 110°F.

- The average gas temperature at the column inlet and outlet was 320° and 95°F, respectively.

- The column-specific internal temperature variation in relation to N_2O formation must be further investigated.

- Because of the low sulfur concentration in the flue gas, high S retention was observed. Trends were not conclusively established during this test.

4.15.2 Two-Stage Process

1. Except for one gasifier shutdown due to a gasifier-plugging issue, syngas production was successfully maintained throughout the test, achieving a total of 70 hr of steady-state operation.

2. Column performance was disrupted about four times because of corrosion-related gas and column circulation water leakage.

3. Inlet gas temperature significantly varied (unlike earlier test). Outlet gas temperature was also impacted because of inlet gas fluctuations, unlike in the earlier test.

4. Freshwater injection, acidic water discharge, and column water recirculation rates were maintained constant during column operation. At 112 L/hr, the recirculation rate was four times higher than the earlier test.

5. pH = 1.57 was an average value observed during the entire test, except for a slight increase in the value during the last 6 hr, owing to a reduced gas flow rate.

6. The wet flue gas injection rate in the column ranged between 655 and 870 scfh, which is about an order of magnitude higher than the earlier test.

7. The NO concentration in the flue gas was low owing to the low nitrogen concentration in the EFG combustion feed stream.

8. Greater than 77% nitrogen capture was achieved. NO_2 and N_2O remained undetected.

9. Total S species loading was 3 orders of magnitude higher compared to the previous test. This high value was an effect of discontinued use of limestone with coal feed.

10. Measurement of sulfur species concentration at the inlet and outlet of the $DeSNO_x$ column revealed capture of the primary sulfur species SO_2 at more than 90%. COS and H_2SO_4 were captured at nearly 100%. The SO_2 concentration in the inlet flue gas stream ranged between 600 and 800 ppm.

11. At steady gasifier operating conditions, the increase in excess oxygen in the syngas combustion was found to have a decreasing effect on SO_2 concentration at the column inlet. SO_2 oxidation to form SO_3 with an increase in oxygen concentration was one of the plausible explanations for the observed phenomenon.

12. High-pressure operating conditions related to moisture dew point increase in the upstream flue gas stream coupled with a high SO_2 concentration could pose an operating concern owing to acid corrosion of the flue gas supply line to the spray column.

4.15.3 Commercial Impact

The commercial impact of a viable postcombustion impurity removal system is significant. While many precombustion technologies exist, they have a large energy penalty associated with operations. To date, no major barriers have been encountered with postcombustion impurity removal processes such as $DeSNO_x$. Future efforts in this area will concentrate on integrating precombustion and postcombustion impurity removal while minimizing corrosion impacts.

5.0 ACTIVITY 5 – DEVELOPMENT OF IMPROVED CARBON CAPTURE SYSTEMS ENGINEERING MODELS

The modeling efforts for Activity 5 focused on three key areas that supported the efforts and testing that occurred in Activities 2–4. The EERC used the results of each activity to develop improved systems engineering models, and in the case of Activities 2 and 3, developed a technoeconomic assessment of the technologies. For Activity 4, the EERC developed baseline pilot-scale models to assist in the development of the technology.

5.1 Cost and Performance of RPB Systems

The performance of a RPB system was tested at the EERC under a parallel project effort, and the results of the testing were used to develop a technoeconomic assessment of the technology in a full-scale 550-MW power system. A RPB system is used to improve the mass transfer characteristics between the solvent and the gas and is potentially able to reduce the physical footprint of the absorber system. In addition, this technology is considered modular and can be used to test a slipstream of the gas and then scaled up by adding more modules. The solvent tested in the RPB was provided by CO_2 Solutions and is an enzymatic solvent capable of being regenerated at low temperature; therefore, low-grade or waste heat may be able to be used for regeneration.

In order to understand the overall economic implications of adding RPB technology, the EERC performed a full-scale economic assessment of the technology, based on Case 12 in the DOE report "Cost and Performance Baseline for Fossil Energy Plants, Volume 1: Bituminous Coal and Natural Gas to Electricity, Revision 2a" (41). This baseline was chosen because previous evaluations of the CO_2 Solutions solvent were performed with this baseline (1). Additionally, the physical performance of the solvent is similar to MEA, with the primary benefit of the solvent being low-temperature regeneration. Therefore, the applicability of the Shell Cansolv baseline (or Case B12B) to this system is questionable. The overall energy balance calculated previously for the CO_2 Solutions solvent is shown in Table 5-1. The assessment was completed assuming that the solvent can be generated with waste heat, and that the absorption/stripping performance matches MEA. As can be seen by the data, the solvent alone represents a significant increase in overall plant efficiency because of the utilization of waste heat.

Testing at the EERC indicated that the performance of the CO_2 Solutions solvent in the RPB was very similar to the performance in a standard packed tower; therefore, the overall mass and energy balance was assumed to be the same as in the previous report. The only difference between the assessments was the capital cost estimate used for the absorber and strippers. Data on the cost and performance of the system were provided by Trilok Fabrication and Equipment LTD. and are shown in Table 5-2. The data provided represent very high level estimates and are not based on detailed engineering. The power consumption estimates for the motors are very similar to the power consumption of the pumps in the traditional system, and given the high-level nature of the estimates, it was assumed that the auxiliary power requirements for the RPB system were the same as a standard absorber/stripper tower. This assumption has merit, because the motor energy consumption is offset by not having to pump the solvent to the top of the absorber and stripper columns.

This information was used in conjunction with previous technoeconomic assessments for the CO_2 Solutions solvents to develop a cost estimate for the CO_2 removal system. Since a detailed engineering design was not completed for the RPB, it was assumed that the standard auxiliary needs, including reboilers, heat exchangers, and condensers, were the same as the base case. The economic assessment was completed using Aspen Process Economic Analyzer (APEA). The equipment costs provided were input into the model to determine the direct field costs, indirect field costs, non-field costs, and project total costs. The overall cost for an absorber/stripper system using six absorbers and four strippers was estimated to be US$185.5 million. Adding in compression, the total cost for CO_2 removal and compression is US$232.0 million. These estimates were then used to determine the overall cost of CO_2 capture in dollars per ton for a 550-MW system.

As mentioned, this assessment is based on previous work performed in providing an economic assessment of the CO_2 Solutions technology. The NETL baseline report was referenced to estimate the costs for the majority of the power plant. The cost estimates in the report had a base year of 2007. Case 11, supercritical pc power plant without CO_2 capture, and Case 12, supercritical pc power plant with Econamine-based CO_2 capture, were used as a baseline for comparison. These case studies use Illinois No. 6 bituminous coal as the fuel. Under this process, the assumption is made that the plant being assessed is a greenfield plant with a net power output of 550 MW_e.

Table 5-1. Energy Balance for CO_2 Solutions Solvent

	Case 11	Case 12	CSES[1]
Steam Turbine Power	**580,400**	**662,800**	**636,714**
Coal Handling and Conveying, kWe	440	510	458
Pulverizers, kWe	2780	3850	3052
Sorbent Handling and Reagent Preparation, kWe	890	1250	982
Ash Handling, kWe	530	740	583
Primary Air Fans, kWe	1300	1800	1427
Forced Draft Fans, kWe	1660	2300	1823
Induced Draft Fans, kWe	7050	11,120	8085
Selective catalytic reduction, kWe	50	70	55
Baghouse, kWe	70	100	78
Wet flue gas desulfurization, kWe	2970	4110	3260
CSES Auxiliaries, kWe	–	20,600	16,356
CO_2 Compression, kWe	–	44,890	35,643
Miscellaneous Balance of Plant, kWe	2000	2000	2000
Steam Turbine Auxiliaries, kWe	400	400	400
Condensate Pumps, kWe	800	560	739
Circulating Water Pump, kWe	4730	10,100	6095
Groundwater Pumps, kWe	480	910	589
Cooling Tower Fans, kWe	2440	5230	3149
Transformer Losses, kWe	1820	2290	1939
Total Auxiliaries, kWe	**30,410**	**112,830**	**86,713**
Net Power, kWe	**549,990**	**549,970**	**550,001**
Net Plant Efficiency, HHV	39.3%	28.4%	35.8%
Net Plant Heat Rate, Btu/kWh	8687	12,002	9529
Condenser Cooling Duty, 10^6 Btu/hr	2178	1646	2434
Consumables			
As-Received Coal Feed, kg/hr (lb/hr)	185,759 (409,528)	256,652 (565,820)	203,782 (449,263)
Limestone Sorbent Feed, kg/hr (lb/hr)	18,437 (40,646)	25,966 (57,245)	20,351 (44,866)
Thermal Input, kWt	1,400,163	1,934,520	1,536,015
Raw Water Withdrawal, m^3/min (gpm)	20.1 (5321)	38.1 (10,071)	24.7 (6529)
Raw Water Consumption, m^3/min (gpm)	16.0 (4227)	29.3 (7733)	19.4 (5118)

[1] CO_2 Solutions enzymatic solvent.

Table 5-2. RPB Performance Data

Unit Flue Gas Capacity	100 m^3/s
Number of Absorbers	6
Number of Strippers	4
Radius of Solvent Inlet Pipe	0.15 m
Inner Radius of Packing (based on gas velocity 40 m/s in the eye)	0.9 m
Outer Radius of Packing	1.4 m
Height of Rotor	4 m
Motor rpm	200
Motor Rating	1000 hp
Equipment Cost per RPB	US$2.2 million

For the solvent, APEA was used to estimate the capital and operating costs for the capture portion of the plant. Values for cost were adjusted from values given for Case 12 by utilizing information from Aspen modeling and derived adjustment factors as described in the NETL document "Capital Cost Scaling Methodology" (42). The methodology provides a system to modify costs from a base case utilizing parameters that directly affect those costs.

Case 12 is used for the economic portion of the assessment as it contains the equipment necessary to conduct CO_2 capture from the greenfield plant. The only modification is that the assumption is made that the steam cycle of the plant will not be touched.

To estimate COE, a simplified equation that was a function of total overnight capital (TOC), fixed and variable operating and maintenance (O&M) costs, capacity factor, and net output was given by the NETL report (43).

$$COE = \frac{\begin{matrix} first\text{-}year \\ capital\ charge \end{matrix} + \begin{matrix} first\text{-}year \\ fixed\ operating \\ costs \end{matrix} + \begin{matrix} first\text{-}year \\ variable\ operating \\ costs \end{matrix}}{\begin{matrix} annual\ net\ megawatt\ hours \\ of\ power\ generated \end{matrix}} \quad \text{[Eq. 5]}$$

$$COE = \frac{(CCF)(TOC) + OC_{FIX} + (CF)(OC_{VAR})}{(CF)(MWH)} \quad \text{[Eq. 6]}$$

where:

COE = Revenue received by the generator (US$/MWh) during the power plant's first year of operation (expressed in base-year dollars)

CCF = Capital charge factor

TOC = Expressed in base-year dollars

OC_{FIX} = The sum of all fixed annual operating costs

OCVAR = The sum of all variable annual operating costs, including fuel at 100% capacity factor

CF = Plant capacity factor (85%)

MWh = Annual net megawatt-hours of power generated at 100% capacity factor

Cost estimates were provided for each section of the power plant and categorized by account code (Table 5-3). Details for the major equipment in each account can be referenced in the NETL report. DOE scaling factors are applied to the account numbers based on parameter outputs given in the Aspen model. For example, Account 1 factors are based on the coal feed rate of the plant whereas Account 3 factors are based on parameters such as raw water makeup and water load to treatment. Account 9 factors are adjusted based on circulating water flow rate and cooling tower duty. Details for every account can be found in the NETL report.

Table 5-3. Plant Sections by Account Number

Account No.	Section Description
1	Coal and sorbent handling
2	Coal and sorbent preparation and feed
3	Feedwater and miscellaneous systems and equipment
4	Boiler and accessories
5	Flue gas cleanup
5B	CO_2 recovery
6	Combustion turbine/accessories
7	HRSG, ducting, and stack
8	Steam turbine generator and auxiliaries
9	Cooling water system
10	Ash/spent sorbent recovery and handling
11	Accessory electric plant
12	Instrumentation and control
13	Improvement to site
14	Building structures

It is recognized that there are components of the carbon capture system that truly do not apply to the CO_2 Solutions capture system. These are components that are not needed for the CO_2 Solutions solvent but are in the Econamine basis for the DOE case studies. These systems include the water wash tower and associated subsystems and the solvent reclaimer and associated subsystems. Exact detail on the precise components cannot be derived as that information is held as proprietary by Fluor and cannot be released by DOE. Nonetheless, an attempt was made to remove those components from the system and the costs estimated by their removal from the case study.

The cost-estimating methodology described was used to calculate the total plant capital costs, CO_2 Solutions RPB, and was compared to Case 12 and the initial evaluation conducted previously, denoted as CO_2 Solutions Base (1). Table 5-4 shows the total plant cost (TPC) results, organized by cost account. Further results of the economic evaluation are given in Table 5-5.

The projection of utilizing RPBs instead of traditional columns with the CO_2 Solutions solvent greatly reduces the CO_2 capture costs. This economic exercise is only to demonstrate the potential of the RBP technology; however, there are several things to note, including the following:

- The modular aspect of RPBs must be vetted further.
- Additional testing is required in scale-up demonstrations to truly evaluate the potential for RPBs and to eliminate any unforeseen challenges with their use.
- The evaluation relies on the ability to find enough waste heat sources to provide the heat for solvent regeneration.
- More vetting of the RPB costs must be conducted.

Table 5-4. TPC Results for Each Case Organized by Account Code, costs in US$1000 (2007 $)

Account No.	Description	Case 12	CO_2 Solutions Base	CO_2 Solutions RPB
1	Coal and sorbent handling	47,015	40,633	40,633
2	Coal and sorbent preparation and feed	22,441	19,198	19,198
3	Feedwater and miscellaneous systems and equipment	102,552	92,134	92,134
4	Boiler and accessories	369,144	315,868	315,868
5	Flue gas cleanup	163,337	137,425	137,425
5B	CO_2 recovery	468,782	384,476	231,992
6	Combustion turbine/accessories	0	0	0
7	HRSG, ducting, and stack	37,525	38,168	38,168
8	Steam turbine generator and auxiliaries	132,111	122,543	122,543
9	Cooling water system	60,964	43,366	43,366
10	Ash/spent sorbent recovery and handling	15,109	13,257	13,257
11	Accessory electric plant	80,932	58,835	58,835
12	Instrumentation and control	25,838	22,356	22,356
13	Improvements to site	15,717	15,517	15,017
14	Buildings and structures	60,557	58,581	57,735
TPC		1,602,024	1,362,358	1,208,581
TOC		1,963,646	1,667,685	1,482,893

Table 5-5. Estimated Costs for Case 12, CO_2 Solutions Base, and CO_2 Solutions Using a RPB

	Case 12	CO_2 Solutions Base	CO_2 Solutions RPB
TPC, US$ (2007)/kW	2913	2477	2197
TOC, US$ (2007)/kW	3570	3032	2696
Total As-Spent Capital, US$ (2007)/kW	4070	3457	3074
COE, US$ (2007)/MWh	100.9	82.3	76.8
Levelized COE, US$ (2007)/MWh	127.8	104.4	97.4
CO_2 Capture Cost, US$ (2007)/tonne	47.7	39.3	30.2

5.2 Updated Existing Precombustion Model

Previous EERC technoeconomic studies for IGCC systems included the systems necessary to evaluate the impact of the new technology on the overall system. As part of this activity, the EERC evaluated the potential use of a complete IGCC model that represents Case B5B of the DOE baseline study Revision 3 (44). The model was developed by Field and Brasington (Massachusetts Institute of Technology [MIT] model) and is intended to represent the GE radiant cooler gasification system, with CO_2 capture and compression presented in Case 2 (45). Utilization of this baseline model with novel CO_2 separation and capture technologies is expected to provide increased accuracy in technoeconomic assessments. This subactivity presents the IGCC plant performance study as a comparison between the baseline and EERC model.

5.2.1 Process Results and Discussion

A high-level IGCC process flow sheet depicting comparative differences between baseline Case B5B and the EERC model is shown in Figure 5-1a and b, respectively. The figure depicts the unit operations and main flow streams integrating each unit operation for these models. The detailed description of the baseline model Case B5B and IGCC performance data is provided in the DOE baseline study (44). The description of the MIT model used in predicting the baseline data for the Case B5B is presented in the MIT study (45). The primary difference between the MIT model representing the baseline IGCC process and the EERC model is the substitution of SELEXOL with a H_2 separation membrane. To accommodate this change, the CO_2 gas compression and CO_2 liquid-pumping processes are replaced with cryogenic CO_2 separation and liquid CO_2-pumping processes. Also, as shown in Figure 5-1b, the water-scrubbing and shift gas-cooling processes of the baseline model are removed in the EERC model. This change is based on the following considerations: 1) the operating temperature of the gasifier in excess of 1300°C is adequate for greatly reducing tar concentration in the syngas, thus reducing the need for scrubbing, and 2) the operating temperature range of the H_2 membrane closely matches with the shift gas exit temperature such that gas cooling is not essential in the EERC process.

The two-stage membrane process generates a H_2-rich stream, with N_2 used as H_2 sweep or carrier of fluid injected in the membrane process of staged separation. This process separates greater than 99% H_2 by weight of the inlet stream. The compressed sweep N_2 is received from the ASU process. Two of the three outlet streams consisting of permeate (H_2) are directly injected into the gas turbine power module while the retentate or the CO_2-rich gas stream is injected into the cryogenic section, as depicted in Figure 5-1b. The product CO_2 liquid is pumped for pipeline transport to high pressure (in excess of 150 bar) such that additional pressure boosting prior to the delivery terminal is avoided.

The power generation module in the baseline and in the EERC process model consists of a syngas expander and gas and steam turbines. The primary difference between the baseline and EERC model is that the clean H_2-rich gas stream diluted with sweep N_2 used in the membrane process along with the recycle gas stream from the cryogenic CO_2 separation process module is injected into the gas turbine module, and the mixed stream of feed gases is converted to power. The steam turbine process module receives hot gases from the gas turbine section. Modifications for process optimization to this process was not required. The parasitic or auxiliary load for the operation of the IGCC process is provided by this section.

Unlike the baseline process in which a significant fraction of the sulfur and halogen species are removed in the scrubbing and cooling processes, the proposed EERC model is designed for capture in the sorbent bed with high selectivity for trace gas removal downstream of the shift reactor module. The gas-phase release of the sulfur and halogen species during the sorbent bed regeneration process is recovered in the Claus process, having an established performance. For simplicity, the EERC process assumes the parasitic/auxiliary load required by the Clause process as determined in the baseline process for establishing EERC process performance and does not attempt to repeat modeling.

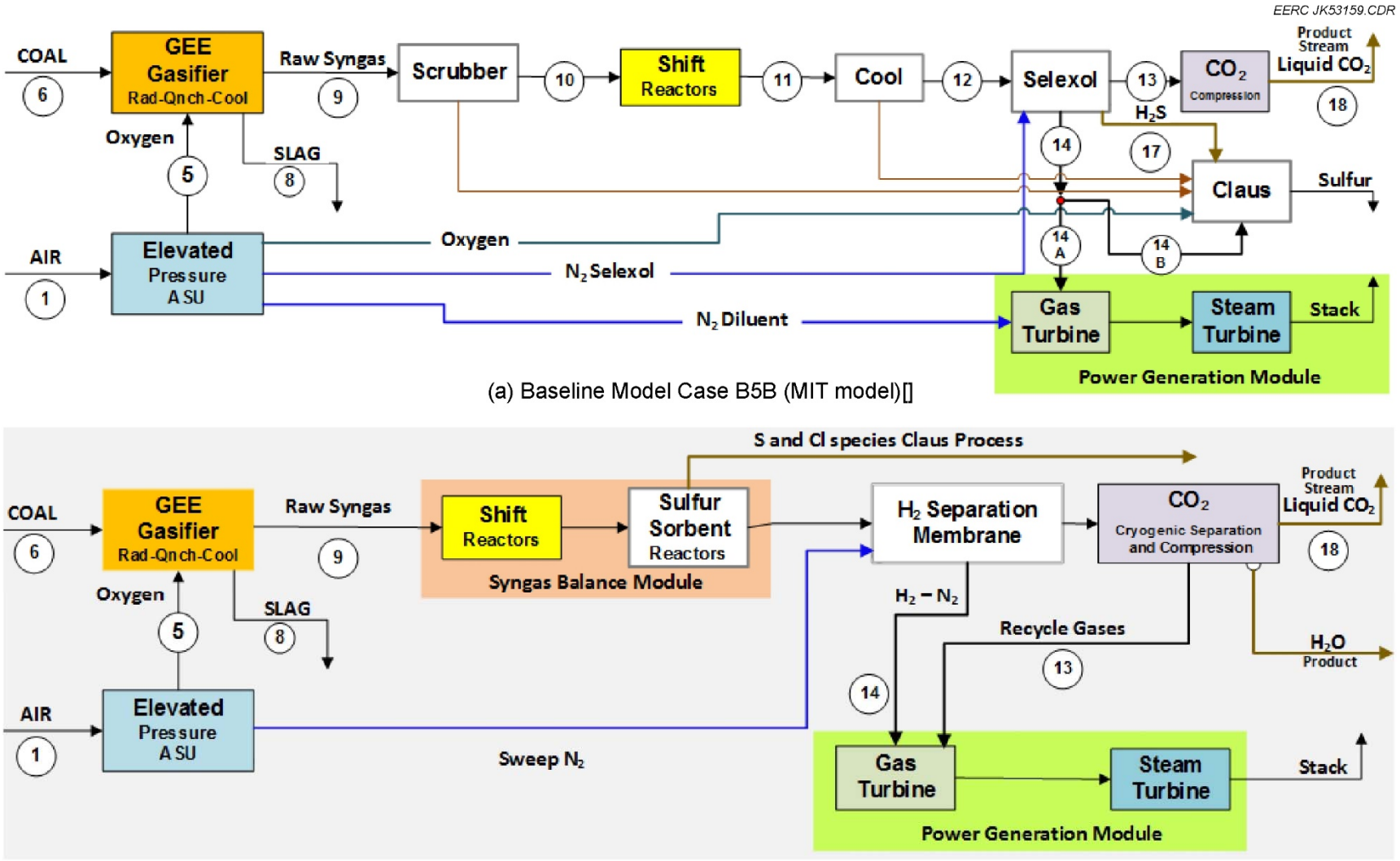

Figure 5-1. High-level IGCC process flow sheet depicting comparative differences between Baseline Case B5B and EERC model.

To validate the computed baseline stream data, the published data for Case B5B are represented in the first column of the data table showing the performance. The following data tables showing the process performance data consist of three columns: a) data presented in Case B5B of the DOE NETL report, b) computed baseline data with MIT model including SELEXOL-based CO_2 capture, and c) computed data with the EERC model, including H_2 separation membrane and cryogenic CO_2 separation.

The Case B5B IGCC process is based on the General Electric Energy (GEE) gasifier. The current modeling effort is based on the GE radiant quench cooling process.

The composition of the bituminous coal used in the computation is shown in the Table 5-6. Except for coal moisture, ultimate and proximate analysis are on a dry basis. The mercury content of Illinois No. 6 coal considered in the modeling is 0.09 ppm on a dry weight basis.

Table 5-6. Composition of the Design Coal – Illinois No. 6 Bituminous

Proximate, wt%	**(a)**	**(b)**	**(c)**
Moisture, as received	11.12	11.12	11.12
Fixed Carbon	49.72	49.72	49.72
Volatile Matter	39.37	39.37	39.37
Ash	10.91	10.91	10.91
Ultimate, wt%			
Ash	10.91	10.91	10.91
Carbon	71.72	71.72	71.72
Hydrogen	5.06	5.06	5.06
Nitrogen	1.41	1.41	1.41
Chlorine	0.33	0.33	0.33
Sulfur	2.82	2.82	2.82
Oxygen	7.75	7.75	7.75

Table 5-7 shows various throughputs to the gasifier (coal, oxygen, and water/slurry) for the three cases. The data in Columns a and b are the baseline cases and the data in Column c represents the feed data for EERC model. As illustrated, the closely matching feed throughput and composition values indicate the identical performance of the gasifier in the three cases and thus form a common comparison basis for the targeted study.

Table 5-8 shows the composition, flow rate, temperature, pressure, and related properties of the raw syngas leaving the gasifier downstream cooling system and shifted gas leaving the WGS process module. The syngas pressure in all three cases is identical (5.5–5.6 MPa); however, because of differences in the extent of cooling at the gasifier downstream, the syngas temperature is different. In Case B5B (Column a), the syngas is cooled down to 677°C in the radiant cooling section. The resulting moisture fraction in the syngas is 13.8%. While in the computed baseline

Table 5-7. Coal, Oxygen, and Slurry Water Throughputs to the Coal Gasification Process in the Three Models

	Coal Feed			Oxygen Feed			Slurry Water Feed		
Mole Fraction	(a)	(b)	(c)	(a)	(b)	(c)	(a)	(b)	(c)
H_2O	–	–	–	0.0178	0.0188	0.0188	1.0	1	1
N_2	–	–	–	0.0318	0.0322	0.0322	0	0	0
NH_3	–	–	–	0.00	0	0.00	0	0	0
O_2	–	–	–	0.95	0.95	0.95	0	0	0
Flow Rate, kmole/hr	–	–	–	5,526	5,739	5,739	5,037	5,037	5,037
Flow Rate, kg/hr	–	–	–	177,826	184,696	184,696	90,747	90,747	90,747
Solids Flow Rate, kg/hr	220,902	220,902	220,902	–	–	–	–	–	–
Temperature, °C	15	60	60	32	91	91	142	60	60
Pressure, MPa, abs	0	7	7	1	7	7	5.79	6.0	6.0
Aspen Plus Enthalpy, kJ/kg	−2117	−2046	−2046	4	47	47	−15427	−15799	−15799
Density, kg/m^3	–	–	–	11	72	72	872	829	829
Molecular Weight	–	–	–	32	32	32	18	18	18

Table 5-8. Composition, Flow Rate, Temperature, Pressure, and Related Properties of the Raw Syngas and Shift Gas

	Raw Syngas			Shift Gas		
Mole Frac	**(a)**	**(b)**	**(c)**	**(a)**	**(b)**	**(c)**
SELEXOL		0.0000	0.0000		0.0000	0.0000
CO	0.3576	0.2686	0.3120	0.0060	0.0082	0.0118
CO_2	0.138	0.0725	0.0842	0.3082	0.3026	0.3006
H_2	0.3406	0.2030	0.2357	0.4366	0.4212	0.4196
H_2O	0.1369	0.4385	0.3478	0.2325	0.2526	0.2573
N_2	0.007	0.0061	0.0071	0.0044	0.0056	0.0056
AR	0.0086	0.0055	0.0064	0.0054	0.0050	0.0050
CH_4	0.0011	0.0001	0.0001	0.0007	0.0001	0.0001
NH_3	0.0019	0.0000	0.0000	0.0013	0.0000	0.0000
H_2S	0.0073	0.0048	0.0056	0.0047	0.0047	0.0000
COS	0.0002	0.0003	0.0003	0.0000	0.0000	0.0000
HCl	0.0008	0.0005	0.0006	0.0001	0.0000	0.0000
Flow Rate, kmole/hr	23,122	33,640	28,964	36,477	36,935	36,773
Flow Rate, kg/hr	465,238	660,000	575,753	705,563	718,969	713,315
Solids Flow Rate, kg/hr	–	–	–	–	–	–
Temperature, °C	677	216	404	240	150	150
Pressure, MPa, abs	5.6	5.5	5.5	5.4	5.43	5.43
AspenPlus Enthalpy, kJ/kg*	−5,246	−5,353	−4,051	−8,864	−9,449	−9,525
Density, kg/m^3	14	28.0	19.5	24.8	36.6	36.7
Molecular Weight	20.1	19.6	19.9	19.3	19.5	19.4

* 77°F and 14.696 psi.

case, the raw syngas is cooled down to 216°C (Column b) in the radiant quench cooling process typically available in the GEE gasifier. The cooling in the case of the EERC model (Column c) is restricted to about 404°C, achieved by reducing the quench water flow rate as compared to the baseline computed value. The elevated moisture fraction in the coolest raw syngas (Column b) is higher because of quench cooling. The mole fraction of the syngas species is different because of moisture dilution. Considering that the operating temperature of the gasifier, being in excess of 1300°C, is adequate for significantly reducing tar concentration in the syngas, raw syngas water scrubbing is not required in the EERC process. The raw syngas is filtered (in-line candle gas filter) and directly injected into the shift process module (see Figure 5-1b). The steam injection rate in the EERC process is reduced, while in the baseline case, the syngas moisture is condensed in the scrubber and then added back in the shift process. The steam usage is thus reduced in the EERC process. As can be observed, the shift gas composition is identical for all cases except the for marginally higher unshifted residual fraction of carbon monoxide (0.8% in baseline vs. 1.2% in the EERC process).

The H_2 membrane operates at the same temperature and pressure as the WGS reactor; therefore, the thermodynamic losses associated with cooling and/or pressure changes are avoided. The H_2 in the shift gas is passed selectively through the membrane, resulting in a high-pressure stream of CO_2, water, and other nonpermeate or raffinate gas stream on one side and a highly purified H_2 stream on the other. The steam or N_2 can be used as sweep gas, depending on the application or purity of the H_2 required. Since the gas turbine in the power generation module accepts N_2 diluent in the H_2 feed, N_2 produced from the ASU is used as the sweep gas.

The membrane separation process uses inorganic dense membranes fabricated from palladium alloys, solid electrolytes such as zirconia and nickel, or microporous ceramic membranes. The choice of dense metallic membranes is owing to its high selectivity for H_2 permeation, achieving flux rates suitable for large-scale commercial applications. It is assumed that the H_2 membrane technology is near-commercial maturity and is sufficiently inert to H_2S and CO poisoning effects and maintains structural integrity during sustained operation.

Table 5-9 shows the composition, flow rate, temperature, pressure and related properties of the inlet and various outlet streams across the H_2 membrane. As illustrated in the table, the temperature and pressure at the membrane inlet is same as at the WGS outlet (see Table 5-8). The shifted gas cooling necessary for acid gas removal in the SELEXOL process is not essential in the membrane process. The gas-cooling process is removed in the EERC model. The sweep gas (N_2) obtained from the different ASU streams is injected on the permeate side of the two-stage membrane. The sweep gas composition, pressure, and temperature determine the pressure and temperature of the combined H_2-rich streams leaving the membrane. In the current IGCC model, the gas turbine fuel injection pressure determines the membrane back pressure set point and the corresponding sweep gas pressure. The sweep N_2 is compressed in the ASU unit. Within the permissible flammability limits of the permeate H_2 stream, the oxygen impurities in the sweep N_2, along with other impurities such as argon and trace noble gases, could be allowed, thus minimizing the need for pure nitrogen. Table 5-9 also shows the H_2- and CO_2-rich stream composition, flow rates, pressure, and temperature of the membrane outlet. The two H_2-rich streams are combined

Table 5-9. Composition, Flow Rate, Temperature, Pressure, and Related Properties of the Inlet and Various Outlet Streams

	Membrane Inlet Stream			Membrane Outlet Stream		
Mole Fraction	**Shifted Gas**	**N_2 Sweep 1**	**N_2 Sweep 2**	**H_2-Rich Stream 1**	**H_2-Rich Stream 2**	**Raffinate CO-Rich Stream 3**
CO	0.0118	0.0000	0.0000	0.0000	0.0000	0.0190
CO_2	0.3006	0.0000	0.0000	0.0000	0.0000	0.4850
H_2	0.4196	0.0000	0.0000	0.4150	0.4150	0.0636
H_2O	0.2573	0.0000	0.0000	0.0000	0.0000	0.4151
N_2	0.0056	0.9860	1.0000	0.5769	0.5850	0.0090
AR	0.0050	0.0045	0.0000	0.0026	0.0000	0.0081
CH_4	0.0001	0.0000	0.0000	0.0000	0.0000	0.0002
O_2	0.0000	0.0095	0.0000	0.0055	0.0000	0.0000
Total Flow, kmol/hr	36,773	9730	9981	16,631	17,062	22,790
Total Flow, kg/hr	713,315	273,463	279,599	287,375	293,874	685,128
Temperature, °C	150	196	30	195	95	149
Pressure, MPa	5.43	3.17	3.17	3.10	3.10	5.10
Enthalpy, kJ/kg	−9525	176	−3	287	117	−10,071
Density, g/cm^3	36.7	22.6	35.4	13.8	17.5	70.8
Average, MW	19.4	28.1	28.0	17.3	17.2	30.1

with combustible recycle gases before injection in the gas turbine. The CO_2 rich stream is injected into the cryogenic CO_2 separation system. Table 5-10 shows flow rates of the combined H_2-rich stream. As depicted, about 91% of the H_2 in the feed is shown as recoverable in the membrane. With membrane performance optimization, the H_2 recovery could be improved. However, the drivers for such recovery are dependent on the impact of H_2 in the raffinate, cryogenic recovery of the CO_2 in the subsequent section, and justifiable improvements in the overall system's thermodynamic efficiency.

The essential components of the process are the two-stage cooling and the CO_2 separation and liquid CO_2 pumping for long distance transport as a supercritical fluid. First-stage cooling reduces the CO_2-rich stream received from the membrane section to room temperature (about 20°C), essential for removing moisture as condensate from the flash tank. The gas pressure is not reduced within in any unit operation of this module except for the system pressure losses. The relatively dry gas is further cooled to about −55°C (the point above the CO_2 triple point at the operating pressure) for selective recovery of CO_2 as a liquid. The liquid CO_2 is pumped to above 15.17 MPa and reheated to about 50°C before transporting it as a supercritical fluid.

Table 5-11 shows the species-level mass flow rate of the inlet–outlet streams of the cryogenic CO_2 separation module. The molar composition of the CO_2-rich stream injected into the CO_2 separation module is also shown in Table 5-11. Stage 1 cooling recovers about 99.9% water from the wet stream. The residual water can also be removed by freeze-drying in the Stage 2 low-temperature cooling system. The heat from the incoming dry CO_2 reach stream is extracted in an indirect-contact cross-flow heat exchanger located between the Stage 2 cooling inlet and CO_2 liquid pump. As shown in the Table 5-11, 10 wt% CO_2 and 91 wt% CO are recycled. To remain

Table 5-10. Mass Flow Rate of Gas Species Across the Membrane and Percent H_2 Separation

Gas Species	Inlet Gas Stream, kg/hr		Outlet Gas Streams, kg/hr		Permeate
	Shift Gas	Sweep Gas	H_2-Rich	CO_2-Rich	% diff.
CO	12,132	0	0	12,132	0
CO_2	486,411	0	0	486,411	0
H_2	31,107	0	28,187	2921	91
H_2O	170,439	0	0	170,439	0
N_2	5775	548,370	548,370	5775	0
AR	7379	1741	1741	7379	0
CH_4	57	0	0	57	0
NH_3	14	0	0	14	0
O_2	0	2951	2951	0	0

Table 5-11. Species-Level Mass Flow Rates of the Primary Inlet and Outlet Stream of Cryogenic CO_2 Separation Module

Gas Species	Inlet CO_2-Rich, kg/hr	Stage 1 Condensate, kg/hr	Product Liquid CO_2, kg/hr	Recycle to Gas Turbine Feed, kg/hr	wt% Recycle
CO	12,132	0	1103	11,029	91
CO_2	486,411	146	439,082	47,184	10
H_2	2921	0	94	2827	97
H_2O	170,439	170,258	181	0	0
N_2	5775	0	487	5288	92
AR	7379	0	1339	6040	82
CH_4	57	0	12	44	79
NH_3	14	14	0	0	0
O_2	0		0	0	81
Total Flow Rate, kg/hr	685,128	170,418	442,298	72,412	

above the CO_2 triple point at stream pressure, a restriction is applied in the model to lower stream temperature below −55°C, resulting in restriction of CO_2 capture efficiency. Further process optimization may improve CO_2 capture. The optimization strategy may require 1) higher CO shift in the WGS section, 2) improvement in H_2 recovery in the membrane section, and 3) applying recycle stream flash separation.

The recycle gas stream is combined with the H_2-rich stream prior to injection into the gas turbine combustor.

Table 5-12 depicts composition side-by-side comparison of flow rate, temperature, pressure and related properties of the CO_2 product stream at a delivery point for the baseline and EERC model. Table 5-13 shows percent mass concentration of the product stream species. As shown, the CO_2 molar and concentration computed in the EERC model product stream are about 98.5% and 99.3%, respectively, and are slightly lower compared to that of the baseline case. The baseline case data show the molar and mass concentration value of 99.6% and 99.9%, respectively. The

Table 5-12. Composition, Flow Rate, Temperature, Pressure and Related Properties of the CO_2 Product Stream in the Delivery Pipeline for the Baseline Cases (a and b) and EERC Model (c)

	CO_2 Product		
Mole Fraction	**(a)**	**(b)**	**(c)**
CO	0.0002	0.0002	0.0039
CO_2	0.9948	0.9963	0.9854
H_2	0.0048	0.0022	0.0046
H_2O	0.0000	0.0005	0.0010
N_2	0.0000	0.0005	0.0017
AR	0.0002	0.0003	0.0033
CH_4	0.0000	0.0000	0.0001
Flow Rate, kg mole/hr	10,425	10411	10125
Flow Rate, kg/hr	456,650	456961	442298
Temperature, °C	51	49.8	50.0
Pressure, MPa, abs	15.27	15.30	15.17
AspenPlus Enthalpy, kJ/kg*	−9120	−9125	−9076
Density, kg/m^3	641.8	660.7	638.6
Molecular Weight	43.805	43.9	43.7

* 77°F and 14.696 psi.

Table 5-13. Mass Concentration of the CO_2 Product Stream

Mass Concentration	**(b)**	**(c)**
CO	0.0%	0.2%
CO_2	99.9%	99.3%
H_2	0.0%	0.0%
H_2O	0.0%	0.0%
N_2	0.0%	0.1%
AR	0.0%	0.3%
CH_4	0.0%	0.0%
NH_3	0.0%	0.0%

proposed process optimization in the WGS, H_2 membrane, and CO_2 separation modules can offer pathways for reducing the impurities in the supercritical fluid stream at the delivery point.

Table 5-14 shows the composition, flow rate, temperature, pressure, and related properties of the stack gases leaving the steam turbine module. The oxygen concentration in the stack gases for the baseline cases (a and b) and EERC model (c) are comparable. The difference in the stack CO_2 concentration is due to lower CO_2 capture obtained in the case of the EERC model. Table 5-15 shows the CO_2 capture expressed as weight percent of the combined total of the CO_2 product at the pipeline delivery point and CO_2 discharged in the stack. Compared to the baseline capture of about 90%, the EERC model based on membrane process offers 87%. It is likely that further process optimization can plausibly attain the DOE-targeted CO_2 capture of greater than 90%.

Table 5-14. Composition, Flow Rate, Temperature, Pressure, and Related Properties of the Stack Gases Leaving the Steam Turbine Module for the Three Cases

Mole Fraction	(a)	(b)	(c)
CO	0	0.0000	0.0000
CO_2	0.0083	0.0083	0.0108
H_2	0	0.0000	0.0000
H_2O	0.1222	0.1208	0.1187
N_2	0.7541	0.7523	0.7531
AR	0.0091	0.0092	0.0088
O_2	0.1064	0.1094	0.1086
NO	–	0.0000	0.0000
NO_2	–	0.0000	0.0000
Flowrate, kgmole/hr	139,657	138,425	139,699
Flowrate, kg/hr	3,834,349	3,804,480	3,846,860
Temperature, °C	132.0	140.4	133.7
Pressure, MPa, abs	0.10	0.10	0.10
AspenPlus Enthalpy, kJ/kg*	−1078.7	−1056.6	−1078.7
Density, kg/m^3	0.90	0.84	0.85
Molecular Weight	27.46	27.48	27.54

* 77°F and 14.696 psi.

Table 5-15. CO_2 Capture in the IGCC Process

Stream ID	(b)	(c)
CO_2 Capture, wt%	90%	87%
Stack CO_2, kg/hr	50,516	66,029
Product CO_2, kg/hr	456,495	439,146
Total, kg/hr	507,011	505,175

5.2.2 Plant Performance Summary

Table 5-16 shows the IGCC plant performance summary for the baseline and EERC processes. Table 5-17 shows the plant performance as a percent of gross power produced. As illustrated in Table 5-16, the published and computed baseline plant produces a net output of 543 and 540.3 MW at a respective net plant efficiency of 32.6% and 32.4% (HHV basis). The EERC model shows the net output of 577.2 MW and net plant efficiency of 34.7%.

The percent auxiliary load with respect to the total gross power produced for the three cases is 26%, 25.4%, and 20.6%, respectively (see Table 5-17). The lower auxiliary load for the computed baseline process (Case b) as compared to Case B5B is owing to the differences (lower) in the load calculated for the SELEXOL, Claus, and CO_2 compression processes. The lower auxiliary load in the EERC model is primarily due to 80% reduction in load for the CO_2 capture process.

Table 5-16. Plant Performance Summary for the Baseline and EERC Processes

	(a) Case B5B	(b) Baseline MIT Model	(c) Membrane EERC Model
Combustion Turbine Power, MWe	464.00	457.00	459.34
Sweet Gas Expander Power, MWe	7.00	8.12	0.53
Steam Turbine Power, MWe	264.00	259.44	266.70
Total Gross Power, MWe	734.00	724.56	726.80
Air Separation Unit Main Air Compressor, kWe	67,330.00	70,363.00	69,211.30
Oxygen Compressor, kWe	10,640.00	11,116.00	11,116.00
Nitrogen Compressors, kWe	35,640.00	34,343.30	36,311.00
CO_2 Compression, kWe	31,160.00	27,967.50	1,663.00
Acid Gas/CO_2 Removal, kWe	19,230.00	16,430.90	7,202.20
Claus Plant, kWe	2,030.00	1,107.00	1,107.00
Steam Plant Operation, kWe	5,440.00	5,086.00	4,655.00
Balance of Plant, kWe	19,400.00	18,309.00	18,309.00
Total Auxiliaries, MWe	191.0	184.3	149.6
Net Power, MWe	543.0	540.3	577.2
HHV Net Plant Efficiency	32.6%	32.4%	34.7%

Table 5-17. Plant Performance Summary for the Baseline and EERC Processes Expressed as Percent of the Gross Power Produced

	(a) Case B5B, %	(b) Baseline MIT Model, %	(c) Membrane EERC Model, %
Combustion Turbine Power, MWe	63.2	63.1	63.2
Sweet Gas Expander Power, MWe	1.0	1.1	0.1
Steam Turbine Power, MWe	36.0	35.8	36.7
Total Gross Power, MWe	100.0	100.0	100.0
Air Separation Unit Main Air Compressor, kWe	9.2	9.7	9.5
Oxygen Compressor, kWe	1.4	1.5	1.5
Nitrogen Compressors, kWe	4.9	4.7	5.0
CO_2 Compression, kWe	4.2	3.9	0.2
Acid Gas / CO_2 Removal, kWe	2.6	2.3	1.0
Claus Plant, kWe	0.3	0.2	0.2
Steam Plant Operation, kWe	0.7	0.7	0.6
Balance of Plant, kWe	2.6	2.5	2.5
Total Auxiliaries, MWe	15.5	16.0	16.0
Net Power, MWe	26.0	25.4	20.6

The ASU accounts for about 16% of the gross power produced and is the key auxiliary load that accounts for more than 60% and 78% of the total auxiliary load for the baseline cases (a and b) and the EERC model, respectively. Among the main air compressor, nitrogen compressor, oxygen compressor, and ASU auxiliaries the air compressor consume most power (about 9.5% of the gross power generated). The two-stage SELEXOL process and CO_2 compression account for an additional 26% and 24% of the auxiliary power load for the baseline cases (a and b). In contrast, the EERC capture process consumes only 6% of the total auxiliary load. The boiler feed water (BFW) pumps comprise over 2.8% of the load for the baseline and about 10% of the auxiliary load for all other systems including the cooling tower fans. The BFW for the EERC model consumes about 3% of the auxiliary load, leaving about 12% for the balance of plant which is comparable to the baseline.

The IGCC process based on the EERC model has shown to be a promising pathway for the reduction of plant complexity and expected reduced capital and operating cost while achieving benefits regarding increased net plant efficiency. The CO_2 capture of 87% was achieved while meeting DOE-targeted product CO_2 purity of greater than 95%.

The proposed future task for improving plant performance with improvement in CO_2 capture will require the following process optimization strategy: 1) higher CO shift in the WGS section, 2) improvement in H_2 recovery in the membrane section, and 3) applying recycle stream flash separation.

5.3 Technoeconomic Analysis of Membrane Performance

Information was provided by CSIRO on the cost and expected performance of the membrane systems. The EERC used this information to develop a technoeconomic assessment of the membranes performing under the conditions of the DOE baseline study, as presented in the previous section. The membrane cost was estimated based on membrane area requirement estimates from CSIRO. These estimates are based on performance of the membranes observed at CSIRO and the EERC. The following equation can be used to determine the total cost of membranes (not including containment vessels):

$$Total\ cost = \frac{(specific\ cost)(Total\ H_2\ production\ rate)}{(membrane\ permeance)(P_1^{0.5} - P_2^{0.5})(yield\ scaling\ factor)} \qquad \text{[Eq. 7]}$$

Specific cost is the cost per unit area for the membrane (\$ m^{-2}); the total H_2 production rate is 4006 mol s^{-1} based on the DOE baseline study flows; permeance is the measure of membrane performance (mol/m^{-2} s^{-1} $Pa^{-0.5}$); P_1 and P_2 are the H_2 partial pressures in the feed and permeate streams, respectively; and the yield scaling factor is 0.20 for 90% H_2 yield. Additional costs include containment vessels, catalysts, etc. The specific cost for the membranes was determined to be \$2703/m^2 by CSIRO. A permeance of 0.0005 mol/(m^2*s*$Pa^{0.5}$) was used based on performance data. Hydrogen partial pressures were based on the modeling effort discussed earlier. A yield-scaling factor of 0.2 was used for 90% hydrogen recovery. Based on this information, the total cost of the membranes was estimated to be \$117,289,000. This includes both materials and production. APEA was used to estimate the cost of the containment vessels for the membrane system and for warm-gas sulfur removal. The model assumed a two-stage membrane process with six vessels operating in each stage at the required pressures and flows. Sulfur removal was assumed to take

place in four beds operating in parallel. Based on this information, the overall cost for the sulfur removal membrane vessels, including piping, electrical, instrumentation, and civil work, was estimated to be $38,113,000. Cost for a regenerable sulfur sorbent, RVS-1, was also determined based on EERC purchases and operation in a 1-MW_{th} gasifier. Scaling up to 550 MW_e, the total cost of the sorbent is estimated to be $28,424,000, and this estimate does not assume a discount for a bulk order, which would likely be significant. Overall, the cost of the sulfur removal and hydrogen separation system is estimated to be $183,827,000. This estimate is in 2012 dollars. This compares to the DOE baseline estimate of $213,219,000 for a SELEXOL system for sulfur and CO_2 separation. This cost can be substituted directly into Item 5A.1 in the TPC estimate and used to update the overall economics of the process. It should be noted that very small improvements in the permeance and performance of the membrane (yield scale factor) would result in very significant cost savings for the system. Future research and development efforts have the potential to cut these costs in half.

5.4 Modeling Support for Pressurized Oxy-Combustion Systems

Pressurized oxygen-fired combustion systems (or pressurized oxy-combustion systems) have the potential to generate heat for steam and power production while producing a stream of nearly pure CO_2 that has advantages when it comes to flue gas cleanup. This is a cutting-edge technology that has the potential to improve overall efficiencies for CO_2 capture. As a first step toward developing the technology, the EERC ran small pilot-scale systems to evaluate the combustion characteristics and test gas cleanup methods in a pressurized environment. The results of this testing were presented in the previous section. To augment this effort, the EERC performed small-scale systems modeling to help understand the potential of the technology and guide testing efforts. The models are intended to serve as the foundation for future full-scale technoeconomic analysis.

Models were developed for both a single-stage and a two-stage oxy-combustion system. The single-stage system relies heavily on a stream of recycle CO_2 to temper the reaction temperature in the combustor. The combustor chosen was a fluid-bed system operating at below the ash-melting temperature; therefore, significant CO_2 recycle was used. Aspen models were used to determine the appropriate operating conditions for the system, including coal, oxygen, and recycle flow rates. The model developed is shown in Figure 5-2. The model includes a separation of the fluid bed and freeboard section of the combustor, a cyclone for recirculation of solids, a filter vessel, water quench, and a recycle system. The model was used to develop the overall test plan for the pilot-scale combustion and impurity removal testing. Table 5-18 shows a comparison of the pilot-scale results measured with an online FTIR to the modeling results achieved. The main difference can be attributed to the nitrogen levels in the gas stream and the ability to detect very high levels of CO_2. The nitrogen levels are higher in the pilot data because more nitrogen was needed for system purges than was anticipated in the model. The NO levels in the system were significantly higher in the pilot unit as compared to the model, and this is assumed to be due to the higher-than-expected nitrogen levels. SO_2 levels were much lower than the pilot data, and this was attributed to the use of limestone in the fluid-bed combustor. The ability to capture sulfur in the fluid bed under pressurized oxy-combustion appears to be enhanced as compared to standard combustion conditions.

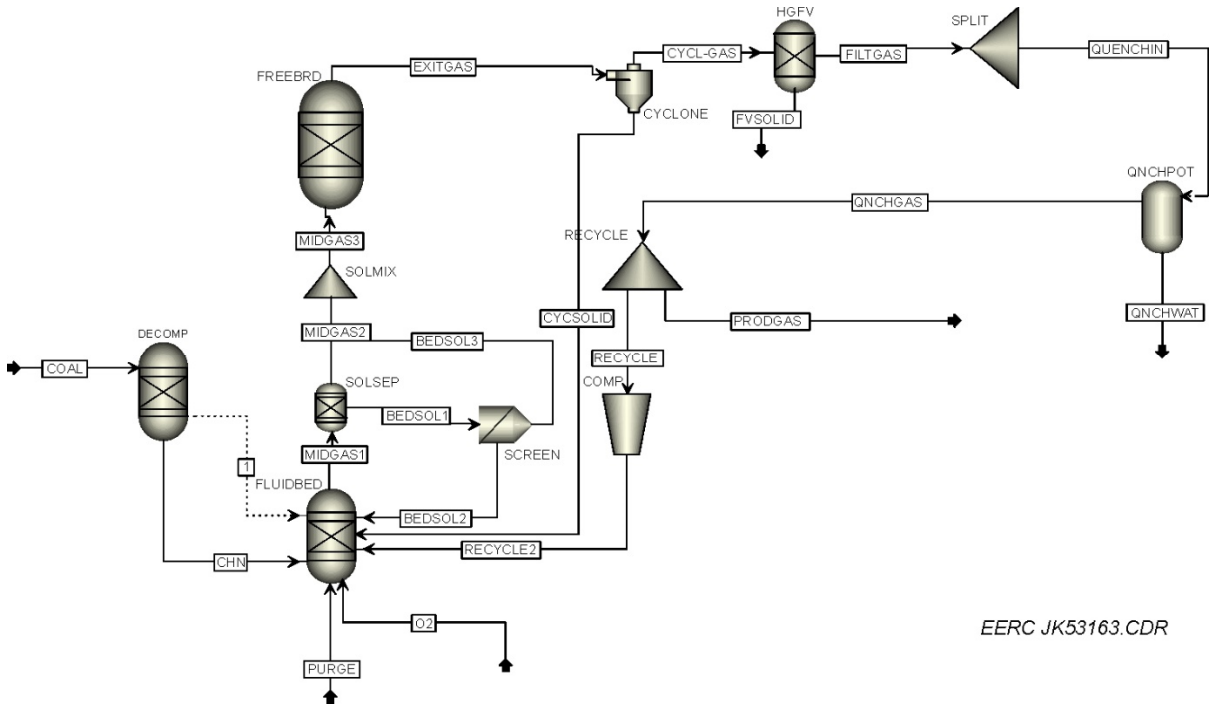

Figure 5-2. Single-stage pressurized oxy-combustion model.

Table 5-18. Single-Stage Pressurized Oxy-Combustion Model and Pilot Data

	Aspen Model	Pilot Test 1	Pilot Test 2	Pilot Test 3
vol%				
O_2	6.7	2	1.1	0.9
N_2	0.5	5.1	4.1	3.7
CO_2	91.7	87	88.8	89.6
H_2O	1.1	5.9	6	6
ppmv				
NO	4	117	85	106
NO_2	0	6	18	26
N_2O	N/A	31	22	21
SO_2	425	18	2	3
SO_3	65	1	1	0
COS	0	2	0	0
H_2SO_4	N/A	0	0	0

A two-stage pressurized oxy-combustion system was also tested to evaluate the overall potential of this technology. The system was set up using the same fluid-bed system as in the single stage, except the fluid bed was used for partial oxidation. A high-temperature entrained-flow reactor was used to fully oxidize the gas, and impurity removal strategies were also tested for SO_2 and NO. Figure 5-3 shows the Aspen model that was set up to evaluate the technology concept prior to testing. For this system, the CO_2 was recycled to the second stage to help abate the flame temperature. The recycle occurred after running through the sulfur and NO_x removal step.

Table 5-19 compares the model results to the pilot-scale testing. The model was able to predict the CO_2 composition reasonably well when excess oxygen was controlled to near 1.7% in the pilot unit. The model also predicted the low levels of NO_x observed. The SO_2 levels correlated very well with the model predictions, but the model predicted higher levels of SO_3 than was measured in the system. This is believed to be the result of measurement difficulties because under these conditions, the SO_3 quickly converts to H_2SO_4 and condenses before it can be measured. Overall, the model was shown to perform reasonably well and can be used as the foundation for future scale-up efforts.

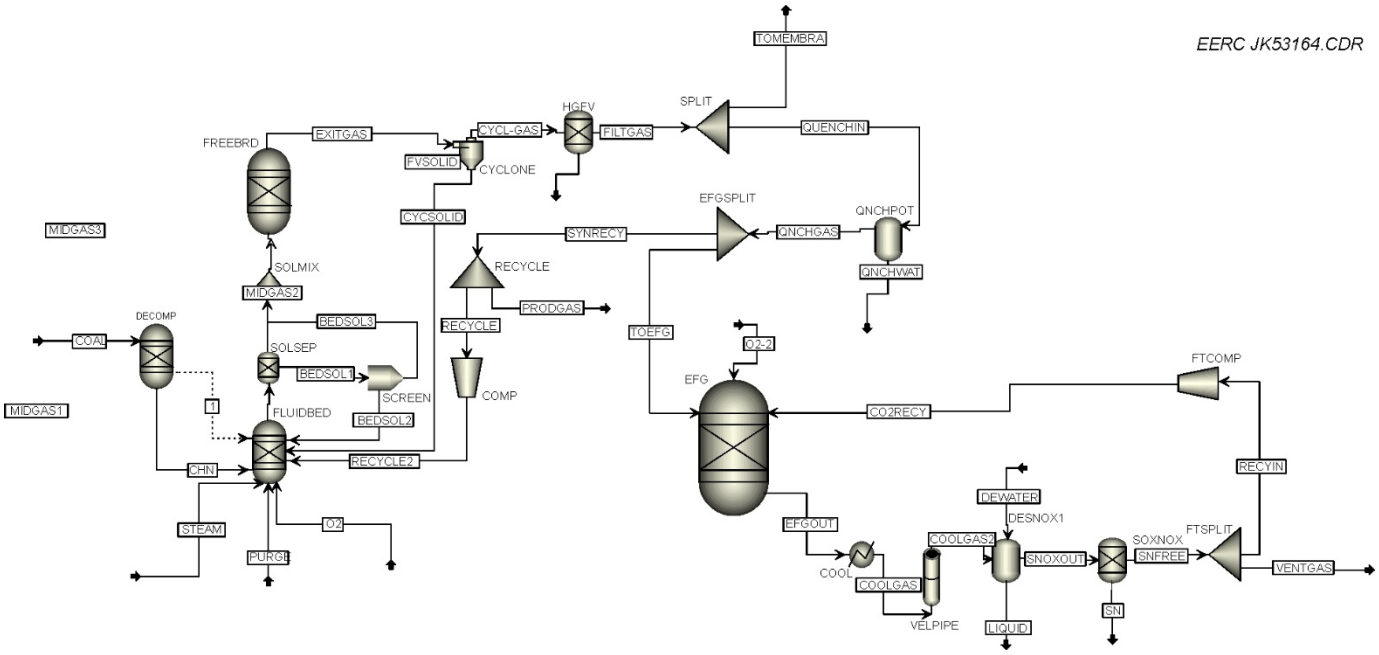

Figure 5-3. Aspen model for two-stage pressurized oxy-combustion.

Table 5-19. Two-Stage Pressurized Oxy-Combustion Model and Pilot Data

	Aspen Model	Pilot Test 4	Pilot Test 5	Pilot Test 9
vol%				
H_2O	7.8	5.1	5.7	5.1
CO_2	89.9	83.0	86.4	89.5
O_2	1.7	4.8	2.9	1.9
ppmv				
NO	2	2	2	2
NO_2	0	0	0	0
N_2O	N/A	0	0	0
SO_2	835	766	806	680
SO_3	387	0	0	0
COS	0	0	0	0
H_2SO_4	N/A	3	6	1
NH_3	0	0	0	0
CO	0	40	3	11

6.0 CONCLUSIONS

This subtask focused on several research areas in an effort to find ways to decrease the cost of capture across both precombustion and postcombustion platforms. Potential for improvements was observed in all areas investigated. Some recommendations have also been suggested.

CO_2 Solutions sought to combine its enzyme-based solvent with an RPB, anticipating that the RPB would improve the performance of the solvent. The RPB functioned well as an absorber for capturing CO_2, but an improvement in performance was not observed. Solvent performance was noted to be similar to that measured in previous testing at the EERC. The RPB did not function well as a solvent desorber, and it is not recommended that it be used for that purpose. If the assumptions are made that scale-up would be manufactured in a modular fashion with multiple RPB beds and that the performance of the solvent is similar to that of MEA, then the economic projection is that the cost of CO_2 capture for a 550-MW greenfield plant would approach $30 per tonne ($US 2007) of CO_2 captured. This cost reduction is based on the much-reduced cost of the RPB system over a conventional column-based design and smaller footprint. Although this shows great potential to reduce the cost, much more study is needed to determine more accurately how the RPB concept would scale up, and vetting of the associated costs needs to continue.

A solvent produced from humic acid extraction from North Dakota lignite coal (ARCTECH, Inc.) was evaluated to collect data with regard to its ability to flow in a spray column and to capture CO_2, SO_2, and NO_x in a batch mode. Regeneration of the solvent was not evaluated. The solvent flowed well, and foaming could be controlled using antifoaming agents. Some propensity for increased viscosity that was observed by ARCTECH in laboratory tests was not observed. The solvent indeed performed well, and the maximum CO_2 capture was 82%, SO_2 capture was between 80% and 90%, and NO_x capture was between 10% and 20%. The solvent is a good candidate for

additional testing, but its regeneration behavior stills needs to be examined. The loaded solvent can also be processed to produce a solid filtering media for wastewater. The combined processes and how they would integrate into a full-scale system also warrant further investigation. Because of the early stages of this technology, economic evaluation was not conducted.

CSIRO provided hydrogen separation membranes to test for separation performance. Tests were conducted utilizing EERC gasification equipment to produce the syngas from lignite coal provided by the Falkirk and Freedom Mines in North Dakota. These were the first tests of the CSIRO membranes on coal-derived syngas. The membranes worked very well during these tests, but several improvements are recommended as the technology is improved. To move this technology forward, better control of the endothermic reaction of the membrane as it is first exposed to the syngas to reduce fracture potential, additional information on the transmembrane pressure boundaries and upper limits, and full life cycle testing to determine robustness must be explored. The metallurgy between the membrane separator tubes and system piping must be investigated further to remove leaks. Preliminary economic projections were conducted on the hydrogen separation process. Scaling costs to an equivalent 550-MW system projected a 14% reduction in cost as compared to the DOE baseline estimate for a SELEXOL system for sulfur removal and CO_2 separation. Small future improvements in permeance and performance of the membrane would result in a very significant cost savings for the system.

Pressurized oxy-combustion technology from the standpoint of CO_2 purification was tested on the pilot scale. This technology can produce a highly concentrated, pressurized gas stream of CO_2 as part of the process, but the stream purity must be high for the process to work without excessive annual maintenance costs. If the purity can be increased, then it holds great promise in realizing highly efficient systems with simplified CO_2 purification techniques. The evaluated concept, referred to as the $DeSNO_x$ process, has the potential to be used in not only pressurized oxy-combustion but also in supercritical CO_2 cycles. Testing indicated that over 77% nitrogen capture was achieved along with greater than 90% SO_2 capture. Challenges remain with selective condensation of acids at the entry of the $DeSNO_x$ system which must be addressed as the technology is moved forward. Beyond this, no major barriers have been encountered with this postcombustion impurity removal process. From this testing, models of both a single-stage and a two-stage oxycombustion system were created. These models are intended to provide the foundation for future full-scale technoeconomic analysis. Flow streams were predicted by the models fairly well and, overall, they were shown to perform reasonably well.

To increase the possible variations in IGCC configuration, the EERC modified a model constructed by MIT which represents a GE radiant cooler IGCC gasification system with CO_2 capture and compression. The modification substituted H_2 separation membranes for the more traditional SELEXOL process. Other modifications were undertaken, as necessary, for appropriate subsystems needed for the membranes. As compared to the original MIT model and the DOE Baseline Case B5B for an IGCC system, the EERC-modified model indicated an improvement in net power generation of 577 MW_e over 540 MW_e for MIT and 543 MW_e for the DOE case. Efficiency was also improved to 34.7% over 32.4% and 32.6% for the MIT model and the DOE base case, respectively. The model offers an additional process methodology to model performance and ultimately to provide economic analysis of IGCC processes that are considered for future power plants.

This subtask has demonstrated additional promising pathways to improve CO_2 purity in combustion and gasification systems, reduce the complexity of plant systems, and project potential economic benefits for the technologies tested. The modeling of many of these technologies was carried out and will provide the foundation for future modeling and pilot-scale testing efforts. This work can be directly applied to the analysis of lignite and its future place in energy production and provide additional options for consideration.

7.0 REFERENCES

1. Kay, J.P.; Azenkeng, A.; Fiala, N.J.; Jensen, M.D.; Laumb, J.D., Leroux, K.M.; McCollor, D.P.; Stanislowski, J.J.; Tolbert, S.C.; Curran, T.J. *Subtask 2.18 – Advancing CO_2 Capture Technology: Partnership for CO_2 Capture (PCO_2C) Phase III*; Final Report for U.S. Department of Energy National Energy Technology Laboratory Cooperative Agreement No. DE-FC26-08NT43291, North Dakota Industrial Commission, PPL Montana, Nebraska Public Power District, Tri-Mer Corporation, Montana–Dakota Utilities Co., Basin Electric Power Cooperative, KCRC/Korean Institute of Energy Research, Cansolv Technologies, and CO_2 Solutions, Inc.; EERC Publication 2016-EERC-02-16; Energy & Environmental Research Center: Grand Forks, ND, Feb 2016.

2. CO_2 Solutions, Inc. www.co2solutions.com (accessed March 2017).

3. ARCTECH, Inc. www.arctech.com/PDF/PressReleases/Apr 2014 ARCTECH_PressRelease_ CCEMC.pdf (accessed March 2017).

4. Kluiters, S.C.A. *Status Review on Membrane Systems for Hydrogen Separation*; Dec 2004.

5. *Effects of a Transition to a Hydrogen Economy on Employment in the United States, Report to Congress;* U.S. Department of Energy, July 2008.
6. Ellis, S. Honda Fuel Cell Vehicle Progress. Presented at the Advancing the Hydrogen Economy Action Summit II; Grand Forks, ND; Sept 4, 2008.

7. Holmes, M. Coal-to-Hydrogen. Presented at the Advancing the Hydrogen Economy Action Summit II; Grand Forks, ND; Sept 4, 2008.

8. Black, J. *Cost and Performance Baseline for Fossil Energy Plants Volume 1: Bituminous Coal and Natural Gas to Electricity*; Revision 2; DOE/NETL-2010/1397; 2010.

9. Gerdes, K. *Current and Future Technologies for Gasification Based Power Generation, Volume 2: Carbon Capture, Revision 1*; DOE/NETL-2009/1389; 2010.

10. Klara, J.M. *IGCC:* Coals Pathway to the Future. Presented at the Gasification Technologies Conference; Oct 4, 2006.

11. Sondreal, E.A.; Swanson, M.L.; Benson, S.A.; Holmes, M.J.; Jensen, M.D. A Review of Gasification Technology for Coproduction of Power, Synfuels, and Hydrogen from Low-

Rank Coals. *In Proceedings of the 20th Symposium on Western Fuels*; Marriott Denver Tech Center, Denver, CO; Oct 24–26, 2006.

12. Gerdes, K. The Potential of Advanced Gasification Pathways to Reduce CO_2 Capture Costs. Presented at the Gasification Technologies Conference, Colorado Springs, CO; Oct 2009.

13. Hoffman, J. Cost and Performance for Low-Rank Coal Power Plants. Presented at the Gasification Technologies Conference, Colorado Springs CO, Oct 2009.

14. Plunkett, J. Performance & Cost Comparisons of Alternate IGCC Based Carbon Capture Technologies. Presented at the Gasification Technologies Conference, Colorado Springs, CO, Oct 2009.

15. Stanislowski, J.; Laumb, J. Gasification of Lignites to Produce Liquid Fuels, Hydrogen, and Power. Presented at the Pittsburgh Coal Conference, Sept 2009.

16. Stocker, J.; Whysall, M.; Miller, G. *30 years of PSA Technology for Hydrogen Purification*; UOP LLC; 1998.

17. Adhikari, S.; Fernando, S. *Hydrogen Membrane Separation Techniques*; ACS Publications Industrial & Engineering Chemistry Research; 2006.

18. DOE Hydrogen Program. *FY2008 Annual Progress Report*; www.hydrogen. energy.gov/index.html; Dec 2008.

19. Ockwig, N.; Nenoff, T. *Membranes for Hydrogen Separation*; ACS Publications Chemical Review, 2007.

20. Rothenberger, K.; Howard, B.; Killmeyer, R.; Ciocco, M.; Morreale, B.; Enick, R. Palladium-Copper Alloy Membrane Performance under Continuous H_2S Exposure; www.netl.doe.gov (accessed April 2017).

21. Subramanian, P.; Laughlin, D. Binary Alloy Phase Diagrams – 2nd, ed.; Massalski, T., ed.; ASM International; 1990; pp 1454–1456.

22. Volkov, A.; Kazantsev, V. Kourov, N.; Kruglikov, N. *Formation of the Structure and Properties of Cu-Pd Alloys During the A1-B2 Phase Transitions*; The Physics of Metals and Metallography; 2008.

23. Kamakoti, P.; Sholl, D. Ab Initio Lattice-Gas Modeling of Interstitial Hydrogen Diffusion in CuPd Alloys; *Physical Review B 71*, **2005**, 014301.

24. Sholl, D. Using Density Functional Theory to Study Hydrogen Diffusion in Metals: A brief overview; *Journal of Alloys and Compounds* **2007**, 446–447, 462–468.

25. Kamakoti, P.; Sholl, D.; A Comparison of Hydrogen Diffusivities in Pd and CuPd Alloys Using Density Functional Theory. *Journal of Membrane Science* **2003**, *225*, 145–154.

26. Kamakoti, P.; Sholl, D. Towards First Principles-Based Identification of Ternary Alloys for Hydrogen Purification Membranes. *Journal of Membrane Science* **2006**, *279,* 94–99.

27. Hao, S.; Sholl, D. Selection of Dopants to Enhance Hydrogen Diffusion Rates in MgH_2 and $NaMgH_3$. *Applied Physics Letters* **2009**, *94,* 171909.

28. Hao, S.; Sholl, D. Comparison of First Principles Calculations and Experiments for Hydrogen Permeation through Amorphous ZrNi and ZrNiNb Films. *Journal of Membrane Science* **2010**, *350,* 402.

29. Hao, S.; Sholl, D. The Role of Interstitial H_2 in Hydrogen Diffusion in Light Metal Borohydrides. *Phys. Chem. Chem. Phys*. **2009**, *11*, 11106.

30. O'Brien, C. *Sulfur Poisoning of Pd and PdCu Alloy Hydrogen Separation Membranes*; Doctoral Thesis; Carnegie Mellon University; 2011.

31. Gabitto, J.; Tsouris, C. Sulfur Poisoning of Metal Membranes for Hydrogen Separation. *International Review of Chemical Engineering* **2009**, *1* (5), 394–411.

32. Ma, Y.; Pomerantz, N.; Chen, C. *Sulfur-Tolerant Pd/Cu and Pd/Au Alloy Membranes for Hydrogen Separation with High Pressure CO_2 Sequestration*; Periodic Progress Report, 2007.

33. Yang, J.; Nishimura, C.; Komaki, M. Hydrogen Permeation of $Pd_{60}Cu_{40}$ Alloy Covered V-15Ni Composite Membrane in Mixed Gases Containing H_2S. *Journal of Membrane Science* **2008**, *309*, 246–250.

34. Phillips, J. et al. *Can Future Coal Power Plants Meet CO_2 Emission Standards Without Carbon Capture & Storage?*; Electric Power Research Institute, Oct 2015, 16 p.

35. Forrest, B.; Lu, X.; McGroddy, M.; Strakey, J.; Fetvedt, J.; Freed, D.; Thimsen, D.; Phillips, J.; Marasigan, J.; Hendrix, H.; Maxson, A.; Booras, G.; Shingledecker, J.; Wright, I.; Tossey, B.; *Oxy-Lignite Syngas Fueled Semi-Closed Brayton Cycle Process Evaluation – Evaluation of Cycle Performance, Cost, and Development Plan*; Final Report; Jan 2014, 100 p.

36. Nsakala, N.Y.; Liljedahl, G.N.; Turek, D.G. *Greenhouse Gas Emissions Control by Oxygen Firing in Circulating Fluidized Bed Boilers: Phase II – Pilot Scale Testing and Updated Performance and Economics for Oxygen Fired CFB with CO_2 Capture Final Technical Progress Report*; PPL Report No. PPL-04-CT-25; Alstom Power Inc. Power Plant Laboratories, Oct 27, 2004.

37. Seltzer, A.; Fan, Z.; Robertson, A. *Conceptual Design of Supercritical Oxygen-Based PC Boiler*; Final Report DE-FC26-04NT42207; Foster Wheeler Power Group, Inc., Nov 2006.

38. Adanez, J.; Abad, A.; Garcia-Labiano, F.; Gayan, P.; de Diego, L.F. Progress in Chemical-Looping Combustion and Reforming Technologies. *Progress in Energy and Combustion Science* **2012** *38*, 215–282.

39. Andrus, Jr., H.E.; Chiu, J.H.; Thibeault, P.R.; Brautsch, A. Alstom's Calcium Oxide Chemical Looping Combustion Coal Power Technology Development. Presented at the 34th International Technology Conference on Clean Coal & Fuel Systems, May 31 – June 4, 2009, Clearwater, FL.

40. Muzio, L.J.; Teague M.E.; Kramlich, J.C.; Cole, J.A.; McCarthy, J.M.; Lyon, R.K. Errors in Grab Sample Measurements of N_20 from Combustion Sources. *JAPCA* **1989**, *39*, 287–293.

41. Black, J. *Cost and Performance Baseline for Fossil Energy Plants, Volume 1*: *Bituminous Coal and Natural Gas to Electricity*; Revision 2a; DOE/2010/1397; Sept 2013.

42. Black, J. *Quality Guidelines for Energy Systems Studies, Capital Cost Scaling Methodology*; DOE/NETL-341/013113; Jan 2013.

43. U.S. Department of Energy National Energy Technology Laboratory Office of Program Planning and Analysis. *Quality Guidelines for Energy System Studies, Cost Estimation Methodology for NETL Assessments of Power Plant Performance*; DOE/NETL-2011/1455; April 2011.

44. Fout T.; Zoelle A.; Keairns D.; Turner M.; Woods M.; Kuehn N.; Shah V.; Chou V.; Hamilton B. A.; Pinkerton L. Cost and Performance Baseline for Fossil Energy Plants Volume 1a: Bituminous Coal (PC) and Natural Gas to Electricity Revision 3, DOE/NETL-2015/1723; July 6, 2015.

45. Field R.P.; Brasington, R. Documentation of Simulation Model GEE_BIT_SEL_wCC_ NOSF", IGCC Version 2 Model Documentation – MIT Energy Initiative, Massachusetts Institute of Technology. www.google.com/url?sa=t&rct=j&q=&esrc=s&source=web&cd=1&cad=rja&uact=8&ved=0ahUKEwi38PmRuobTAhUk5oMKHYUGD6UQFggnMAA&url=https%3A%2F%2Fs3-eu-west-1.amazonaws.com%2Fpstorage-acs-6854636%2F4256743%2Fie200288u_si_001.pdf&usg=AFQjCNEN7SXmLZMWRSrkhJkj8-vlzq2ipA&sig2=l9YIjxStwgUm7w9_d4s2ig&bvm=bv.151325232,d.amc (accessed April 2017).